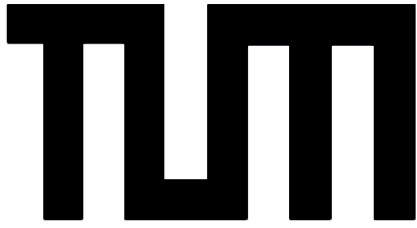Felix Reimold

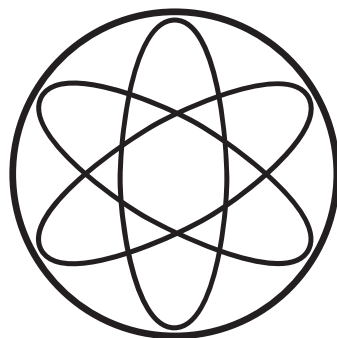# Experimental Studies and Modeling of Divertor Plasma Detachment in H-Mode Discharges in the ASDEX Upgrade Tokamak
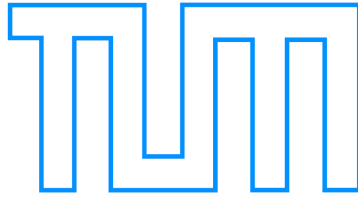
Experimental Studies and Modeling of Divertor Plasma Detachment in H-Mode Discharges in the ASDEX Upgrade Tokamak

Felix Reimold

Physik-Department der
Technischen Universität München (TUM)
&
Max-Planck-Institut für Plasmaphysik (IPP)

Technische Universität München

Max-Planck-Institut für Plasmaphysik

Experimental Studies and Modeling of Divertor Plasma Detachment in H-Mode Discharges in the ASDEX Upgrade Tokamak

Felix Reimold

Abstract

In future fusion devices like ITER and DEMO power exhaust is a challenge. Without radiation cooling, the power flux to the DEMO divertor target plates of several 100 MWm^{-2} exceeds the specified steady-state material limits of 5–15 MWm^{-2}. High radiated power fractions by impurity seeding and divertor detachment are required to limit the heat and particle fluxes to the material surfaces. Control, characterization and understanding of divertor detachment in H-mode plasmas with significant power fluxes to the divertor are crucial for sound extrapolation of results from present-day tokamaks like ASDEX Upgrade to future reactors like DEMO.

The first stable, completely detached H-mode plasmas in ASDEX Upgrade with a full tungsten first wall has been achieved by nitrogen seeding into the divertor. A new phases is added to the detachment classification described in Ref. [1]: The transition from partial detachment of the outer divertor target with its transient increase of the line integrated electron density by about 15 % to complete detachment of both targets correlates to the appearance of intense, strongly localized, stable radiation at the X-point. Radiated power fractions increase from about 50 % without to 85 % with nitrogen seeding. The X-point radiation is accompanied by a loss of pedestal top plasma pressure of about 60 % and strong Balmer radiation inside the confined plasma at the X-point. The core pressure inside $\varrho_{\mathrm{pol}} < 0.7$ changes only by about 10 % during complete detachment. The confinement parameter H_{98} ranges from 0.8–1.0 during detached operation. With nitrogen seeding the frequency of edge localized modes (type-III) increases from the 100 Hz range to a broadband distribution at $1 - 2$ kHz with a large reduction in their size.

Accompanying SOLPS modeling reconciles almost all the experimental measurements with the simulations. The code recovers the phenomena observed in experiment during detachment. The level of agreement of a detailed comparison of simulations with experimental data of high recycling and detached high power H-mode discharges is a novelty. An exception is the lower divertor neutral density in the simulations that indicates a deficiency in the description of the divertor neutral compression and the plasma fueling. An increase of the perpendicular transport in the divertor region is necessary to match the simulations to the experiment. It is larger in the inner divertor. The inclusion of drifts is crucial for modeling of the ASDEX Upgrade SOL and divertor in detached H-mode conditions. Drifts improve the quality of the match to experiment, especially in the inner divertor, and reproduce features such as a detached vertical inner target, improved X-point radiation stability and improved impurity retention of the divertor.

The combined approach with modeling and experiment allows to validate the simulations and simultaneously use the modeling for the interpretation and the analysis of the diagnostic measurements and the involved physical processes.

Kurzfassung

Für zukünftige Fusionsreaktoren wie ITER und DEMO wird die Leistungsabfuhr eine Herausforderung. Hohe Leistungsflüsse von mehreren 100 MWm^{-2} auf die Prallplatten in DEMO übersteigen die stationären Materialbelastungsgrenzen von 5–15 MWm^{-2}. Ein Großteil der Leistung muss durch Einbringen von Verunreinigungen abgestrahlt werden und die Ablösung des Plasmas von den Prallplatten (Detachment) ist notwendig, um die Leistungs- und Teilchenflüsse zu begrenzen. Die Kontrolle, die Charakterisierung und das Verständnis des Ablösungsprozesses im Divertor ist entscheidend, um die in heutigen Tokamaks wie ASDEX Upgrade gewonnenen Ergebnisse auf zukünftige Fusionsreaktoren wie DEMO übertragen zu können.

Das erste stabile, vollständig abgelöste Plasma im Regime mit verbessertem Einschluss, der H-Mode, in ASDEX Upgrade mit vollständiger Wolframwand wurde durch Einblasen von Stickstoff in den Divertor erreicht. Der Übergang von partieller Ablösung, die mit einem vorrübergehenden Anstieg der linienintegrierten Elektronendichte um ca. 15 % einhergeht, zur vollständigen Ablösung korreliert mit dem Auftreten einer intensiven, stark lokalisierten, stabilen Strahlung am X-Punkt. Die abgestrahlte Leistung steigt von ca. 50 % ohne auf ca. 85 % mit dem Einblasen von Stickstoff an. Die X-Punkt-Strahlung wird begleitet von einem Druckverlust von ca. 60 % an der Oberkante der Gradientenregion am Plasmarand (Pedestal) und intensiver Balmer Linienstrahlung am X-Punkt. Die Druckänderung während der vollständigen Ablösung innerhalb der Gradientenregion ist auf ca. 10 % begrenzt. Die globale Einschlusszeit sinkt durch den Betrieb mit abgelöstem Plasma um nur 10–20 %. Mit dem Einblasen von Stickstoff wächst die Frequenz von am Rand lokalisierten Moden aus dem Bereich von 100 Hz auf eine breitbandige Verteilung um $1-2$ kHz an und ihre Größe reduziert sich stark.

Die begleitende Modellierung mit dem SOLPS-Code kann erstmals fast alle experimentellen Messungen mit den Simulationen in Einklang bringen. Der Code reproduziert die beobachteten Phänomene während der Ablösung. Der Grad an Übereinstimmung der Simulationen mit den experimentellen Daten aus den stark rezyklierenden und abgelösten H-Mode-Plasmen ist eine Neuheit. Eine Ausnahme bildet der zu niedrige Neutraldruck im simulierten Divertor. Er weißt auf ein Defizit des Codes bei der Beschreibung der Kompression von Neutralteilchen im Divertor und des Befüllens des Plasmas hin. Um die Simulationen an das Experiment anzupassen, ist ein erhöhter senkrechter Transport im Divertor notwendig. Das Einbinden von Driften in der Modelierung von abgelösten H-Mode Bedingungen ist entscheidend, um die Übereinstimmung mit dem Experiment zu verbessern und experimentell beobachtete Merkmale in der Simulation nachbilden zu können.

Contents

CHAPTER 1

Introduction

This chapter introduces nuclear fusion and different confinement approaches for plasmas with a special focus on the tokamak. The importance of power exhaust handling is explained and concepts for power exhaust are presented [1].

One of the most important resources deciding on a nation's wealth and prospects is the available energy and related resources [3, 4]. With the natural resources of fossil energy carriers depleting [5, 6] and a large-scale detrimental impact of traditional combustive energy production on the ecosystem earth, such as global warming [7], alternative energy sources have to be developed. In addition to the renewable energy with its widely discussed potential [8–10] and its well-known challenges [11–15], nuclear fusion is a candidate for this.

1.1 Nuclear Fusion

Nuclear fusion is the process of two light nuclei forming a heavier one. For mass numbers smaller than that of iron ($^{56}_{26}$Fe) fusion reactions can be exothermic. Most energy per nucleon is gained in fusion processes transforming hydrogen isotopes H,D,T or $^{3}_{2}$He to $^{4}_{2}$He. For fusion to occur the light nuclei need to overcome the repellent Coulomb force of the positively charged protons inside the nuclei. A high kinetic energy is required to reach a minimum distance enabling the strong interaction to dominate over the electromagnetic repulsion[2]. For net energy production the power released by fusion reactions, P_{fusion}, has to be larger than the applied external power, P_{ext}, to generate these reactions such that $Q = P_{\text{fusion}}/P_{\text{ext}} > 1$. In colliding beams fusion a net energy gain ($Q > 1$) is not possible due to (elastic) collisions [18–21]. Thus, a confined, thermalized plasma at sufficiently high temperature is used to to induce fusion reactions. The fusion output at a given plasma density is determined by the reaction rate, which is defined as a convolution of the velocity-weighted cross-section with a Maxwellian distribution. Of the considered hydrogen isotope reactions shown in figure 1.1 only the DT reaction has a large enough

---

1   Some material is adopted from [2]
2   Muon-catalyzed, cold fusion [16, 17] is not considered here.

reaction rate below plasma temperatures of 1 MeV[1]. This is a result from a resonant energy level in the $^5_2$He nucleus that decays to $^4_2$He and a neutron.

$$^2_1\text{D} + {}^3_1\text{T} \longrightarrow {}^5_2\text{He}^* \longrightarrow {}^4_2\text{He}(3.5\,\text{MeV}) + {}^1_0\text{n}(14.1\,\text{MeV}) \tag{1.1}$$
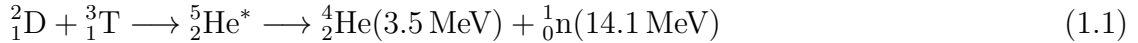
The reaction rate is at a maximum at a temperature of 64 keV [23], which corresponds to approximately 700 Mio.°C. Technically feasible plasma temperatures of about 10–20 keV are sufficient for a fusion plasma using the high-energy tail of the Maxwell distribution for fusion reactions. A large energy gain of 17.6 MeV per reaction and the fact that none of the fusion products is a radioactive isotope is a secondary benefit of the DT reaction. Radioactive waste will be generated from the structural and wall component of a reactor by neutron-induced activation. The optimal material mix of the reactor structural components that will limit the amount and the lifetime of the radioactive waste to a minimum is an active field of research [24–27].

Figure 1.1: Reaction rates of potential fusion reactions for reactors [22].

An economic consideration for energy production is the availability of the fuel deuterium and tritium. Deuterium is a stable isotope of hydrogen with an abundance of 0.0128–0.0149 % [28] and as such can be distilled from water at reasonable prices [29]. Tritium is a radioactive isotope of hydrogen with a decay time of 12.3 years [30], which is why there are no considerable 'natural' tritium resources. After a critical startup of fusion [31], the tritium supply shall be assured by breeding tritium from lithium in the blanket of a reactor, which is a cavity between the plasma facing components, PFC, and the vessel casing [29, 32]. The necessary lithium is relatively abundant and wide-spread [33].

1.2 Inertial & Magnetic Confinement

For net fusion energy production in a plasma, particles and kinetic energy have to be confined long enough. The Lawson criterion is derived from power balance considerations for a pure DT plasma and defines plasma properties that are necessary to achieve a self-heated plasma with $Q > 1$. It reads $nT\tau_\text{E} > 3 \times 10^{21}$ m^{-3}keV s [29], where n is the plasma density, T is the plasma temperature and τ_E is the energy confinement time [29]. Deliberate puffing of non-hydrogenic species, i.e. impurity seeding, or intrinsic impurity sources, e.g. sputtering of wall material, require a modified Lawson criterion, that takes additional energy losses from impurity line radiation and lower fusion output due to dilution of the hydrogenic plasma species, i.e. fuel dilution, into account. One form of

---

1 In plasma physics it is common to give temperatures in equivalent energy units $T \equiv k_\text{B}T$.

the modified Lawson criterion is given in Ref. [34].

$$n_e \tau_E \geq \frac{3 f_{tot} T}{\frac{1}{4} \langle \sigma_{DT} v \rangle f_H^2 E_\alpha - L_Z(T)} \tag{1.2}$$

where n_e, n_i and n_H are the electron, ion and hydrogenic densities respectively, $T_e = T_i = T$ are electron and ion temperatures, $f_H = n_H/n_e$ is the fractional abundance of hydrogenic species, $f_{tot} = \frac{\sum_i n_i}{n_e} \leq 1$ is the ion-electron density ratio (dilution) and E_α is the kinetic energy of the alpha particle. The first term in the denominator of (1.2) is the rate of energy production from fusion reactions and the second term is the total radiative loss function, L_Z. Without fuel dilution, $f_{tot} = f_H = 1$, and without radiation losses, $L_Z = 0$, this expression reduces to the usual Lawson criterion. The two basic confinement schemes that presently attempt to achieve the required plasma conditions set by the Lawson criterion will be briefly described in the following.

In inertial confinement fusion, small DT ice pellets are isotropically and homogeneously heated by laser or ion beams [35, 36]. The intense heating (1 MJ) of the pellet within a short time (20 ns) [37, 38] leads to ablation of the outermost pellet shell [39]. The recoil of the ablated material compresses the inner parts of the pellet [37, 40]. The compression and a fast ignition laser pulse provide confinement and heating at the same time and initiate the fusion reactions. However, the necessary homogeneous and isotropic nature of the compression and counteracting instabilities, e.g. Rayleigh-Taylor, are a major challenge for achieving $Q > 1$ [38, 41]. For a reactor ($P_{fusion} = 3$ GW) high repetition frequencies of about 3 Hz at 1 GJ energy output per pellet are a major technological challenge given the need for accurate positioning of the pellet to guarantee homogeneous heating.
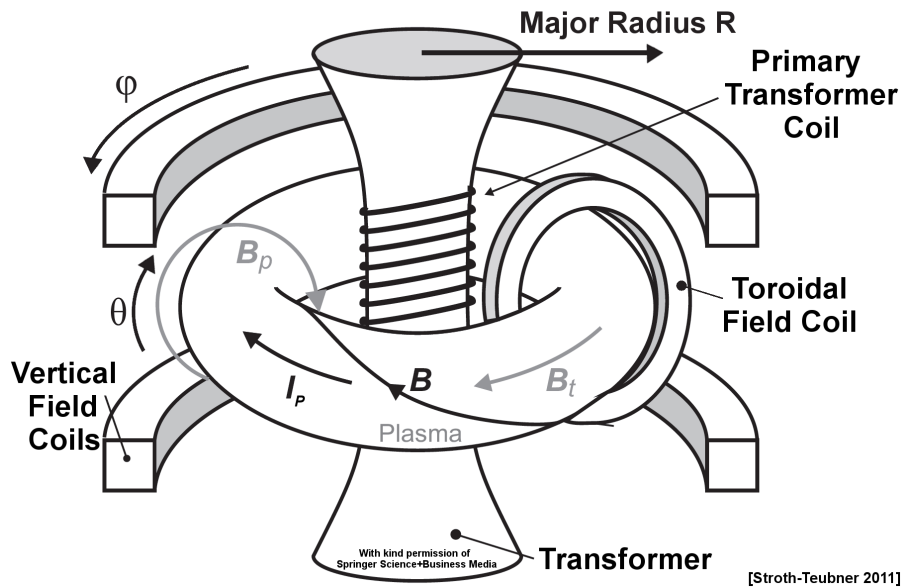
Figure 1.2: In a tokamak magnetic field coils produce the toroidal magnetic field $B_{t/\phi}$. The induced plasma current I_P generates the poloidal magnetic field $B_{p/\theta}$. Vertical magnetic field coils are used for position control of the plasma [42, p.272 ff]. Figure adapted from Ref. [43].

In magnetic confinement fusion, charged particles are confined by magnetic fields using the Lorentz force to restrict their motion perpendicular to field lines. The particles travel on helical trajectories along magnetic field lines, the so called gyro-motion [44]. A toroidal magnetic field confines charged particles in zeroth order. Gyro-orbit drifts require a poloidal magnetic field [42, p.284] such that the actual magnetic field lines have a helical shape as shown in figure 1.2.

There are two competing approaches of how to generate the poloidal magnetic field. In a tokamak it is produced by a toroidal plasma current, I_P, that is driven by an induced electric field from a primary transformer coil, see figure 1.2. In stellerators the poloidal field relies on a more complicated set of sophisticated, external field coils only, e.g. by helical coils [45, 46] or optimized modular field coils [47]. This thesis is concerned with experiments in the tokamak ASDEX Upgrade, AUG, and the following focuses on the tokamak only.

1.3 The Tokamak

A tokamak is characterized by two geometric quantities shown in figure 1.2: the major radius, R, is the distance from the toroidal axis of symmetry. The minor radius, r, is the distance from the geometric/magnetic axis in the poloidal plane. The major radius R is used as a geometric coordinate and as a measure of the spatial dimensions of a specific machine, i.e. machine size. Notation for minor radius differentiates between the machine specific parameter a and the coordinate r. The inverse aspect ratio is an important machine parameter that is defined as $\varepsilon = \frac{a}{R}$. The plasma topology in a tokamak is determined by the magnetic field geometry. The magnetic field can be split in the toroidal and poloidal components such that $\vec{B} = B_\phi \vec{e}_\phi + B_\theta \vec{e}_\theta$. The toroidal magnetic field is created by the toroidal field coils $B_\phi \propto R^{-1}$ and the poloidal magnetic field is created by the plasma current $B_\theta \propto I_P$. In a tokamak the absolute magnitude of the toroidal magnetic field is usually much larger then that of the poloidal field and the magnetic field strength can be approximated by $B \approx B_\phi$. The magnetic field lines wind helically around the magnetic axis, which is defined by $B_\theta = 0$. The magnetic field pitch angle, α_{pitch}, is defined as the angle of the magnetic field with respect to the horizontal direction. The safety factor is defined as the number of toroidal transits necessary for one poloidal transit along the magnetic field line, $q = \frac{r B_\phi}{R B_\theta} \approx \frac{r}{R} \sin\left(\alpha_{\text{pitch}}\right)^{-1}$.

Physically, the plasma and its magnetic field can be described in a single-fluid picture that is governed by the ideal MHD equations [42, p.261]. A stationary equilibrium requires that no net forces act on the plasma. In the simplest picture, this condition is fulfilled when the $\vec{j} \times \vec{B}$-force balances the plasma pressure force, $\vec{j} \times \vec{B} = \vec{\nabla} p$. This implies that the magnetic field lines and the currents are constrained to surfaces of constant pressure. These flux surfaces are isomagnetic contours of toroidal and poloidal magnetic flux and can be labeled by it. Commonly used is the coordinate ϱ_{pol} that is defined as $\varrho_{\text{pol}} = \sqrt{\frac{\Psi - \Psi_{\text{sep}}}{\Psi_{\text{sep}} - \Psi_{\text{axis}}}}$, where Ψ is the poloidal magnetic flux and the subscripts *sep* and *axis* refer to the separatrix and the magnetic axis respectively. The separatrix is the last closed flux surface, LCFS, that separates the closed field lines in the confined plasma

region, i.e. the core, from the open field lines in the Scrape-Off Layer, SOL, see figure 1.3. The coordinate ϱ_{pol} is scaled such that $\varrho_{pol} = 0$ at the magnetic axis, $\varrho_{pol} = 1$ at the separatrix and $\varrho_{pol} > 1$ in the scrape-off layer.

1.4 Scrape Off Layer and Divertor

In a tokamak two major magnetic field geometries can be distinguished. The limiter (a) and the divertor configuration (b) are shown in figure 1.3. In limiter geometry the LCFS is determined by the tangential intersection of a particular magnetic flux surface with a material surface, which is called limiter. In figure 1.3.a the plasma is limited by the high field side heatshield. The limiter is in direct contact with the confined, hot plasma. Intense plasma-wall interaction in direct proximity to the core plasma is a consequence. The plasma density radially outward from the LCFS decreases monotonically, often exponentially, due to the separation of the fast parallel transport along magnetic field lines to the limiter and the slow perpendicular transport [48]. The limiter scrapes off the outermost plasma layers, hence the name Scrape-Off Layer. The SOL width, λ_{SOL}, is determined by the ratio of parallel to perpendicular transport.

In divertor geometry additional magnetic field coils produce a magnetic quadrupole field in the divertor, that introduces a so-called X-point, see figure 1.3.b, where the poloidal magnetic field vanishes. A last closed flux surface is generated magnetically and the core plasma is now confined without direct proximity of any material walls or direct connection to the walls along magnetic field lines. The separatrix legs in the divertor connect to the divertor target surface at the strikepoints. In the analysis of a divertor tokamak SOL some expressions are recurring. The midplane is the horizontal plane in the poloidal cross section that is at the height of either the geometric or the magnetic
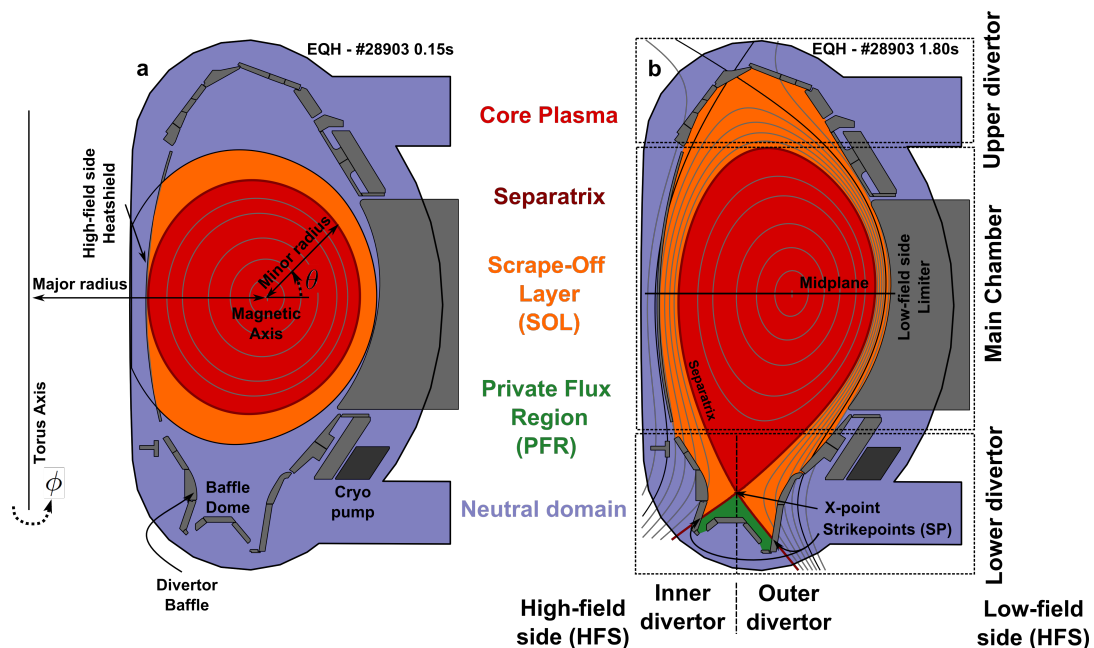

Figure 1.3: Limiter and divertor geometry of plasma and magnetic field.

axis. The outer midplane ($\theta = 0$) is often taken as a reference position and measurements at different poloidal positions ($\theta \neq 0$) are often mapped to this position along the field lines or according to their magnetic flux surface label (ϱ_{pol}) for comparison. The effective radial transport in a tokamak peaks at the outer midplane, where the plasma is most unstable [49, 50]. It is therefore often considered as the sole entry point of power and particles into the SOL in a simple analysis of the parallel SOL transport.

Despite rather short distances from a given point in the SOL to a material surface in the poloidal cross section in figure 1.3.b, the length along a magnetic field line, the so-called connection length, is of the order of 20–50 m in AUG [51]. The connection length from the midplane to the closest target is approximately $L_{\mathrm{c}} \approx \pi q R$. In the proximity of the X-point, where $B_\theta \to 0$ and hence $q \to \infty$, the connection length is significantly higher than in the far SOL. The introduction of a poloidal magnetic field null also increases the radial separation of flux surfaces, i.e. the magnetic flux expansion, in the divertor and especially at the X-point, see figure 1.4. The magnetic flux expansion is defined as $f_{\mathrm{x}} = \frac{l_{\mathrm{u}}}{l_{\mathrm{t}}} \approx \frac{B_{u,\theta}/B_{u,\phi}}{B_{t,\theta}/B_{t,\phi}}$ and is minimal at the outer midplane separatrix due to the Shafranov shift [42, p.272 ff]. As B_θ decreases, the magnetic flux expansion increases towards the X-point and then decreases again towards the target.

Figure 1.4: Flux expansion and magnetic field pitch angle in the SOL. Figure adapted from Ref. [48].

Plasma that is radially transported across the separatrix quickly travels along the field lines and impacts onto the divertor targets. The particles are neutralized at the material surface and are released as neutrals, a process called recycling. In the radial direction a separation of the SOL in the near and far SOL, relative to the separatrix, is often useful. Such a separation is not exact. The near SOL close to the separtrix is characterized by large power and particle fluxes. The strong peaking of the power and particle fluxes around the strikepoint at the target is a challenge for power exhaust, see chapter 4. The extent of the near SOL is mostly defined by the radial power fall off length, λ_{q}, that characterizes the exponential decay of the radial profile of the parallel power flux, $q_\parallel$.

The spatial separation of the material surfaces from the confined plasma in a divertor configuration and the fast parallel transport along the magnetic field into the divertor restrict the bulk of the plasma-wall interaction and the majority of the recycling to surfaces remote from the confined plasma. The formation of a divertor plasma between the X-point and the divertor targets provides additional options for power exhaust. Cold (< 5 eV) and dense ($> 10^{20}$ m^{-3})) divertor plasma provides efficient pumping through compression of neutrals in the divertor [52, 53] and ensures low erosion of the target material [54] as well as energy and particle loads that are compatible with the material limits [55]. Divertor optimization can be achieved by a number of adjustments, e.g. target geometry, impurity seeding, sweeping, etc.
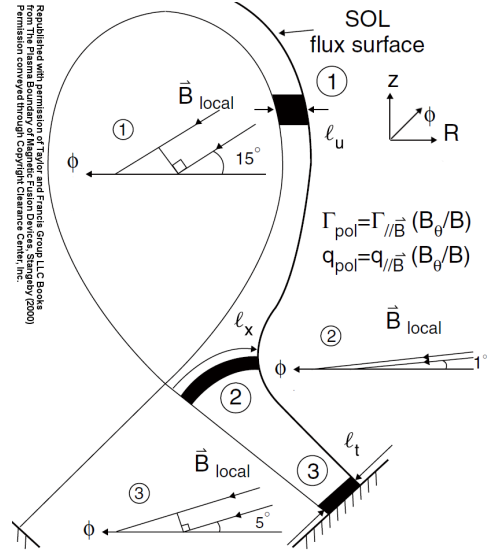
1.5 The High-Confinement Mode

A magnetically confined plasma in a tokamak exists in different modes, which results in different levels of confinement. Plasmas with a low level of confinement are called L-Modes. The first high-confinement mode, H-Mode, was discovered at AUG's predecessor ASDEX [56]. A sudden transition from the operation in L-Mode to H-mode occurs above a threshold for the heating power [57]. An edge transport barrier is established where turbulent, radial transport is suppressed by strong $\vec{E} \times \vec{B}$ shear flow [58, 59]. However, the formation of the H-Mode is not yet fully understood. Experiments show that the gradients in the confined regions inside the edge transport barrier are limited to a critical gradient, a property called stiffness [29, 60, 61]. With stiff core profiles, an increase of electron density and temperature in the pedestal region also influences the plasma center. An increase in confinement of typically about a factor of two is achieved in H-Mode compared to L-Mode [56]. H-Mode is the foreseen confinement scheme for future fusion devices like the international tokamak ITER [62]. This thesis will extend previous L-mode studies to high power H-mode conditions to ensure a sound extrapolation of the detachment physics and power exhaust to such devices.

A feature of H-modes are edge-localized modes, ELMs [63, 64]. ELMs are quasi-periodic, cyclic relaxations of the pedestal gradients in the electron density and the electron and ion temperature due to MHD instabilities of the pedestal. Such a crash of the pedestal expels energy and particles into the SOL and leads to transient heat and particle loads on the divertor targets, that can exceed the loads in between ELMs by orders of magnitude. ELMs therefore are a challenge for power exhaust and target materials. Fortunately, chapter 4 will show that puffing impurities in our discharges reduces the ELM size and can even lead to the suppression of ELMs.

The experimentally most relevant ELM-types in present day devices are type-I and type-III ELMs. Type-I ELMs can be explained in the framework of an ideal MHD instability, i.e. peeling-ballooning. The smaller type-III ELMs are likely to be resistive MHD instabilities [65]. An overview on ELMs can be found in Ref. [63]. The envisaged scenario for the larger, next-step device ITER is H-mode with type-I ELMs [62], but a limitation to smaller type-III ELMs has been proposed as well [66].

Although we focus here on H-mode phases in between ELMs, so-call inter-ELM time intervals, the bursts of energy and particles can have implications for the evaluation of diagnostics and the inter-ELM plasma equilibrium [67].

1.6 First Wall Material

In magnetic fusion devices the plasma resides in a vacuum vessel that is protected by plasma facing component, like limiters, shielding or a blanket. The material properties of these components of the first wall have to fulfill several requirements. They have to withstand high power fluxes of the order of 10 $\mathrm{MWm^{-2}}$ in steady-state and 1 $\mathrm{GWm^{-2}}$ for transient events lasting up to 1 ms [68] without major damage to wall material,

e.g. melting. Low erosion, i.e. low effective sputtering yields, high sputtering threshold and no chemical erosion, are required for long maintenance intervals, especially of the divertor. The effect of released wall material as a plasma impurity can have a detrimental effect on plasma performance, e.g. increased core radiation losses. Low co-deposition of radioactive material (tritium inventory) is necessary for operational safety and nuclear operation licenses.

In non-nuclear machines (D fuel) carbon is an optimal material choice [69–72], but nuclear safety regulations prohibit its use in a reactor due to the large retention of tritium within carbon [73]. A promising alternative wall material is tungsten [74]. Tungsten is a high-Z impurity with a large radiative loss function in the hot core plasma, see figure 1.6. The critical limit for the allowed tungsten concentration to achieve burn conditions, $Q > 1$, for ITER is $c_W = \frac{n_W}{n_e} \approx 5 \times 10^{-5}$ [34]. Thus, tungsten sources have to be minimized in the divertor, especially during ELMs, and at the main chamber walls [75, 76]. The physical sputtering threshold of tungsten is high and the sputtering yields are low even when sputtering caused by impurity ions is considered [54]. The decisive advantage of tungsten is the lack of co-deposition of tritium. The tritium retention in tungsten is small and compatible with the design of future fusion reactors [77, 78]. New tungsten mono block designs can withstand up to $20\,\mathrm{MWm^{-2}}$ of steady-state heat load [79]. However, in contrast to carbon, tungsten melts when its material limits are exceeded. Melt droplets can be a threat to a safe shutdown and can lead to disruptions. Melt damage might reduce the lifetime of wall material significantly and inhibit a continuation of operation after a melt event [80].

AUG was the first tokamak that changed from a full carbon wall to a full tungsten wall in order to test tungsten as first wall material under experimental reactor conditions [74, 81]. Recently, the Joint European Torus, JET, undertook a major overhaul that installed the so-called ITER-like wall with main chamber wall made from beryllium and a full tungsten divertor [82, 83].

1.7 Power Exhaust - A Challenge

In future fusion devices like ITER [62] and the demonstration reactor DEMO [84] power exhaust will be a challenge. Economic and technical considerations lead to a power plant size with a fusion power of $P_{\mathrm{fusion}} = 3\,\mathrm{GW}$ [85]. The fusion power is distributed inversely proportional to the mass ratio of the fusion products. The neutron will carry 80 %, P_{neut}, and the alpha-particle the remaining 20 %, P_α, of the fusion power. The neutrons are not confined by the magnetic field, their energy is distributed over the whole first wall and deposited volumetrically inside the blanket due to a finite penetration depth. The alpha particles are confined and transfer their energy to the plasma via collisions leading to the so-called alpha particle heating. Without volumetric losses, e.g. line and bremsstrahlung radiation, the alpha particle heating plus external heating power needs to be transported across the separatrix into the SOL leading to $P_{\mathrm{SOL}} \approx 650\,\mathrm{MW}$. A DEMO-like device has a major radius of about $R = 7\,\mathrm{m}$ [84]. With an inverse aspect ratio of $\varepsilon = a/R \approx 1/3$, the minor radius is about $a = 2\,\mathrm{m}$. Recent evaluation of experimental data suggest that the width of the power carrying layer in the SOL is $\lambda_q \approx 1\,\mathrm{mm}$ [86]. Assuming a safety

factor of $q = 3$ then leads to a parallel power flux at the midplane of:

$$q_{\parallel,\text{mid}} = \frac{P_{\text{SOL}}}{A_\perp} = \frac{P_{\text{SOL}}}{4\pi R \lambda_q \sin(\alpha_{\text{pitch}})} \approx 72 \text{ GWm}^{-2} \tag{1.3}$$

where $A_\perp$ is the projection of the SOL area perpendicular to the magnetic field lines and $\sin(\alpha_{\text{pitch}}) = B_\theta/B_\phi \approx 0.1$ is the sine of the magnetic field line pitch angle. This huge power flux propagates along the magnetic field lines into the divertor as shown in figure 1.5. Geometric effects such as magnetic flux expansion ($f_x \approx 5$) and targets tilted with respect to the magnetic field lines ($\sin(\alpha_t) \approx 0.05$) can achieve about a factor 100 reduction in the power flux [87]. The maximum magnetic flux expansion is set by the divertor geometry and the tolerable currents in the divertor field coils. The minimum $\alpha_t \geq 3°$ is set by the engineering limit of how well the divertor target structure can be

Figure 1.5: Power- and particle fluxes to be considered in the analysis of power exhaust and recycling.

aligned to the requested position. The divertor tiles are positioned such that they shadow adjacent tiles in the toroidal magnetic field direction to ensure that small misalignment of divertor tiles will not produce leading edges. Tilting the target decreases the effective target area, but leading edges would be subject to large heat- and particle fluxes with the potential for severe melt damage.

Taking into account the experimentally observed typical power sharing ratio between the outer and inner divertor of 2–3 in inter-ELM phases [88, 89], the outer target would receive a higher power flux of about $q_t = 480$–540 MWm^{-2}. This is still well above the specified material limits for the divertor target plates in steady-state, which are 10–20 MWm^{-2} for ITER [55, 79] and even lower for DEMO [79].

One possible approach to solve this problem is the distribution of the power, P_{SOL}, over larger areas of the vessel wall by increasing the electromagnetic radiation, which is distributed equally into the full 4π solid angle. The acceleration of the charged particles following the curved field lines leads to bremsstrahlung, P_{brems}. Neutral atoms and impurity ions that are not fully stripped of their electrons are excited in the plasma and emit line radiation, P_{line}. A complex collisional-radiative model [90] that calculates the excitation and de-excitation of the plasma particles can be condensed in a coronal quasi-equilibrium, i.e. at low densities [29], which allows to extract average charge states and an effective radiative cooling rate [91], L_Z. Such cooling rates are shown for hydrogen and several impurities in figure 1.6. The amount of energy lost due to line radiation of an ion species is given by $P_{\text{rad}} = n_e^2 c_Z L_Z [W]$. Non-coronal enhancement of the radiative loss function can occur at higher plasma densities that are present in a tokamak. The radiation potential of each ionization state is re-evaluated as an average potential includ-

ing re-neutralization with a frequency $1/\tau$ [92]. The effect of non-coronal enhancement of the radiative loss function for carbon is shown in figure 1.7.
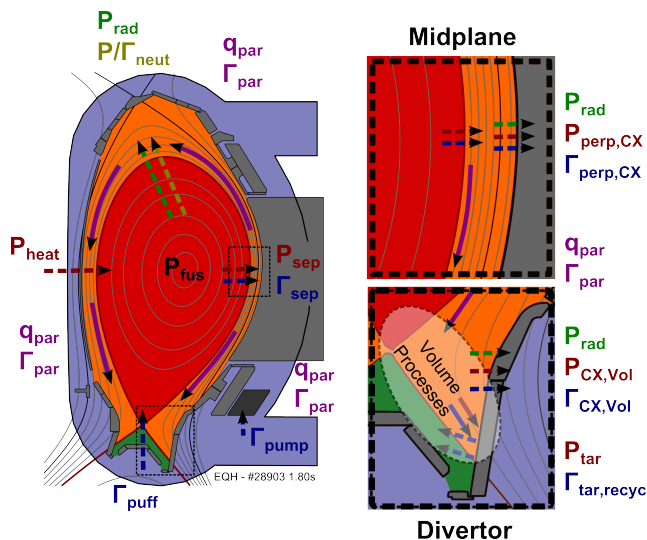
In steady-state the power balance of the confined plasma reads $P_\alpha + P_{\text{heat}} = P_{\text{neut}} + P_{\text{rad,core}} + P_{\text{SOL}}$ with $P_{\text{rad,core}} = P_{\text{brems}} + P_{\text{line}}$. Deliberate puffing, so-called seeding, of high-Z impurities like argon, krypton or xenon can be used to increase the radiation inside the confined plasma, the so-called core radiation [94, 95]. The radiative characteristic of high-Z impurities preferentially produces radiation losses in the hot, confined plasma region, see figure 1.6. The radiated power is distributed across the whole first wall and the power that enters the SOL is reduced. The amount of acceptable core radiation is limited by at least two requirements: First, if a DEMO-device is to be operated in H-mode the so-called L-H threshold needs to be taken into account [57]. The current interpretation of the L-H threshold is that a minimum power flow across the separatrix, $P_{\text{L-H}}$, is necessary to transit from L- to H-mode and stay in H-mode ($P_{\text{SOL}} \geq 1.2 P_{\text{L-H}}$). Second, the Lawson criterion needs to be fulfilled in oder to be able to achieve $Q > 10$. The impact of high-Z elements like tungsten, argon, krypton or xenon is two-fold negative: One, they not only dilute the plasma stronger due to higher average charge states, but also tend to accumulate in the center of the plasma. Two, radiation losses from the core by line radiation cools the core plasma and can terminate the plasma in a disruption [34]. The sensitivity of the available operational space to different kinds of impurities is strongly varying [34].

Figure 1.6: Radiation loss function in coronal equilibrium [89].
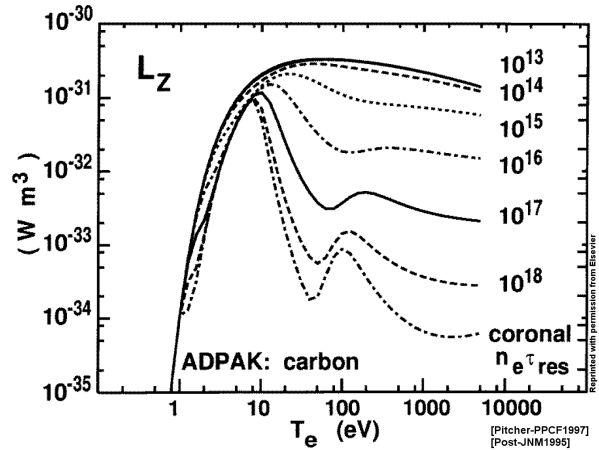
Figure 1.7: Radiation loss function of carbon. Non-coronal enhancement with parameter $n_e\tau$ increases L_Z [93].

In DEMO 70 % of the alpha heating power, P_H, are foreseen to be exhausted via radiation in the confined region by seeding of high-Z impurities [92]. The remaining power is exhausted into the SOL and needs to be reduced by SOL and divertor radiation in order to ensure operation with total radiated power fractions, $f_{\text{rad}} = P_{\text{rad}}/P_H$, above 95 %. In contrast to high-Z elements, low- to medium-Z elements like nitrogen and neon are used to control the SOL (Ne) and divertor (N_2) radiation [96, 97]. The limit for the use of such impurities is set by the maximum allowed fuel dilution in connection with the

ability of the divertor to confine the impurities, i.e. divertor retention [98], and a possible saturation of the divertor radiation [97, 99].
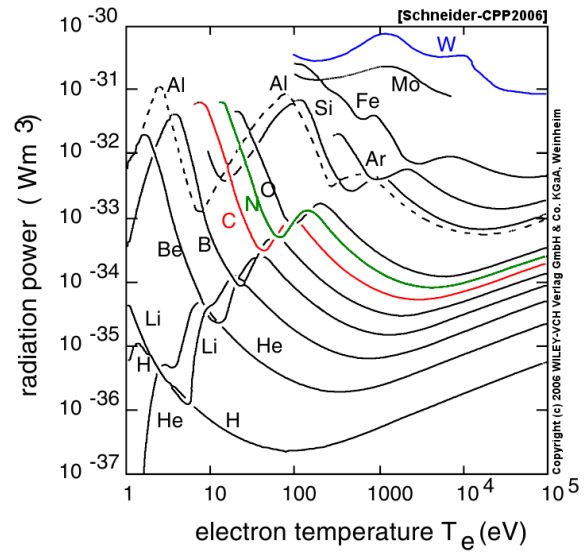
Radiation in the divertor has several beneficial effects. First, it reduces the heat flux to the divertor target. Second, the energy loss along a field line leads to a temperature gradient in the parallel direction. With pressure conservation along a flux tube the density increases towards the target, which in turn increases the amount of radiation. Low divertor temperatures also increase the perpendicular broadening of heat flux profile at the targets [100]. Third, for chemically inactive target materials, like tungsten, the reduction of the temperature at the target will reduce or suppress additional impurity production by sputtering. Finally, the decrease in temperature and increase in density opens up new volumetric loss channels like charge-exchange with neutrals and recombination. Both can lead to a plasma pressure loss and ultimately to detachment of the plasma from the target.

1.8 Scope of Thesis & Key Results & Structure

A good characterization and understanding of divertor detachment is crucial in order to test the theoretical models for a possible extrapolation of detachment to future devices like ITER and DEMO. Detachment physics in L-mode [101, 102] and radiative power exhaust scenarios using impurity seeding have been a focus on AUG [92, 96, 103, 104]. This thesis extends the investigations for the first time to complete detachment in high power H-mode discharges with nitrogen seeding in AUG with a full tungsten wall.

In the course of this work, the first stable, completely detached H-mode discharges have been achieved in full tungsten AUG. The experiments showed for the first time that with nitrogen seeding an intense, localized radiation at the X-point inside the confined plasma is intimately coupled to complete detachment in full tungsten AUG. The X-point radiation is stable, reproducible and reversible. In contrast to studies in AUG with a carbon wall [105, 106], complete detachment of the outer target is not associated with the occurrence of an H-mode density limit [103]. The completely detached H-mode discharges feature good confinement properties and the X-point radiation has a beneficial impact on the detachment properties. The discovered plasma scenario seems to be a very interesting candidate for a future fusion device if the observations can be extrapolated to the necessary plasma parameters.

The experimental efforts are accompanied by extensive modeling with the numerical code package SOLPS [89] in order to test its ability to reproduce the experimental observations with recent theoretical models and to gain a better understanding of the complex physical mechanisms that govern the detachment process. It has been possible to qualitatively reproduce the experimental observations in the numerical modeling. The quality of the detailed match of these simulations with the experimental measurements for such H-mode simulations is a novelty. The modeling was able to confirm the suggested experimental conclusions and to clarify which physical processes are relevant for the detachment process.

Following this introduction, a basic theoretical model for the analysis of the SOL and the

detachment process is presented in chapter 2 and the physics of detachment is discussed. The tokamak ASDEX Upgrade and diagnostics that are important for the evaluation of the experiments are introduced in chapter 3. The experimental studies and the detailed experimental observations are summarized in chapter 4. In chapter 5 the modeling of these discharges with SOLPS is presented. Finally, a discussion about the results and concluding remarks are given in chapter 6.

CHAPTER 2

Detachment Physics

This chapter introduces a simple model for the SOL and the divertor plasmas - the Two Point Model [48], TPM, and elucidates the transition to a more complex approach with numerical computer codes for 2D and 3D simulations. This section includes material from Refs. [2, 48, 101, 107, 108].

2.1 Simple Two Point Model - SOL Transport Analysis

2.1.1 Basic Parameters

The Braginskii equations describe the parallel heat transport in the SOL as a combination of conduction and convection by electrons and ions [108]:

$$
q_{\parallel,\mathrm{e}} = \frac{5}{2} T_\mathrm{e} n_\mathrm{e} u_\mathrm{e} \\
- \kappa_{0,\mathrm{e}} T_\mathrm{e}^{5/2} \frac{\mathrm{d}T_\mathrm{e}}{\mathrm{d}s}
\tag{2.1}
$$

where the kinetic energy of the mean flow of electrons is neglected. For the ion heat flux this is not appropriate due to $m_\mathrm{i}/m_\mathrm{e} \gg 1$.

$$
q_{\parallel,\mathrm{i}} = \left(\frac{1}{2} m_\mathrm{i} u_\mathrm{i}^2 + \frac{5}{2} T_\mathrm{i} \right) n_\mathrm{i} u_\mathrm{i} \\
- \kappa_{0,\mathrm{i}} T_\mathrm{i}^{5/2} \frac{\mathrm{d}T_\mathrm{i}}{\mathrm{d}s}
\tag{2.2}
$$

Figure 2.1: The SOL analysis in a 1D simplified geometry.

where the Spitzer-Härm heat conductivity κ_0 is given in (5.7). Heat transport in (2.1) and (2.2) is convective for the first and conductive for the second term. The equations imply that conductive heat transport
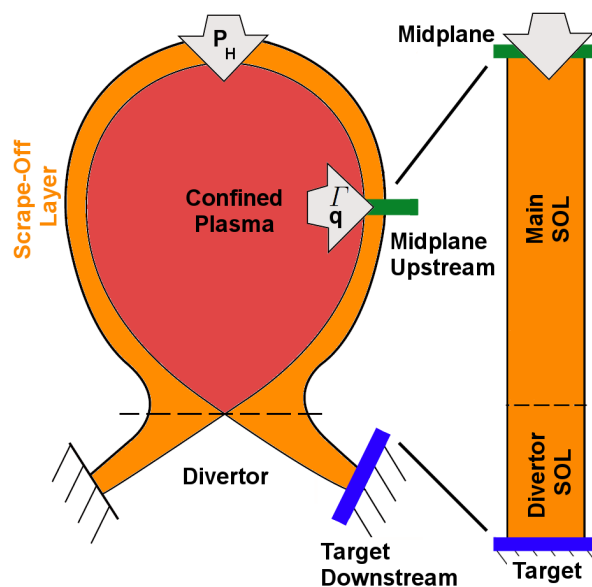
is dominated by the electrons as $\kappa_{0,\mathrm{e}} \gg \kappa_{0,\mathrm{i}}$, whereas in a convective SOL the ions are dominant as $u_\mathrm{e} \approx u_\mathrm{i}$ due to ambipolarity of the particle flux.

At the plasma-wall interface the parallel fluxes are transmitted through the sheath. The sheath is a thin boundary layer with a parallel extension of the order of the Debye length $\lambda_\mathrm{D} = \sqrt{\varepsilon_0 T_\mathrm{e}/e^2 n_\mathrm{e}}$ in front of the plasma-solid interface at the target. On the Debye scale the plasma is quasi-neutral and electrons are free to move along the magnetic field. Their larger mobility compared to ions ($\propto \sqrt{m_\mathrm{i}/m_\mathrm{e}}$) results in a negatively charged target surface. A potential drop in front of the target is the consequence. This so-called sheath potential accelerates ions towards the surface and repels electrons

Figure 2.2: The structure of the sheath in front of a target surface with an oblique magnetic field and its influence on electron and ion trajectories is shown. Figure adapted from Ref. [48].

such that the outflux of electrons and ions is ambipolar. A presheath acceleration of ions to velocities $v \geq c_\mathrm{s}$ was derived by Bohm without magnetic fields [109, 110]. Chordura introduced a magnetic presheath, that is of dimension of the ion gyro radius, r_g, to extend the analysis to cases with a magnetic field at oblique angles of incidence at the target. The generalized boundary condition is known as the Bohm-Chordura criterion [111, 112], which states that the ion flow velocity u_i has to exceed the local sound speed at the sheath entrance.

$$u_\mathrm{i}^2 \geq c_\mathrm{s}^2 = \frac{(Z_\mathrm{eff} T_\mathrm{e} + \gamma T_\mathrm{i})}{m_\mathrm{i}} \tag{2.3}$$

where c_s is the ion sound speed, Z_eff is the average charge state [29] and γ is the ratio of specific heats with $\gamma = 1$ for isothermal flow, $\gamma = 5/3$ for adiabatic flow with isotropic pressure and $\gamma = 3$ for one-dimensional adiabatic flow. Including drift effects requires a modification of the Bohm criterion due to $\vec{E} \times \vec{B}$ drifts [113].

$$M_\mathrm{out/in} = \left(\frac{u}{c_\mathrm{s}}\right)_\mathrm{out/in} \geq 1 \pm \frac{E_\mathrm{r}}{B_\theta c_\mathrm{s}} \tag{2.4}$$

Addtional effects have also been considered [114]. To fulfill the Bohm criterion ions need to be accelerated towards the targets by a presheath potential in the SOL. The presheath potential drop for isothermal flow can be approximated by $\Phi_\mathrm{pre} \approx -0.7\frac{T_\mathrm{e}}{e}$ [48, p.48]. Neglecting radiation, the power deposited onto the target is given by the sheath theory. The ability to transmit energy through the sheath is characterized by the sheath heat transmission factor, γ_sh, and the target heat flux can be expressed as

$$q_\mathrm{t} = \gamma_\mathrm{sh} \underbrace{n_\mathrm{e,t} c_\mathrm{s} T_\mathrm{e,t}}_{\propto p_\mathrm{e} T_\mathrm{e}^{1/2}} + \underbrace{n_\mathrm{e,t} c_\mathrm{s}}_{\propto p_\mathrm{e} T_\mathrm{e}^{-1/2}} E_\mathrm{pot} = \Gamma_\mathrm{t}\left(\gamma_\mathrm{sh} T_\mathrm{e,t} + E_\mathrm{pot}\right) = \gamma_\mathrm{sh}^* \Gamma_\mathrm{t} \tag{2.5}$$

where $\gamma_\mathrm{sh} \approx 8$ [115] is the sheath heat transmission coefficient and $E_\mathrm{pot} \approx E_\mathrm{pot,i} + E_\mathrm{pot,r} =$
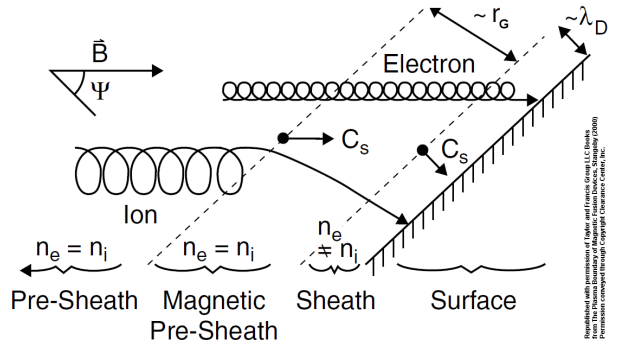
15.8 eV is the potential energy that a deuterium ion will release on the target when recombining to a deuterium molecule [55, 116]. A more complete description of the sheath heat transmission factor, including particle and energy reflection at the target and secondary electron emission, can be found in [116].

$$
\gamma_s^* \approx \left(\frac{2.5 T_i}{Z_{eff} T_e} - 0.5 \ln \left[\left(2\pi \frac{m_e}{m_i} \right) \left(Z_{eff} + \frac{T_i}{T_e} \right) (1 - \delta_e) \right] \right) (1 - R_{iE})
$$
$$
+ \frac{2}{1 - \delta_e} (1 - R_{eE}) + \varepsilon_{pre} + \frac{E_{pot,i}}{T_e} + \frac{E_{pot,r}}{T_e} (1 - R_{iN})
\tag{2.6}
$$

where δ_e is the secondary electron emission coefficient, $R_{i/eE}$ is the energy reflection coefficient, ε_{pre} is the energy gain in the presheath and $E_{pot,i/r}$ are the energies per ion for recombination (13.6 eV for D) and molecule formation (2.2 eV for D_2). Assuming $T_i = T_e$, $\delta_e = 0$, $Z_{eff} = 1$ (pure D) and $\varepsilon_{pre} = R_x = E_{pot,x} = 0$, results in $\gamma_s = 7$–8. Experimentally measured sheath heat transmission coefficients range from 5.5–12.5 [115, 116].

The analysis of the SOL transport is started with a simplified 0D model that derives from the 1D conservations equations with the spatial coordinate s being the parallel distance along the field line. This Two-Point Model, TPM, describes the interconnection of the target plasma parameters with the upstream plasma and external control parameters such as heating power and fueling. Integrating the 0D equations one can reconstruct 1D parallel profiles. Only one flux tube adjacent to the separatrix is considered and cross field transport is neglected [48].

2.1.2 Sheath Limited Regime

In the sheath-limited regime ion-ization in the divertor is small (low recycling) compared to the particle source due to cross field transport from the main plasma across the separatrix. All particles and the power enter the SOL upstream at the stagnation point close to the outer midplane and flow downstream to the target plate. The stagnating plasma flow upstream is accelerated to sound speed at the target to meet the Bohm criterion. The

Figure 2.3: The SOL collisionality is the ordering parameter that determines the dominant SOL regime. Figure adapted from Ref. [48].

sheath heat transmission factor determines the parallel heat flux through the SOL. Most of the power is convected and the temperature gradient in the SOL is small such that $T_t \approx T_u = T$ can be assumed. The sheath limited regime occurs only at low collisionality, see figure 2.3, and hence low upstream densities. This implies that volumetric processes
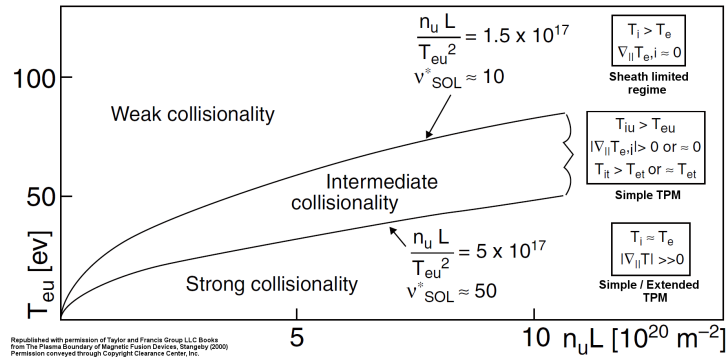
are negligible and hence total pressure is conserved along a flux tube.

$$2n_\text{u}T = \underbrace{2n_\text{t}T}_{\text{stat.pressure}} + \underbrace{2m_\text{i}n_\text{t}c_\text{s}^2}_{\text{dyn.pressure}} \Rightarrow n_\text{t} = \frac{1}{2}n_\text{u} \tag{2.7}$$

where we used $u_\text{u} = 0$, $u_\text{t} = c_\text{s} = \sqrt{\frac{2T}{m_\text{i}}}$. Equations (2.5) and (2.7) can be solved for T. A two-point model gives the target parameters depending on experimental control parameters like heating power $P_\text{H} \propto q_\parallel$ and upstream density or line integrated density $\overline{n} \approx 3n_\text{u}$ [117]. The particle flux to the target is calculated from $\Gamma_\text{t} = n_\text{t}c_\text{s}$.

$$T \approx \frac{1}{2}m_\text{e}^{1/3}\left(\frac{q_\parallel}{\gamma_\text{sh}n_\text{u}}\right)^{2/3} \quad \& \quad \Gamma_\text{t} = \frac{1}{2}m_\text{e}^{-1/3}\left(\frac{q_\parallel n_\text{u}^2}{\gamma_\text{sh}}\right)^{1/3} \tag{2.8}$$

2.1.3 Conduction Limited Regime

At higher collisionalities, i.e. higher density, the heat transport in the SOL will change from convective to conduction dominated. A temperature gradient along the magnetic field lines from upstream to target arises. In the conduction limited regime the ionization of the recycling neutrals in the divertor is the dominant particle source in the divertor (high recycling). Volumetric processes can still be neglected - except for ionization and radiation losses by deuterium[1]. The particle flow in the SOL is driven by sources [48, p.34] and hence the SOL will be stagnant down to the ionization region directly in front of the target. The Bohm criterion at the target is still valid. With these assumptions the Two-Point Model [118] can be derived as a set of equations [48, p.224].

$$\begin{aligned} 2n_\text{t}T_\text{t} &= n_\text{u}T_\text{u} \\ T_\text{u}^{7/2} &= T_\text{t}^{7/2} + \frac{7}{2}\frac{q_\parallel L_\text{c}}{\kappa_{0,\text{e}}} \approx \frac{7}{2}\frac{q_\parallel L_\text{c}}{\kappa_{0,\text{e}}} \\ q_\parallel &= \gamma_\text{sh}n_\text{t}T_\text{t}c_\text{s} \end{aligned} \tag{2.9}$$

Solving these equations gives [48, 93]

$$\begin{aligned} T_\text{t} &\propto n_\text{u}^{-2}q_\parallel^{10/7}L_\text{c}^{-4/7} & n_\text{t} &\propto n_\text{u}^3 q_\parallel^{-8/7}L_\text{c}^{6/7} \\ \Gamma_\text{t} &\propto n_\text{u}^2 q_\parallel^{-3/7}L_\text{c}^{4/7} & T_\text{u}/T_\text{t} &\propto n^2 q_\parallel^{-8/7}L_\text{c}^{6/7} \end{aligned} \tag{2.10}$$

From (2.9) and (2.10) follows that the most severe impact on divertor conditions is the variation of the upstream density. The upstream temperature is very insensitive to any external changes, i.e. heating power or connection length. The high recycling regime exhibits significant parallel temperature gradients in the SOL and target temperatures of as low as several eV can be reached. In present day devices the high recycling regime is sufficient for target heat flux protection as explained in section 1.7. A prerequisite

---

1 The radiation losses per ionization of a deuterium atom can be taken approximately as constant. It increases the ionization energy to an effective ionization energy with values of 30–50 eV [48, p.145]

for the high recycling regime is sufficiently high collisionality, hence density, in the SOL for strong parallel temperature gradients to occur, see figure 2.3. The simple TPM is valid in the conduction limited attached regime when cross field transport and volume processes can be neglected. No pressure loss along a field line occurs and the divertor is attached.

2.2 Extended Two Point Model - Including Volumetric Processes

At even higher densities the divertor exhibits strong radiation cooling in high recycling and can even start to detach. Seeding of extrinsic impurities like nitrogen can further this effect. An extended TPM [48, p.232] is necessary to account for the volume processes that can transport energy, momentum and particles out of a flux tube. Cross field transport can in principle be absorbed in these loss factors as well.

2.2.1 Volumetric Processes - Loss Factors

Allowing for energy loss from radiation and from charge exchange collisions with neutrals a volumetric energy loss factor f_{rad} can be defined to modify the heat flux at the target

$$q_{\text{t},\parallel} = q_\parallel - (q_{\text{rad}} + q_{\text{CX}}) = (1 - f_{\text{power}})\, q_\parallel \tag{2.11}$$

Charge exchange reactions will not only transport energy, but also momentum out of a flux tube. In addition, viscous stress, recombination and friction can contribute to the volumetric momentum or pressure loss, that can be accounted for by a volumetric momentum loss factor f_{mom}. The pressure balance is modified to

$$p_{\text{t}} = \frac{1}{2} f_{\text{mom}} p_{\text{u}} \tag{2.12}$$

Low divertor temperatures will result in deeper penetration of recycling neutrals into the plasma and the assumption of ionization directly in front of the target plate is not valid anymore. A more wide-spread distribution of ionization in the divertor allows for a more complicated flow pattern then assumed for the simple TPM. Plasma flows in the divertor will increase the amount of convected power, that can be taken into account by separating conducted and convected power with the loss factor f_{cond}

$$q_{\parallel,\text{cond}} = f_{\text{cond}} q_\parallel \quad \& \quad q_{\parallel,\text{conv}} = (1 - f_{\text{cond}})\, q_\parallel \tag{2.13}$$

The additional loss factors result in additional proportionalities [48, 93, 101]

$$
\begin{aligned}
T_{\text{t}} &\propto \frac{(1 - f_{\text{pow}})^2}{f_{\text{mom}}^2 f_{\text{cond}}^{4/7}} & n_{\text{t}} &\propto \frac{f_{\text{mom}}^3 f_{\text{cond}}^{6/7}}{(1 - f_{\text{pow}})^2} \\
\Gamma_{\text{t}} &\propto \frac{f_{\text{mom}}^2 f_{\text{cond}}^{4/7}}{1 - f_{\text{pow}}} & T_{\text{u}}/T_{\text{t}} &\propto \frac{f_{\text{mom}}^2 f_{\text{cond}}^{6/7}}{(1 - f_{\text{pow}})^2}
\end{aligned}
\tag{2.14}
$$

The loss factors themselves strongly depend on the electron density and temperature in the divertor plasma. A simple valid parameterization of the loss factors in an analytical form is not to be expected and the TPM equations cannot be solved analytically anymore. Any realistic description will result in a highly non-linear system, which has immediate consequences for the stability of a divertor plasma solution as discussed e.g. in Ref. [119].

A desirable consequence of the volumetric losses is the possibility to reduce the plasma pressure along a field line. With a reduction of the plasma pressure, power and particle fluxes to the targets are lowered and the plasma detaches from the material surfaces.

2.2.2 Detachment Classification

We distinguish between power detachment, a reduction in heat load, and particle detachment, a reduction of particle flux to the target. In present day devices power detachment can be achieved in the high-recycling regime due to the reduction of T_t via (impurity) radiation and ionization energy losses. A value of $T_t \approx 5$ eV suffices for target protection at the observed densities in devices like AUG. Higher P_{SOL} in ITER and DEMO implies higher recycling, hence higher n_t and higher fluxes onto the divertor plate [120]. As discussed in section 2.3, for $T_t < 2$ eV the potential energy flux exceeds the thermal energy flux at the target and a reduction and/or limitation of the particle flux, i.e. particle detachment, becomes a prerequisite for power handling [55].

Partial detachment is defined as a parallel pressure loss at and close to the strikepoint [121]. In AUG a good indicator for partial detachment of the outer target is a drop of the control signal T_{div} below 5 eV. The signal T_{div} is derived from shunt current measurements at the target [122]. Complete detachment is defined as strong parallel pressure loss and close to flat profiles of the ion saturation current, j_{sat}, and electron temperature, T_t, along a large portion of the target [123]. The peak heat and particle fluxes are reduced by more than one order of magnitude compared to attached conditions with identical upstream parameters. In AUG a significant reduction in j_{sat} is typically observed along the target up to a distance from the strikepoint of $\Delta S = 10\text{–}15$ cm. The profiles in the far SOL at the outer target ($\Delta S > 15$ cm) show already low particle fluxes and temperatures even in attached conditions and are only marginally affected. For a completely detached outer target the controller T_{div} ranges from -5 to 0 eV.

Figure 2.4: Schematic description of the low-field side Scrape-off Layer unfolded in a TPM approach into a 1D slab.

An easily accessible, experimental measure for the degree of detachment, DOD, results from the comparison of the fluxes onto the target as obtained from experiment, Γ_{exp},
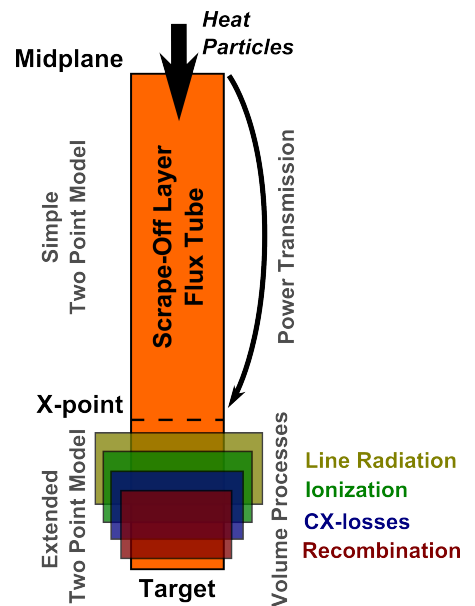
and from a TPM scaling, Γ_{TPM} [124].

$$\text{DOD} = \frac{\Gamma_{\text{TPM}}}{\Gamma_{\text{exp}}} \approx c\,\frac{\overline{n}_e^2}{\Gamma_{\text{exp}}} \tag{2.15}$$

where c is a constant and $\overline{n}$ is the line integrated electron density. Γ_{exp} is usually taken from the sum of the ion saturation current measurements by Langmuir probes at the target and Γ_{TPM} is a scaling of the particle flux to the target based on (2.10). Most often, only the scaling $\Gamma_{\text{TPM}} = cn_u^2$ is used. The constant, c, is determined assuming $\Gamma_{\text{TPM}} = \Gamma_{\text{exp}}$ for a well attached target condition during the experiment. A divertor target is considered detached if $\text{DOD} \gg 1$.

2.2.3 The Detachment Process

As shown in figure 2.4 four different regions or fronts are stacked along the parallel direction as the plasma temperature decreases from upstream to the target in a detached divertor. The location and extent of these regions is defined by the temperature distribution in the divertor and the dependence of the reaction rates for (impurity) line emission, ionization, charge-exchange and recombination on the plasma parameters. Figure 2.5 shows the reaction rates for ionization, recombination and charge exchange in a deuterium plasma with different electron densities. Above $T_e = 10$ eV ionization dominates over recombination and the plasma is called ionizing. The neutral densities will generally be low. Below $T_e = 5$ eV the charge exchange rate is larger by about a magnitude than that for ionization. A significant number of CX collisions per ionization can effectively transport momentum and energy away from flux tubes. Below 1.5 eV recombination finally dominates over ionization. The electron density is reduced, the neutral density increased and the plasma is called recombining.

Plasma pressure removal is possible by three principle means. One is charge exchange collisions with neutrals with subsequent escape of the neutrals from the con-

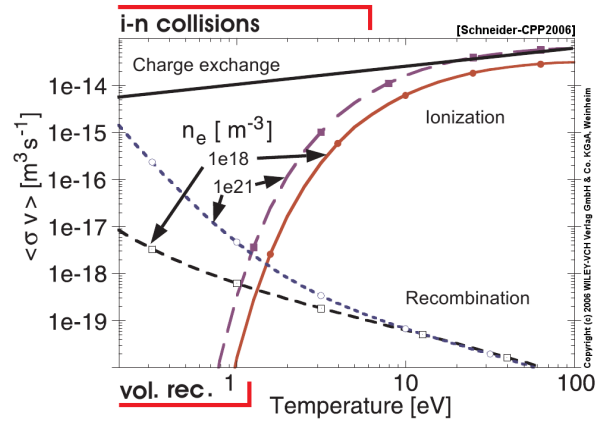
Figure 2.5: Rate coefficients for deuterium reactions assuming $T_e = T_i = T_H$ [89].
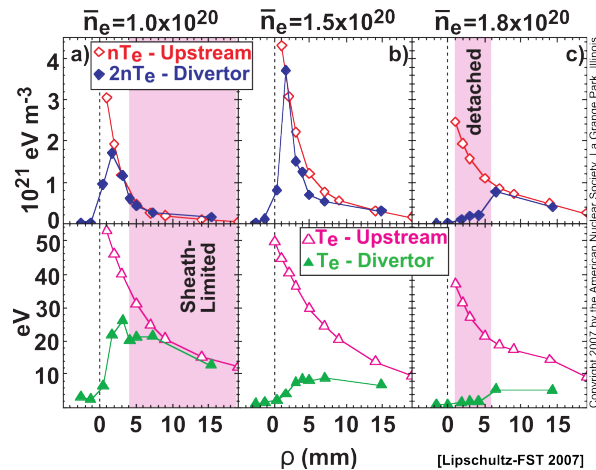

Figure 2.6: Evolution of the pressure balance (top) and the parallel temperature drop (bottom) during a density ramp experiment at C-mod [125, 126].

sidered region. A second is plasma recombination and a subsequent escape of the neutrals from the considered region. And a third is cross field transport out of the considered region. The first two can be increased voluntarily by a reduction of the divertor temperature. The most common approach to detachment in L-mode plasmas is a ramp of the upstream density via a deuterium fueling ramp. Up to the detached phase of figure 2.7 the pressure is still conserved on a flux tube (C) and increasing density (A) implies a drop in the temperature (B). Higher density in the divertor also leads to higher recycling and higher neutral density, which entrails increased radiative losses by deuterium line radiation (E). At target electron temperatures of about 5 eV and high neutral and plasma densities, momentum losses via charge-exchange are able to reduce the local pressure close to the target. A recombination zone in front of the target can be established in AUG at highest densities [127]. The evolution of the target and the upstream profiles for such a scan at the C-mod tokamak are shown in figure 2.6.

The use of such fueling ramp approaches for detachment studies is limited, especially for H-modes. The maximum achievable upstream density at a given power into the SOL is set either by the H-mode density limit [57,103] or the empirical density limit (Greenwald limit) [128]. At higher heating powers it can occur that the maximum achievable upstream density is not high enough to reach sufficiently low divertor temperatures for detachment to occur. An alternative route to detachment is to generate increased volumetric power loss in the SOL and divertor by line radiation of seeded, extrinsic impurities like nitrogen. Examining the extended TPM, (2.14), the power loss, $f_{pow} > 0$, lowers the divertor plasma temperature and reduces the power flux onto the target. At lower temperatures below 5 eV charge exchange processes can dominate over ionization in between the target and the radiation region. Momentum is transported out of the flux tubes, f_{mom}, and the pressure is reduced, i.e. the plasma starts to detach. Provided that the plasma flow velocities are low enough, a recombination front can form, see section 2.3. An examination of the routes to detachment has been carried out in [87].

In the JET tokamak [129] and in AUG with a full carbon wall (prior 2003) [81] complete detachment in H-mode with deuterium fueling only has been observed. Deuterium fueling ramp experiments in H-mode in AUG with a full tungsten wall so far produced at the

Figure 2.7: Density ramp with detachment in full-C AUG [93].

most partially detached outer targets. At heating powers between 5.0–12.5 MW even H-mode density limit experiments with the maximum deuterium fueling rates possible [103] did not achieve complete detachment of the outer target before the H-L backtransition. This thesis showed that strong extrinsic impurity seeding is able to achieve completely
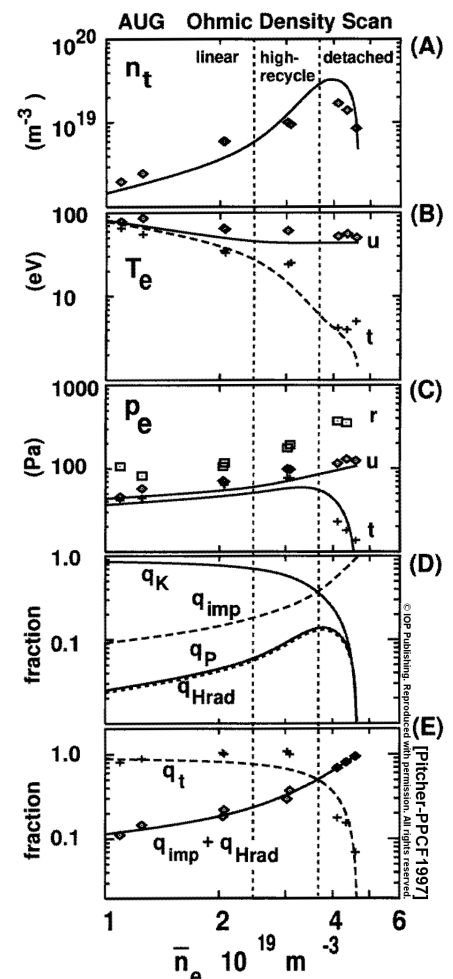
detached H-mode discharges in AUG with a full tungsten wall. Most likely, this is due to the fact that the power losses from deuterium line radiation and ionization alone are not enough to cool the divertor plasma sufficiently to reach temperatures relevant for charge exchange and recombination to occur. Impurity line radiation from extrinsic seeding (full W AUG) or intrinsic impurity sources (full C AUG) can supply the necessary additional power losses.

2.3 Discussion of Detachment

Partial vs. Complete Detachment

A general observation in experiments is that detachment does not occur uniformly along the divertor target, but rather concentrated at the strikepoint, see figure 2.6. In experiments with a deuterium fueling ramp (L-mode) or seeding ramps (H-mode) the local ion saturation flux to the target at the strikepoint rolls over before the integral target flux [55, 104, 124]. The pressure loss at the strikepoint can be orders of magnitude larger than in the far SOL, where the target conditions hardly change even in completely detached conditions, see chapter 4. The preferential detachment at the strikepoint can be undertstood with the (extended) TPM. The available parallel power in the far SOL is significantly lower. As a consequence, the recycling level and the electron density are reduced: Local ionization, radiation losses and charge exchange losses are lower. At the low collisionalities in the far SOL the convective power transmission dominates, i.e. parallel temperature gradients are smaller. The formation of temperature regions where additional power losses, e.g. line radiation, can open the route to detachment is hampered. In addition, cross transport into the private flux region, increased connection length and flux expansion (volume) at the X-point and momentum trapping can facilitate detachment at the strikepoint [131, p.862]. Lately, an increase in cross field transport at the X-point due to low values of β_p has also been discussed [132]. Fortunately, the target conditions in the far SOL are not an issue for material limits.

Power vs. Particle Detachment

If we assume a coupling of the ion and the electron temperature in front of the divertor target ($T_e = cT_i$), neglect a parallel pressure loss and use $\Gamma_t = n_t c_s \propto T_t^{-1/2}$, the target heat flux in (2.5) can be rewritten as

$$q_t \propto p_t(T_t^{1/2} + E_{pot}T_t^{-1/2}) \tag{2.16}$$

The first term is the kinetic energy flux and the second term is the flux of potential energy that will be released at the target when ions recombine to atoms and molecules. A power reduction at the target can be brought about by a decrease in the temperature until the potential energy flux dominates over the kinetic energy flux. Further reduction of the temperature beyond this point would increase the target heat flux again due to an increase in the particle flux.

If we now investigate the impact of volumetric losses on the target heat flux we have to

allow for parallel pressure losses in (2.5) and we get

$$q_{\text{t}} \propto n_{\text{t}}(T_{\text{t}}^{3/2} + E_{\text{pot}}T_{\text{e}}^{1/2}) \tag{2.17}$$

Using (2.14), we find that in the kinetic dominated regime ($T_{\text{e}} > 2$ eV) only the power loss, f_{pow}, has an impact on the target heat flux $q_{\text{t}} \propto (1 - f_{\text{pow}})$. In the potential energy dominated regime ($T_{\text{e}} < 2$ eV) we have $q_{\text{t}} \propto f_{\text{mom}}^2(1 - f_{\text{pow}})^{-1}$. A further increase in f_{pow} would be harmful, especially at high f_{pow} that is already necessary to reach the low temperatures of the potential energy dominated regime. However, at these low temperatures and high densities momentum losses, f_{mom}, will reduce the target fluxes.

It is shown that for a limitation of the target heat flux two things are required: First, high power losses (f_{pow}) that limit the kinetic heat flux and second, significant momentum losses (f_{mom}) that limit the potential energy flux. A more detailed analysis of the radiation characteristics of pure deuterium shows that without pressure losses the radiation cooling results in a minimum achievable temperature of about 4 eV [93, 133].

Charge Exchange vs. Volume Recombination

This paragraph discusses the importance of different physical processes for the necessary limitation of the particle flux to the target. At fixed power into the SOL and fixed upstream density, a target particle flux reduction can be achieved by momentum removal in the SOL, $f_{\text{mom}} > 0$, changing the ratio of conducted to convected heat transport, $f_{\text{cond}} < 1$, or perpendicular transport of particles. As discussed above, reducing the power losses is no option due to power flux and temperature constraints at the divertor plate. A significant part of convected power can only be desirable at already very low temperatures, where charge exchange and recombination are not inhibited. In addition, the necessary flow velocity should be small enough to ensure large transit times that are necessary for recombination, see below. Presently, the diagnostic capabilities are limited for the analysis of the convective transport due to a lack of parallel temperature profiles. In the future additional diagnostic capabilities could enable an experimental quantification of its impact on detachment [134, 135]. Perpendicular transport of particles is not part of the TPM and will be discussed in chapter 5. The focus in here is set on the enhancement of momentum losses for the particle flux reduction.

Important mechanisms that remove momentum are (in)elastic ion-neutral collisions, charge exchange collisions and recombination. An approximate description of the momentum loss factor due to charge exchange is given in [107, 133, 136] $f_{\text{mom}} = 2 \left(\frac{\alpha}{\alpha+1}\right)^{\frac{\alpha+1}{2}}$ with $\alpha = \frac{\langle\sigma v\rangle_{\text{ion}}}{\langle\sigma v\rangle_{\text{ion}} + \langle\sigma v\rangle_{\text{mom}}}$. A comparison of the pressure losses derived from this description using reaction rates from the ADAS database [137] and from experiments in the C-mod tokamak is shown in figure 2.8. The momentum loss expression neglects momentum losses due to recombination and does not take into account the actual momentum transport by neutrals. Recombination would increase the amount of reactions that lead to a momentum loss to neutrals. The analysis of neutral transport reveals that, once the neutrals are accelerated to the ion flow speed, additional collisions will transfer little momentum from ions to neutrals, i.e. momentum trapping [131].

It has to be noted that charge exchange or ion-neutral collisions both constitute a loss of momentum and energy for the ions. Such collisions will therefore contribute to both

f_{pow} and f_{mom} simultaneously. Both loss factors have an opposite effect on the target parameters in (2.14) and there could be critical plasma parameters at which charge exchange reactions change from decreasing to increasing the target particle flux.

It has been debated if charge exchange alone is sufficient for complete detachment of the divertor targets or if volumetric recombination is required. Simulations of ITER indicate that volume recombination is necessary for complete detachment [138–144]. Simulations of JET with nitrogen impurity seeding show that significant pressure loss along field lines can also be achieved when volume recombination is neglected, but the inclusion of volume recombination into these simulations increases the pressure loss by factors of 5 [145]. Experimentally, it has been shown in C-Mod that significant fractions of the particle flux to the targets can recombine in detached divertors [146] and recombination cannot be neglected in numerical simulations.
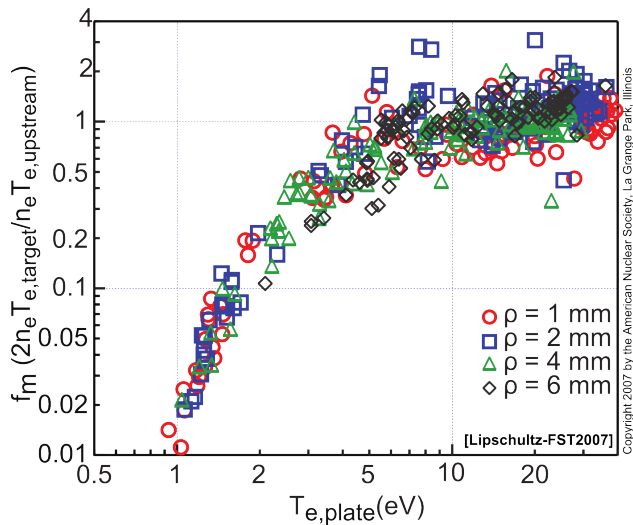

Figure 2.8: Momentum loss factor f_{mom} from experiment and derived from ADAS data [126].

If volume recombination is included it has to be noted that the mean free time of a particle before experiencing a recombination event, $\tau_{\mathrm{rec}} \approx (n_{\mathrm{e}} \langle \sigma v \rangle_{\mathrm{rec}})^{-1}$, needs to be comparable to or smaller than the parallel transit time, $\tau_{\parallel} \approx L_{\mathrm{c}}/u$, where $u \approx c_{\mathrm{s}}$ is the plasma flow velocity. Recombination can contribute significantly only if $\tau_{\mathrm{rec}} \ll \tau_{\parallel}$, which is the case either for long L_{c}, low T_{e}) or subsonic flow.

Geometry & Stability

Going from the simplified picture of the TPM to a real tokamak SOL and taking into account the toroidal symmetry, the actual divertor plasma is determined by at least a two-dimensional evolution of the plasma parameters. The divertor geometry in the poloidal cross section has a major impact on several key divertor parameters. The radiation efficiency [147], the compression and often also the retention is increased for closed divertors with vertical targets [126, 147–153][1]. In general along with increased radiation the target temperatures around the separatrix are lower and partial detachment is achieved more easily, i.e. at lower upstream densities in density ramps experiments [147,153,155]. Complete detachment occurs at similar densities [126,147]. With increased neutral pressures in closed divertors the pumping is better and particle control is easier [156].

Similarly, the magnetic geometry also has an impact. The flux expansion, f_{x}, at the target directly reduces the target fluxes [131, 157] as in (1.3). An improved accuracy of the poloidal field null at the X-point can increase the connection length and the flux expansion at the X-point considerably. Next to the direct effect of the connection length

---

1 Recent result suggests that in JET such a change from horizontal to vertical target is not present [154].

in (2.10) new considerations for an improved divertor concept show that a larger area with small poloidal field strength (low β_p) can lead to an increased radial transport in the vicinity of the X-point [132]. The snowflake divertor with a second order poloidal null and four divertor legs is a direct consequence of this consideration [158, 159]. Optimization for larger flux expansion combined with a larger major radius R at the outer target plate leads to the Super-X divertor [160–162].

The structure of the magnetic field in the divertor and the parallel distribution of parameters like flux expansion and major radius also influence the stability of the ionization and the radiation front [119, 143, 163, 164]. Non-linear effects, e.g. in the radiation cooling process such as radiation condensation instabilities (MARFE), can further the impact of a geometry change by tipping over the divertor parameters into an unstable regime with a subsequent evolution to a new steady-state solution far away from the initial state at only slightly different control parameters [119].

Asymmetries

Another important ingredient in divertor detachment that cannot be discussed here at length are the asymmetries in the power and particle fluxes to the inner and outer divertor. These are still under investigation and not yet fully understood. As introduced in section 5.2.6 the drifts and SOL currents as well as geometric considerations contribute to the asymmetries, but are not sufficient to explain the experimentally observed divertor conditions with numerical codes. A detailed analysis cannot be done here as the detailed study of asymmetries and drifts requires a comparison of forward and reversed magnetic field operation. This is not part of this thesis' experiments and the reader is refered to [89, 113, 131, 165–168]

One particularity of the inner divertor, that will be analyzed in this thesis, occurs with a detached inner divertor and an attached outer divertor at AUG and JET. A high density region in the inner divertor has been observed along with radiative fluctuations close to the X-point [103, 108]. The high field side high density region, HFSHD, is a particular feature that drifts seem to be involved in. However, a full description of this state seems to involve additional physics as well [169].

2.4 Modeling Detachment in the SOL – SOLPS

Modeling of the SOL and divertor with the aim to understand detachment is a long standing scientific task that is not solved in a quantitative sense. Initial analysis of the SOL in a 0D approach like the TPM were improved to 1D simulations of single flux tube SOL by integration of the TPM equations. Two flux tube SOL simulations divide the SOL in the detached near SOL and an attached far SOL including perpendicular transport [170]. Interpretative flux tube modeling of the SOL restricted by experimental data was developed for the Onion-Skin Method solvers [48, 107, 171]. These can be used to map out a 2D plasma solution from experimental measurements at given poloidal locations and to deduce the cross field transport coefficients [48]. Further development led to 2D transport codes with a fluid code for the ion species and a Monte-Carlo solver for kinetic neutrals, e.g. SOLPS [89] or EDGE2D [172, 173]. Computationally intense

kinetic codes [174, 175] can analyze the impact of kinetic effects in the SOL and validate corrections for fluid modeling, e.g. flux limiters. Trace impurity codes like DIVIMP [118, 176] or Impgyro [177] are available to study the impurity transport on given plasma solutions, usually obtained by one of the fluid codes above.

Further refinement of the plasma modeling include 3D effects, e.g. limiters in the main chamber, [178, 179] and a full, first principles description of the radial transport that replaces the ad hoc assumption of anomalous cross field transport coefficient profiles in the convective-diffusive ansatz (5.9) of 2D modeling, e.g. TOKAM3X [180].

In this thesis the SOLPS code is used to model the experimental plasmas and investigate the H-mode detachment physics. It hence contributes to the validation of the SOLPS code in detached and high recycling H-mode conditions by a detailed comparison of experimental data and simulation results.

2.5 State of research

The previous work related to the experimental and numerical work of this this thesis is presented in a condensed overview in this section. This section is supposed to be a first guide to the larger topic of power exhaust in tokamaks for the interested reader and goes beyond the scope absolutely necessary for this thesis.

Operation at high values of radiated power fractions, $f_{\rm rad}$, including detached targets in H- and L-mode has been studied in a number of tokamaks [52, 135, 181–183]. Experimental work on impurity seeding has also been done on a number of machines [53, 121, 134, 135, 155, 181–184].

Detached H-mode plasmas have been demonstrated in JT-60U [168, 185], JET with a full carbon wall [124, 186–188], in JET with the ITER-like wall [129, 189], in C-Mod [126] in DIII-D [190, 191] and in AUG with a carbon wall [123, 155, 192].

In JET the comparison of carbon and ITER-like (W+Be) wall configuration showed that completely detached L- and H-mode operation is achieved at higher density that is connected to lower radiated power in the ITER-like wall environment [129, 193–195]. Extensive detachment studies have been done on C-Mod [126]. The role of neutrals and radiation trapping [171, 196], divertor geometry [126, 197], radiative divertors [120, 182], the role of recombination [198] and localized radiation in the confined plasma, i.e. MARFEs, [131, 168, 198, 199] have been studied. In the DIII-D tokamak the density and temperature redistribution [200] in radiative divertors [190, 191, 201] and the impact of divertor geometry on the divertor plasma [153] were investigated. A unique and very interesting feature of the DIII-D studies is the existence of measurements in divertor volume for the electron density and temperature from Thomson scattering [202, 203]. These measurements allow for a better understanding of the volumetric processes and their localization in the divertor. For progressive validation of numerical modeling such information is crucial in order to verify that the volumetric processes are correctly captured [204]. In the JT-60U spectroscopic studies of the radiation distribution and flow velocities were done [205, 205–208].

The TCV tokamak with its flexible magnetic coils system had a focus on geometry effects [157] and the impact of molecular dynamics in detached plasmas was investigated [101]. TCV, NSTX and the MAST tokamak also contributed to the investigation of advanced divertor concepts like snowflake or super-X divertors [132, 158, 161, 209–216].

Theoretical work on detachment includes the Two Point Model, TPM, [48], the role of a neutral buffer [163] and various stability considerations of the detachment front [119, 143, 217, 218]. Theoretical analysis of MARFEs and radiation fronts have been carried out at different levels of complexity [119, 219–222].

In modeling, detachment has been investigated in a scaling approach at first [89, 223, 224] and more recently simulations of low power and low density discharges have been validated with experimental data in more detail [184, 225–229]. Effects like collisionality [230], neutral fueling [231], geometry [147, 148] or radiation transport [232] have been analyzed. Advanced divertor geometries, e.g. snowflake [233] or super-X [162], are investigated numerically. Predictive modeling, e.g. for ITER, has been done extensively, e.g. in Refs. [232, 234, 235].

In AUG with a carbon wall the radiative divertor and the completely detached H-mode (CDH) [123, 155, 192] was established using nitrogen and neon seeding. So far most dedicated detachment studies in AUG with a tungsten wall focused on L-Mode density ramps [93, 228, 236] with some H-mode studies for partial detachment [237]. More recently, L-mode detachment experiments in AUG with a tungsten wall revealed radiative fluctuations [108] close to the X-point with a detached inner divertor as well as a high field side,HFS, high density region, HFSHD, [238]. They also led to a new characterization of detachment with three phases [127].

High f_{rad} experiments close to detachment with nitrogen seeding in L-mode were used to study the impact of drifts and impurity seeding in L-mode using validated modeling with the edge code SOLPS [239–241]. The effect of the interaction with neutrals and the atomic data was investigated by comparing detachment in hydrogen and helium plasmas [226]. Radiative plasma scenarios with high f_{rad} have been extended to the maximum achievable heating power levels, maximizing the power exhaust qualifier P_{SOL}/R [96].

CHAPTER 3

ASDEX Upgrade & Diagnostics

This chapter introduces the experimental framework of the ASDEX Upgrade tokamak [242] and diagnostics that have particular relevance for this work. For a general introduction to plasma diagnostics please referred to [243, 244].

3.1 ASDEX Upgrade Tokamak

The Max-Planck Institute for Plasma Physics (IPP) operates the upgraded AxisSymetric Divertor EXperiment or short ASDEX Upgrade. A poloidal cut of the vessel geometry along with one of the employed magnetic configurations and the standard midplane diagnostics is shown in figure 3.2. ASDEX Upgrade is a tokamak with a full-tungsten first wall and high heating power capacities. It contributes to the development of tungsten as a

Quantity	
Major Radius	$1.65\,\mathrm{m}$
Minor Radius	$0.5\,\mathrm{m}$
Plasma Volume	$14\,\mathrm{m}^3$
Plasma Surface	$42\,\mathrm{m}^2$
Elongation	1.6
Triangularity	≤ 0.5
Pulse length	$< 10\,\mathrm{s}$
Plasma current	$0.4\text{–}1.6\,\mathrm{MA}$
Ohmic Heating Power	$\approx 1\,\mathrm{MW}$
NBI Heating Power	$20\,\mathrm{MW}$ @ 60 & $100\,\mathrm{keV}$
ICR Heating Power	$6\,\mathrm{MW}$ @ $30\text{–}40\,\mathrm{MHz}$
ECR Heating Power	$4\,\mathrm{MW}$ @ 105 & $140\,\mathrm{GHz}$

Table 3.1: Parameters for ASDEX Upgrade at IPP [242].

first-wall material and to the preparation, exploration and optimization of power exhaust scenarios in future fusion devices. The operational parameters of AUG are given in table 3.1. AUG is a key device in researching and extrapolating tokamak physics in general and power exhaust in particular to the next-step devices ITER and DEMO. AUG is equipped with a large set of diagnostics for the investigation of edge, SOL and divertor physics.

3.2 Heating & Fueling

For the study of power exhaust, the applied heating power and the externally injected neutral gas are important ingredients for experimental studies and modeling.

3.2.1 Heating Systems

The heating system of AUG consists of the intrinsic ohmic heating, neutral beam injection, NBI, electron cyclotron heating, ECRH, and ion cyclotron heating, ICRH [245].

The neutral beam heating system has eight sources with a power of 2.5 MW @ 95 kV each. The sources are assembled in two beam boxes which are 180° toroidally apart. Each box has two dominantly radial and two dominantly co-current directed sources, see figure 3.1.a. Beam box 2 has two on-axis and two off-axis beams, see figure 3.1.b. The acceleration voltage of the neutral beam can be reduced from 95 kV to 60 kV and H/D or He can be used as injected particles.

ECRH couples to the gyro motion of the electrons by microwaves at a frequency of 140 GHz or 105 GHz. In total eight gyrotrons are available each with an approximate power of 500 kW. The microwave frequency determines the absorption location, where the electron cyclotron frequency, $\omega_{c,e}$, is resonant. ECRH suffers from a critical cut-off density above which no power can be coupled to the plasma. Using ECRH at densities above the cut-off density is a risk for in-vessel components. Reflected microwaves can deposit significant power in quite localized areas.

Four ICRH antennas are available with a total of up to 6 MW of heating power at a
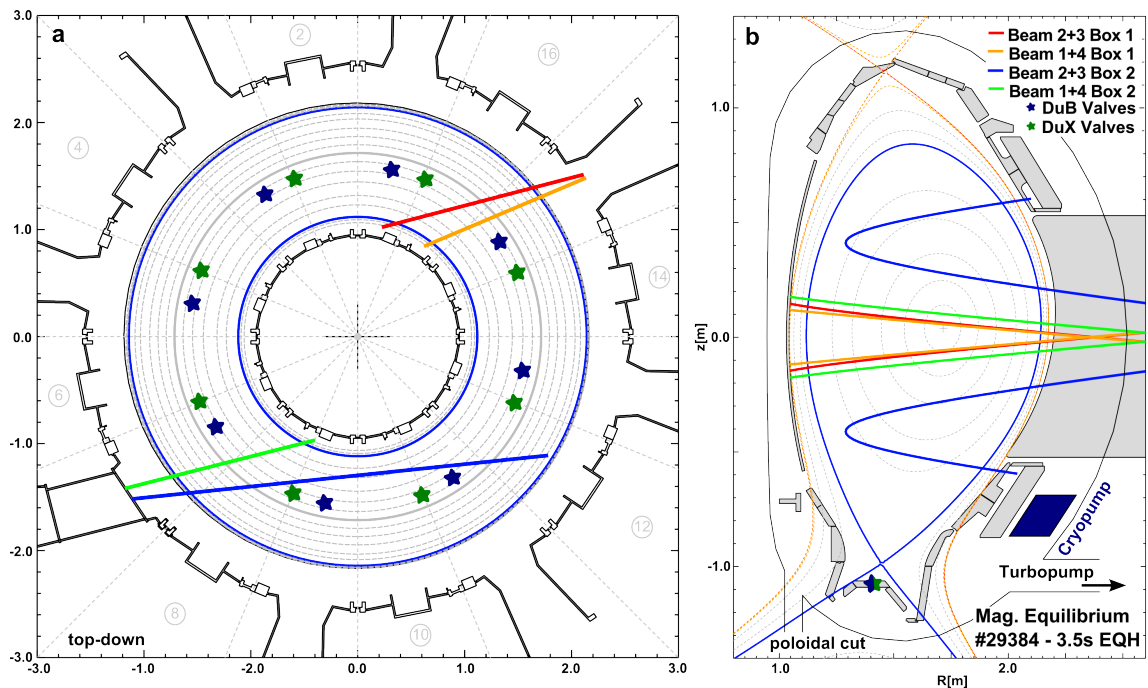

Figure 3.1: Neutral beam geometry an locations of the gas fueling valves at AUG.

wave frequency in the resonant range for $\omega_{c,i} = 30$–40 MHz. In AUG the application of ICRH is coupled to an increased tungsten influx from the ICRH antenna casing [246].

3.2.2 Gas Inlet System

The gas inlet system for neutral deuterium and seed impurities is shown in figure 3.1 as green (DuX valves) and blue (DuB valves) stars respectively. DuX valves puff through a gap in between two sectors and DuB valves puff through dedicated cutouts of divertor baffle tiles in the middle of a sector. The alignment of the valve outlets with the cutouts or the sector gaps is not rechecked after every opening. A misalignment would lead to directed neutral flows in the subdivertor volume that might influence ionization gauge measurements locally.

3.2.3 Pumping System

The pumping system at AUG is shown in figure 3.1.b and has two components: First, turbomolecular pumps with a total pumping speed of $S = 13$ m^{-3}s^{-1} [245]. Second, a toroidally symmetric cryopump below the outer divertor target in the so-called pump chamber. The cryopump is a combination of a liquid nitrogen and a liquid helium pannel and has a pumping speed of $S = 100$ m^{-3}s^{-1} [247, 248]. The pumped flux, $\Gamma_{\text{pump}} = n_0 S$, can be derived from the neutral density, n_0, in the pump chamber. From the conductance of the subdivertor towards the pump chamber, $f_{\text{cond}} \approx 1/5$, and the typical volume of the divertor, $V_{\text{div}} = 2$ m^3, a typical pumping time of $\tau_{\text{pump}} = \frac{V_{\text{div}}}{f_{\text{cond}} S} \approx 90$ ms can be derived.

3.3 Relevant Diagnostics

ASDEX Upgrade is equipped with a large number of plasma diagnostics. A selection of diagnostics that are of a particular relevance for the pedestal, SOL and divertor and this thesis is presented. The implications of the diagnostics limits and data evaluation for the analysis presented will be discussed in chapter 4 and chapter 5.

3.3.1 Magnetic Equilibrium Reconstruction

Poloidally distributed Mirnov coils, see figure 3.2, measure the radial and poloidal magnetic flux, which is used as a boundary condition in the code CLISTE to reconstruct the magnetic equilibrium by solving the Grad-Shafranov equation [65, 249, 250]. Radial density and temperature profiles can be included as additional constraints. For toroidally symmetric CLISTE equilibria an uncertainty of $\Delta R_{\text{sep}} \approx 5$ mm is expected for the radial position of the separatrix at the midplane [251]. Analysis of the two-point model for standard AUG plasma conditions predicts a robust upstream separatrix temperature of $T_{e,u} \approx 100$ eV. The midplane temperature profiles can be used to constrain the radial
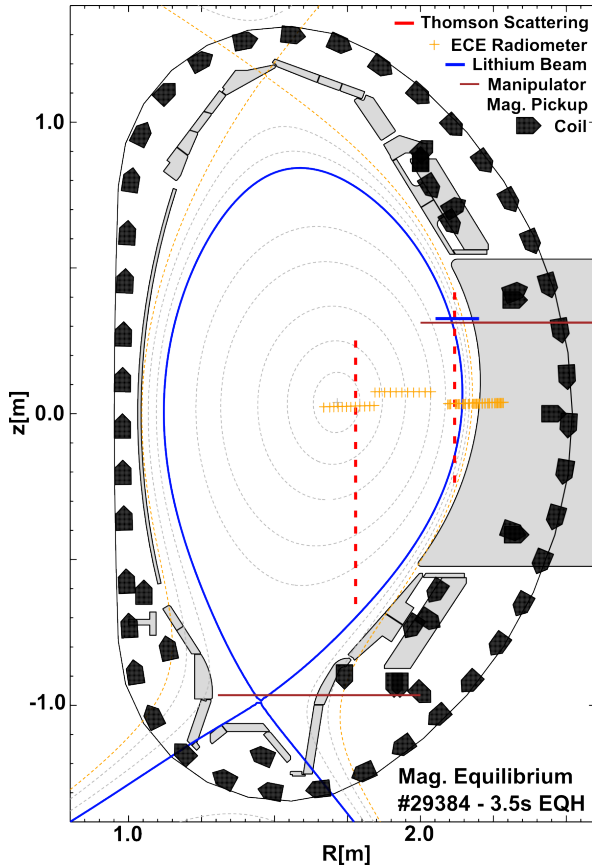
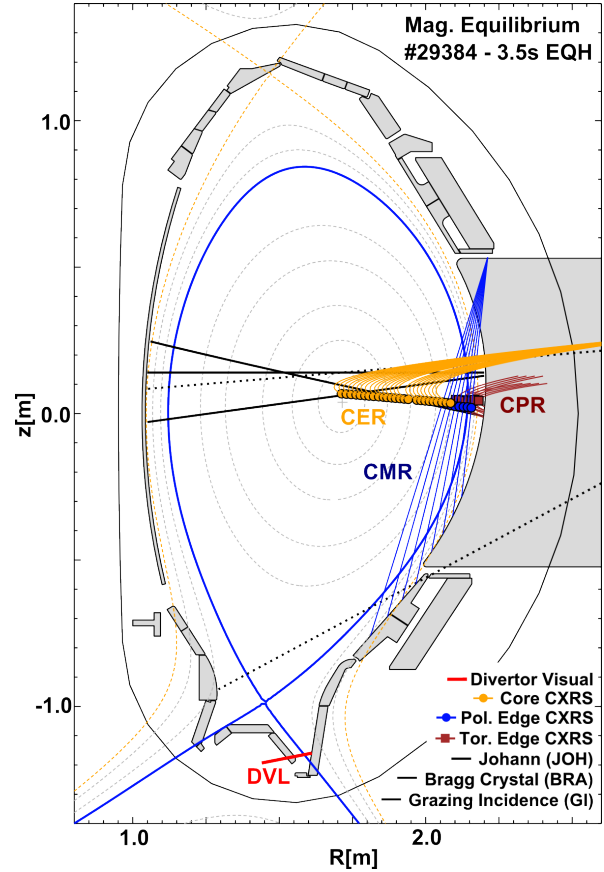**Figure 3.2:** AUG midplane diagnostics and magnetic pickup coils.

Figure 3.3: AUG CXRS and spectroscopic tungsten diagnostics.

shift of the diagnostics with respect to the separatrix. The accuracy of the strikepoint position is about $\Delta S \approx 1$–1.5 cm. The X-point position is subject to larger uncertainty. In attached conditions, the ion saturation current and the heat flux profile at the target should peak at or close to the separatrix and the Eich-Fit can be used [252] to determine the shift, ΔS, of the target profiles along the target coordinate, S.

The uncertainty in the separatrix position with respect to the radial midplane profiles creates a major uncertainty in the determination of the upstream plasma parameters, which are used as boundary conditions in the two-point model analysis of the SOL and divertor. Together with a narrow radial power decay length of $\lambda_q \approx 1$ mm a radial shift of the upstream profiles of 5 mm substantially modifies the power balance of the near SOL. Similarly, correct strikepoint and X-point positions are crucial. The spatial uncertainty of the X-point determines if MARFE-like radiation events occur inside or outside of the separatrix. A change in the strikepoint position strongly changes the magnitude of the parallel pressure loss in partially detached conditions. Hence, an accurate mapping from midplane to target is very important to be able to compare midplane and target profiles.

3.3.2 Thomson Scattering

The Thomson scattering diagnostic [253–255] uses Nd:YAG lasers to measure radial electron density and temperature profiles. The laser light is scattered by the electrons and measured with filtered avalanche photodiodes. The electron density is derived from the intensity of the scattered signal and the electron temperature from Doppler broadening measured by intensity ratios at different wavelengths. In standard operation, the repetition rate of the edge and core systems are 120 and 80 Hz respectively. In figure 3.2 the geometry of the Thomson system is shown. The vertical spacing of the channels along the laser paths for both systems is 60 mm. For high resolution profiles mapped to the midplane the edge-optimized magnetic configuration with the separatrix position at $R_\mathrm{sep} = 2.145$ m should be used. In this configuration an optimal coverage of the pedestal and the near SOL with the edge system is achieved. A radial sweep of the separatrix position with a unidirectional duration of usually 250 ms enhances the profile information. It has to be noted that edge and core systems measure the plasma parameters for the same ϱ_pol at different poloidal locations. The proximity of some channels of the core system to the X-point will lead to larger spatial uncertainties in the position with respect to the magnetic equilibrium.

Since Thomson scattering simultaneously measures the electron density and temperature in the same location, the profiles are inherently aligned and allow the relative radial alignment of profiles from different diagnostics that are mapped to the midplane, e.g. the lithium beam and the ECE radiometer. Typically, the edge Thomson system is shifted 6 mm radially inwards to meet $T_\mathrm{e,u} = 100$ eV. The outermost channels of the core system are shifted by 30–50 mm for consistency of the edge and core profiles.

The statistical and systematic errors of the edge Thomson system is 10 % and 7 % for the electron density and about 7 % and 7 % for the electron temperature, respectively. Examination of the Thomson data shows larger scatter in the edge system measurements. The expected intensity of the scattered light is lower in the SOL due to lower densities. High fluctuation amplitudes due to smaller signal to noise ratio and SOL turbulence are to be expected for the edge system [256].

3.3.3 Lithium-Beam Diagnostic

The lithium beam diagnostic [257–259] uses a beam of accelerated neutral lithium atoms ($E_\mathrm{kin} = 60$ keV) along the chord shown in figure 3.2. Collisions with plasma particles excite the neutral lithium atoms to higher electronic states which decay radiatively. Filtered photomultipliers with a time resolution of 50 μs detect line emission along the lithium beam with a spacing of 3.6–5.5 mm (old system) or 6–7 mm (new system) and a spot size of 5 mm. The lithium beam is chopped with a frequency of up to 2 kHz for background subtraction.

A radial emission profile is reconstructed and a forward model of the excitation by beam-plasma interaction is used to determine the electron density. Beam attenuation and error propagation in the forward model limit the validity range of the diagnostic to $\varrho_\mathrm{pol} > 0.95$ for the old optics and $\varrho_\mathrm{pol} > 0.9$ for the new optics. So far, only the old optics are fully

validated and therefore data in this thesis is restricted to this system. The new optics is used additionally where the pedestal top region is crucial, e.g. in section 4.5.2. A radial shift of typically 5–7 mm of the lithium beam profile is determined through alignment with the Thomson profiles.

3.3.4 Electron Cyclotron Emission Radiometer

The electron cyclotron emission, ECE, is measured by radiometers at a sampling rate of 2 MHz to determine the electron temperature [260]. The harmonics of the electron cyclotron frequency, $\omega_{c,e}^l = leB/m_e$ (cold resonance) are radially located through the magnetic field. Standard ECE temperature evaluation assumes optically thick plasma, where the intensity from ECE can be identified with the electron temperature. In most experiments the assumption of optically thick plasmas is only valid up to the pedestal top [243, 260]. In optically thin plasmas shine through occurs and high radiation temperatures of up to several 100 eV are measured in the SOL. The ECE temperature profiles in the SOL are not reliable without forward modeling of the radiation transport in optically thin plasma [260]. As ECRH the ECE diagnostic is limited to densities below the cut-off.

3.3.5 Charge-Exchange Recombination Spectroscopy

The charge-exchange diagnostic measures light emission of hydrogen-like impurity ions [261, 262]. These ions are produced by charge exchange of fully stripped impurity ions with fast neutrals of the neutral beam injection heating and thermal neutrals. From the impurity line radiation the impurity ion temperature is derived from the Doppler width, the impurity velocity from the Doppler shift and the impurity density from the intensity using a given neutral deuterium density. An accurate wavelength calibration and accounting for passive emission is necessary. Generally the assumption of thermalized ions is thought to be valid and the ion temperature is identified with the temperature deduced from the charge exchange measurements. The standard charge exchange systems observe beam 3 from the beam box 1. Usage of the other

Figure 3.4: Ion temperature mismatch of poloidal and toroidal CXRS systems for nitrogen.

beams of beam box 1 interferes with the diagnostic evaluation and needs to be taken into account. Depending on the impurity level and the seeding scheme, impurity lines of born, nitrogen, carbon and helium are regularly used for CXRS measurements at AUG. Two main charge exchange systems are available: An edge system with two spectrometers that examine the pedestal and edge transport barrier region with high spatial resolution. The line of sight direction of the spectrometers is toroidal (CMR) and poloidal (CPR) to be able to determine poloidal and toroidal velocities at the same time. The core system (CER) lines of sight are oriented in the toroidal direction, see figure 3.3. The core
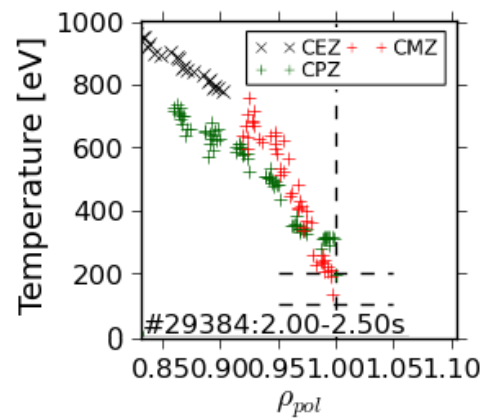
system has a spot size of 2.5 cm and an integration time of 5–10 ms. The spot size of the edge systems is 0.5 cm, the line of sight spacing is 1–1.4 cm and the integration time is typically 2.3 ms. The radial shifts that are applied for alignment are 0.5–1.5 cm for the edge systems and 1–2.5 cm for the core systems.

Ion temperature profiles from the edge and core charge exchange systems are generally in good agreement. A particularity of using nitrogen lines is that the poloidal edge system measures ion temperatures of up to 300 eV lower than the other systems at the same radial location, see figure 3.4. This discrepancy might be due to a stronger impact of passive line emission on the poloidal system. Its lines of sight end in the far SOL of the outer divertor, where strong nitrogen radiation can be expected. Unfortunately, fitting the line width with an additional, cold divertor component did not alleviate this problem.

The CHICA code reconstructs the impurity density profile from the impurity line emission profile assuming poloidal symmetry and using experimental profiles for T_e, T_i, n_e and the rotation velocity, v_{rot}. The necessary neutral density profile is either specified from experiment by beam emission spectroscopy or calculated with the Monte-Carlo code FIDASIM [263]. The FIDASIM code calculates the neutral attenuation for all selected beams. FIDASIM does not take into account the toroidal separation of beam boxes 1 and 2. The inclusion of beams from box 2 into calculations leads to overestimation of the neutral density, n_0, and will reduce the evaluated impurity density by up to a factor of 10 as the line emission is $\propto n_0 n_{imp}$. During the work on this thesis, it has been found that the neutral density profile modeled by FIDASIM is very sensitive to the initial guess of the impurity concentration. Figure 3.5 shows the evaluated boron density for different initial guesses of the carbon and nitrogen concentration. The higher inital Z_{eff} leads to a reduction in the local neutral density from FIDASIM and hence to a higher impurity content. A separate evaluation of the impurity density in seeded and non-seeded phases of a discharge as well as an iterative approach can become necessary.
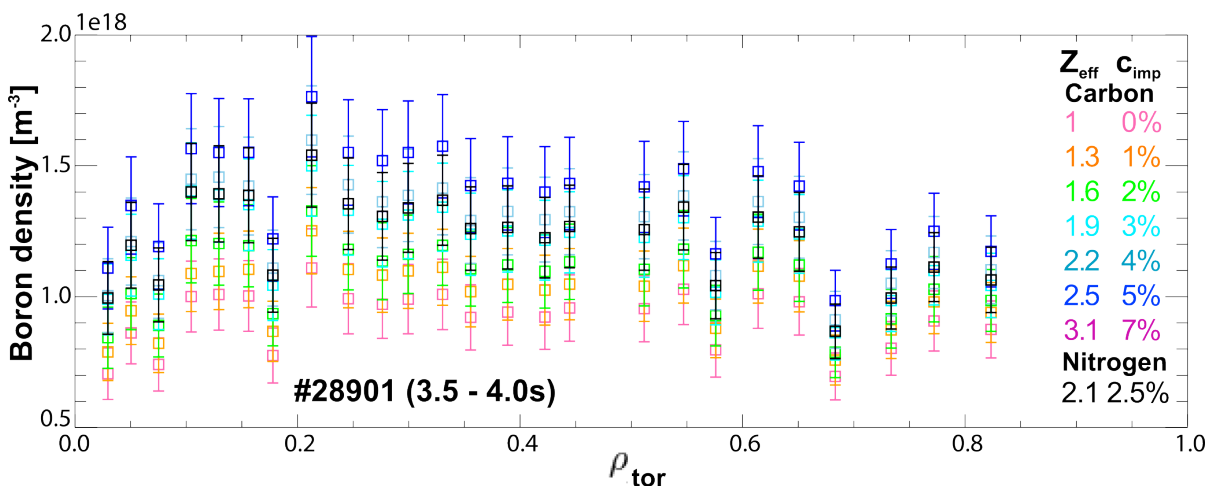

Figure 3.5: Nitrogen impurity density from CHICA with different initial impurity concentration guesses.

3.3.6 Bolometry

Bolometry is used to measure the electromagnetic radiation losses, p_{rad}, from the plasma. Bolometers measure the energy that is deposited into a defined volume from along a line of sight. The lines of sight are defined by an aperture in the bolometer cameras. The bolometry at AUG has two types of detectors [103, 264]: First, fast diode bolometer cameras with an acquisition rate of 200 kHz, that are not absolutely calibrated and have a strong variation in spectral sensitivity [264]. Second, foil bolometers [265–267], that are absolutely calibrated and have a time resolution of about 2 kHz. The coverage of the main chamber volume and the divertor with lines of sight is shown figure 3.6[1]. The line integrated nature of the bolometer measurements requires a tomographic reconstruction or Abel-inversion [268] to retrieve the 2D spatial radiation distribution. The line of sight spacing in the divertor volume is too large for accurate radiation pattern reconstruction with large gradients within the divertor. For foil bolometers, ill resolved, high frequency ELMs, a limited spatial resolution at the X-point and strong poloidal asymmetries in the divertor radiation distribution interfere with the afore-mentioned analysis tools as both rely heavily on symmetry assumptions. In the presence of ELMs the tomographic reconstruction often seems to produce a convolved ELM/inter-ELM radiation distribu-
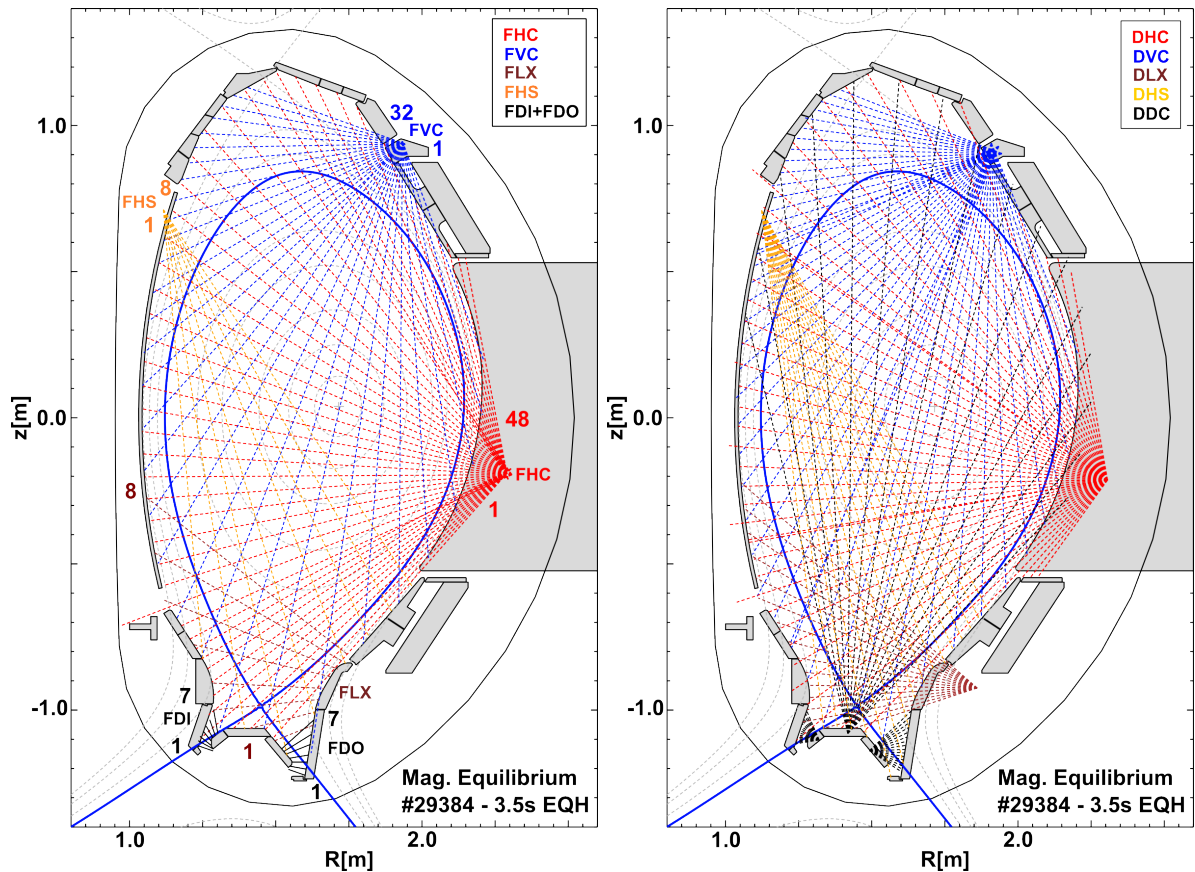

Figure 3.6: Foil (left) and AXUV (right) bolometers.

---

1 The horizontal divertor camera (FLX) as well as the HFS camera (FHS) are not calibrated.

tion. Possible reflections at the metal surfaces in full tungsten clad AUG are not taken into account in the analysis, although they have been shown to be crucial for analysis of line integrated measurements [269]. At low power levels, e.g. during detachment, the power deposition of neutrals on the bolometers might be important [126].

A cross check of the reconstruction quality is the validity of a simple power balance with $P_\mathrm{H} \approx P_\mathrm{tar} + P_\mathrm{rad}$, where P_tar is the power to the targets measured by infrared camera and P_H is the heating power. This power balance implicitly neglects power losses to the main chamber wall. In nitrogen seeded phases of the experiments discussed here, strongly localized radiation sources are present in the divertor. The tomographic reconstruction fulfills the power balance to a 10 % accuracy in these cases. A comparison of tomographic reconstruction and Abel-inversion in the main chamber results in comparable radial profiles of local emissivity. An adaptation of the tomographic reconstruction that allows for larger gradients of the radiated power density in the X-point region was implemented as a result of this analysis. It improves the divertor solution of the radiated power density, p_rad. In AUG divertor radiation, $P_\mathrm{rad,div}$, is defined as all radiation below the upper edge of the inner divertor target plate ($z < 68$ cm). The remaining radiation is main chamber radiation, $P_\mathrm{rad,main}$, which is sometimes also misleadingly referred to as core radiation.

A fast analysis of P_rad from foil bolometers based on geometrical assumptions exists at AUG. This calculation has proven not to be accurate [103] and needs a rescaling factor. The fast P_rad in nitrogen seeded phases is consistently about a factor 1.5 lower than P_rad from tomography. The recalibration factor is different for non-seeded phases.

The fast AXUV-diode bolometers provide insight into fast processes that reflect in the radiation, e.g. radiative fluctuations at the HFS close to the X-point [108]. The analysis of the spatial and temporal evolution of ELM filaments and other fast events is feasible without an absolute calibration. AXUV signals are used for ELM synchronization and/or removal in this thesis.

3.3.7 Divertor Spectroscopy

The visible divertor spectroscopy at AUG [102, 270] consists of two spectrometers with a frame transfer CCD cameras with an integration time of 2.45 ms. Two gratings allow measuring approximately 15 nm (2400 lines/mm) or 150 nm (300 lines/mm) of spectral range in the visible range (395–720 nm) with a dynamic range of 16 bit. The spectrometers are absolutely calibrated and have 25 channels each. The available lines of sight in the divertor and main chamber are shown in figure 3.7.

The standard spectral range from 396 nm to 411 nm includes the Balmer $D_{\varepsilon,\delta}$ lines (390,410 nm), an NII-singlet (399.6 nm) and an NIII-doublet (409.733/410.339 nm) line. The electron density can be determined from the width of the Balmer lines by Stark broadening analysis [1, 102].

For the analysis of line radiation intensities a collisional radiative model is required. This model is a system of rate equations that describe the charge state distribution and the population densities of excited states for an ensemble of plasma particles at particular

plasma parameters (n_e, T_e, etc.). A collisional-radiative model that is widely used in fusion research is described in Ref. [90, 137]. Under certain conditions, mostly valid in low density plasmas, the collisional-radiative model reduces to a corona model that depends only on T_e [271]. From such models effective reaction rates, such as photon emission coefficients or cooling factors, can be derived. Photon emission coefficients give the rate of photon emission for specific transitions at given plasma parameters. These coefficients have been tabulated in the ADAS database [137] for a number of elements and can be used for spectroscopic diagnostics of plasmas [108, 141, 272–276]. Standard temperature measurements using deuterium line ratios are restricted to very low temperatures (<2–5 eV) [277].

In this thesis it has been attempted to extract electron temperatures from line ratios. This was not successful since the interpretation of line integrated measurements of emission by multiple ionization states in the divertor region are not readily interpreted. Large gradients in the divertor plasma parameters and the fact that different transitions, from different ionization states or ions, usually radiate efficiently at different plasma parameters (T_e) largely prevent a simple analysis of the line integrated intensity ratios. A simple comparison of the line intensity ratio with photon emission coefficient ratios is only valid provided a localization of the radiation ensures that all considered line emission stems exclusively from the same plasma region. In principle, it is possible to reconstruct line intensity ratios with plasma parameter profiles along the lines of sight. However, with a divertor transition from attached to detached targets and very different divertor conditions in the inner and outer divertor there are no fixed spatial symmetries of the plasma profiles, that could be exploited for a profile parameterization along the line of sight.

Figure 3.7: Most relevant diagnostics for divertor detachment studies at AUG including ionization gauges, baratrons, interferometer chords (H1, H5, V2), target Langmuir probes and spectroscopy lines of sight.

However, the appearance of line radiation of specific ions can be used as an indicator for regions with certain T_e [278] according to their fractional abundance in a coronal approximation as shown in figure 3.8. In coronal equilibrium, the mentioned NII- and NIII-lines correspond to T_e of about 1–5 eV and 5–10 eV respectively. The Balmer lines have a maximum total emission coefficient at about 1.5 eV, where also the transition from an ionizing plasma into a recombining plasma is expected [270]. The determined temperatures as such are subject to large
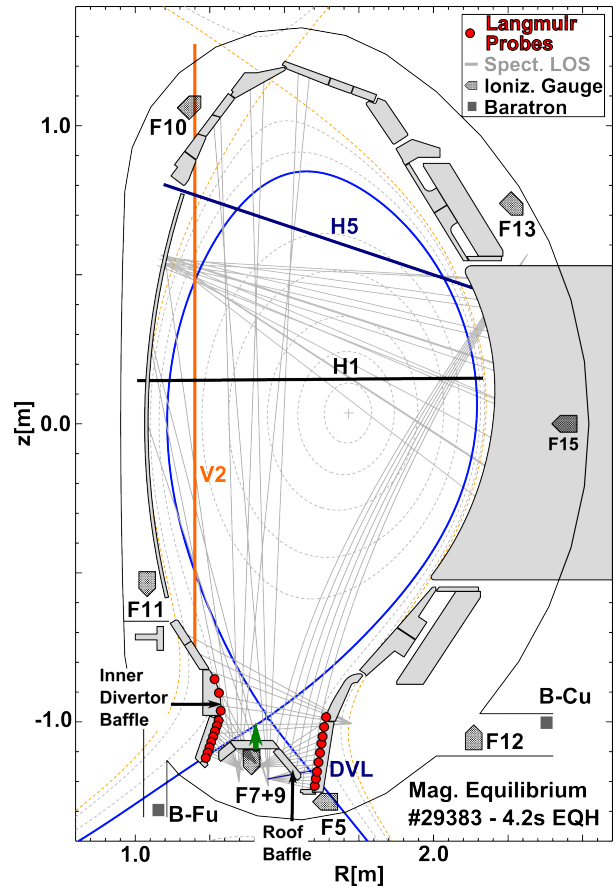
uncertainties as strictly speaking non-coronal effects and transport in the SOL need to be taken into account. In the absence of more accurate measurements, e.g. from a divertor Thomson system [202], these estimates provide valuable information about the temperature distribution and its evolution in the divertor as well as the extent of ionization $T_e > 10$ eV and charge exchange $T_e < 5$ eV regions for deuterium.

Even without the ability of direct interpretation of spectroscopic intensity measurements such measurements can restrict 2D modeling of plasmas efficiently. Depending on the ion (species, charge, etc.) different aspect of the divertor physics can be constrained in the modeling: Low charge states will validate the recycling model and neutral fluxes. Higher charge states are less dominated by the impurity sources and can be used to validate the transport model for impurities and the temperature and density distribution.
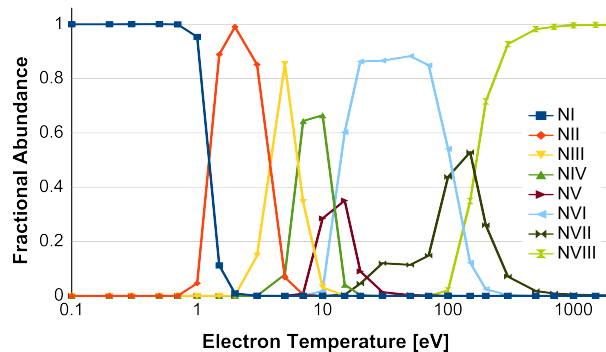

Figure 3.8: Fractional abundance of nitrogen ionization stages for coronal equilibrium calculated with ADAS at $n_e = 10^{19}$ m^{-3}.

Most visible nitrogen lines are from neutral to doubly ionized nitrogen particles (NI-NIII). The main contribution to the radiated power is expected from the NIV with its Li-like electron configuration [276]. Its dominant lines are in the VUV spectral range and are not accessible for our visible divertor spectroscopy. Nonetheless, to explore higher ionization states our recent experiments included measurements of an NV line at 461.9 nm in the SOL and in the divertor. Especially with regard to the observed X-point radiation during detachment this might prove valuable in future studies as the probed temperature range extends to larger temperatures. Our experiments triggered the evaluation of the diagnostic capabilities of this NV line for the pedestal, e.g. charge exchange, at AUG, JET and C-mod.

In order to estimate the neutral influx from the targets, i.e. the recycling flux, the S/XB method can be applied under certain conditions [279]. The neutral influx is given by $\Gamma_H \approx \frac{S}{X_i B_{ik}} \Gamma_{\gamma, i \to k} = \frac{S}{PEC_{ik}^{exc}} \Gamma_{\gamma, i \to k}$, where S is the ionization rate, X_i is the excitation rate into the excited state i, $B_{ik} = A_{ik} / \sum_{i<j} A_{ij}$ is the branching ratio, that is derived from Einstein coefficients A_{ik}, and PEC_{ik} is the photon emission coefficient of the transitions $i \to k$. The coefficient S/XB is often assumed to be constant in a limited parameter space. For some transitions of particular interest experimental data on the dependences of S/XB exist, e.g. WI (400.9 nm) [280]. The influx measurements were developed in [281] and have been applied across a number of impurities and deuterium [75, 108, 279, 282–284].

In H-mode it has to be noted that spectroscopy is prone to misinterpretation due to ELMs. With a minimum integration time of 2.45 ms for standard settings, the spectroscopy integrates over inter-ELM and ELM periods for ELM frequencies above 400 Hz. Depending on the line of sight, the transition looked at and the plasma parameters either ELM or inter-ELM conditions can dominate the measurement. For derived Stark density profiles along the targets it is observed that these are an upper envelope to strongly

fluctuating Langmuir probe density measurements at the target.

3.3.8 Fast Ionization Gauges & Baratrons

Neutral pressure measurements at AUG are predominantly done by ionization gauges. Neutrals entering the gauges via an entrance slit are ionized by electron impact and the induced ion current is measured [285–288]. The setup measures flux densities rather than neutral density or pressure. Based on the assumption of isotropic thermal fluxes the conversion of the flux density into a neutral pressure is $p_0 = 0.5 n_0 T_0 = 2 \frac{\Gamma_0 T_0}{v_{\mathrm{av}}} \approx 1.6 \times 10^{23} \Gamma_0$, where $v_{\mathrm{av}} = 1240$ ms^{-1} is the average absolute velocity [43, p.200] of D_2 at room temperature. A prefactor of 0.5 arises, because the neutral flux is measured as atomic flux, whereas the neutral pressure is dominated by D_2. The neutral density evaluation is based on a calibration, yielding a sensitivity factor for deuterium, s_{H}. A gas mixture or other working gases need a conversion factor [286]. For pure nitrogen (N_2) this is $s_{\mathrm{H}}/s_{\mathrm{N}} = 2.4$ [289]. In the course of this thesis we attempted to separate the partial neutral pressure of D_2 and N_2 in our discharges with strong nitrogen seeding with a spectroscopic gauge (F12). Concentrations of N_2 of about 25 % in the pump chamber were derived. However, the signal to noise ratio of such measurements is large and the variation of the concentration withing the errorbars was 9–47 %.

Saturation of the ionization gauges is attained at roughly 15 Pa D_2 neutral pressure at a magnetic field of 6 T. At lower magnetic field the saturation tends to be shifted to higher pressures. The calibration of the gauges in AUG is taken for neutral pressures in the torus of up to 5 Pa. At larger neutral pressures an extrapolation of the calibration is applied.

Starting with the 2014 campaign new baratrons were installed below the inner/outer divertor. A validation of the ionization gauge measurements at high neutral pressures (≥ 1 Pa) was done in the framework of this thesis by a comparison with the baratron measurements. The baratron and ionization gauge measurements are consistent when taking neutral conductances into account. The locations of the neutral pressure measurements in AUG are shown in figure 3.7.

3.3.9 Langmuir Probes & Shunt Current

Langmuir probes are used to measure the plasma parameters in front of material surfaces, especially the divertor target plates. The Langmuir probe analysis is discussed in Ref. [290] in more detail. The fixed, flush-mounted Langmuir probes in the lower divertor are mostly triple probes. Single probe operation or additional single probes are available. Up to nine toroidally separated Langmuir probes are located at one poloidal position.

The triple probes measure floating potential, V_{float}, and ion and electron saturation currents, $i_{\mathrm{sat,i/e}}$. An ion saturation current density, j_{sat}, is derived with an effective probe area, A_{eff}. The effective probe area is larger than the geometrical probe area, A_{geo}, due to the sheath acceleration of ions towards the target [291]. From the probe characteristics the electron density and temperature are obtained [243, 290].

The triple probes are operated with a battery voltage of 72 V, which sets an upper limit for reliable electron temperature measurements of about 25 eV. A lower limit for reliable temperatures from single and triple probes is about 2 eV due to the limited resolution of the diagnostic. The data acquisition rate of standard triple probes is 25 kHz. Fast Langmuir probes with special electric cabling allow for data acquisition rates of approximately 2 MHz including a 700 kHz low pass filter. Single probes are swept with 200–800 Hz in the range ±75–200 V. The spatial resolution at the inner and outer target is about 3.0 and 2.5 cm, respectively. For fully resolved (peaked) target profiles a sweep of the strikepoint ($\Delta t \approx 250$ ms) can be done. However, the change in the divertor geometry affects the plasma and a careful evaluation of the changes induced by the sweep itself is often necessary.

For the interpretation of Langmuir probe data three main issues exist: First, the effective probe area is not precisely known. Second, significant impurity content in the divertor plasma leads to an underestimation of the electron density due to a change in the effective sound speed at the target [292]. Third, small field line angles at the target invalidate Langmuir probe theory, because gyrating ions travel faster to the probe surface than gyro-averaged electrons. The target Langmuir probes are mounted at a slight toroidal angle (0.5 °) into the target plates. Still, field line impact angles at the target have to be larger than 1–1.5 ° [290].

A fast shunt measurement of the current to a divertor tile can be used for ELM synchronization. This measurement is calibrated to a Langmuir probe temperature in the outer divertor and can be used as a controller for the divertor temperature, T_{div} [122]. The T_{div} signal is median filtered over 2 ms to remove ELMs. The temporal resolution of the diagnostic is approximately 1 MHz.

3.3.10 Thermography

The target thermography system at AUG derives the power fluxes from infrared temperature measurements of the target material surface. The temperature evolution is forward-modeled with the 2D heat transport code THEODOR [88] to derive the power fluxes. An infrared line camera with 256 pixels, a dynamic range of 12 bit and maximum data acquisition rate of 7.7 kHz is employed [293]. Depending on the integration time settings and the plasma scenario, the camera can have poor signal to noise ratio. This is especially true for cold target conditions during detachment. Usually, the temperature is sufficiently high for power flux calculations close to the strikepoint. A careful check of the signal to noise ratio is necessary to determine the validity of the derived power fluxes along the target for each experiment. In addition, it is important to keep in mind that the temporal resolution of the camera and the heat transport can convolve inter-ELM and ELM heat loads at higher ELM frequencies. Reflections and volume radiation can be an issue for the data evaluation [293].

CHAPTER 4

Experiment

This chapter presents the experiments that were carried out in AUG during the work on this thesis. Detachment in H-mode has been achieved in AUG with a full tungsten wall for the first time. The detachment evolution and its impact on the main chamber plasma are discussed. A new feature of nitrogen induced H-mode detachment is intense, localized radiation at the X-point inside the confined plasma that is correlated to an upstream pressure loss and the occurrence of complete detachment at the outer target[1].

4.1 Previous Detachment Studies on ASDEX Upgrade

So far most detachment studies in AUG with a full tungsten wall were done in L-Mode. Detachment was achieved by increasing the separatrix density through deuterium gas puffing. The fueling in L-Mode is less restrictive and density ramps can be implemented straightforward by simple deuterium fueling ramps. Detachment occurs at lower density due to lower heating power compared to H-mode experiments [127]. The higher heating power necessary to sustain H-modes [57], requires a higher density for detachment. Previously, when AUG had a carbon wall (prior to 2003) [81] complete H-mode detachment by deuterium gas puffing was possible [192]. For heating powers of $P_H = 5 - 12.5$ MW in AUG with a tungsten wall, even in dedicated density limit experiments with reduced pumping and the maximum possible deuterium fueling rates only a partially detached outer target has been achieved before the H-L backtransition [103]. This is most probably due to the lack of the radiation cooling of the intrinsic carbon impurity. Radiation cooling with nitrogen seeding has been routinely applied in full tungsten AUG to reduce the target heat flux for target protection [92, 97]. In such discharges the nitrogen seeding often leads to partial detachment at the outer target.

The first completely detached H-mode discharges in AUG with tungsten walls were achieved during this thesis with considerably larger nitrogen seeding rates than previously applied. Previous experiments at AUG aiming at a validation of numerical simulations have been done in low density L-mode conditions [184, 225, 228, 294], where the

---

1 Part of this material is published in [104].

complication of transiently enhanced power and particle flows into the SOL by ELMs is not present.

4.2 Experimental Setup

The H-mode discharges in this study are at a plasma current of $I_P = 800$ kA and a toroidal magnetic field of $B_t = 2.5$ T, which sets the safety factor to $q_{95} \approx 5.5$. The discharges are done in forward field configurations, such that the ion ∇B-drift points to the lower divertor. The plasma current is chosen such that no massive gas injection [295, 296] for disruption mitigation is necessary. Therefore, additional unintended impurity content in subsequent discharges is excluded. The confinement quality of a discharge is described by the factor H_{98} that compares the achieved confinement to the prediction of the $H_{98,y2}$ scaling, that has been derived from data from a number of tokamaks [55]. The standard H-mode confinement corresponds to $H_{98} = 1$. In our experiments H_{98} ranges from 0.8–1.05. The heating power was varied from 6.4 to 11.4 MW with constant central ECRH of 1.4 MW. The deuterium fueling, Γ_D, and nitrogen seeding, Γ_N, rates were varied independently in the range of $1 - 3 \times 10^{22}$ e$^-$s^{-1} in order to vary the neutral density in the divertor, $n_{0,\mathrm{div}}$, and the nitrogen concentration of the plasma, c_N. Stable impurity concentrations in our discharges are supported by a nitrogen preloaded wall that minimizes the wall pumping of nitrogen. Preloading was achieved with previous nitrogen
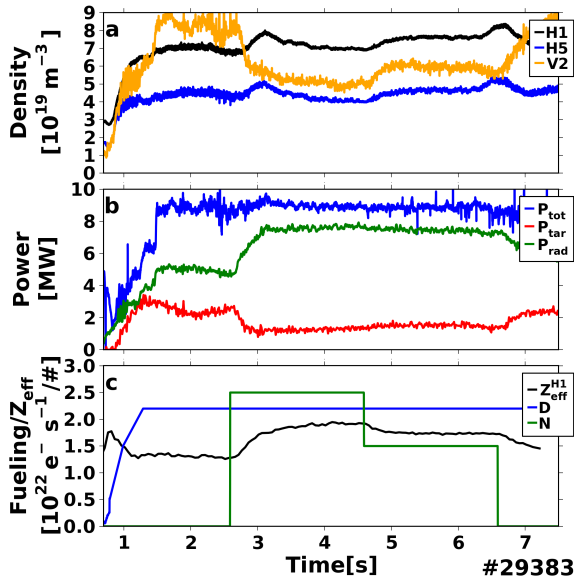
Figure 4.1: H-mode detachment experiment #29383: a) Line integrated density (H1: central, H5: edge, V2: Vertical, high-field side SOL (figure 3.3)). b) Heating Power (PH), radiated power (P_{rad}) and power to the target (P_{tar}). c) Fueling and seeding rates [104].

Figure 4.2: a)+b) I_{sat} is given in black. Inter-ELM median values ,$\langle I_{\mathrm{sat}}\rangle_{\mathrm{ELM}}$, are given in blue and red for the inner and outer target respectively. $I_{\mathrm{sat,TPM}}$ is given in green. c) Standard deviation of the I_{sat} signal as a measure of ELM size. d) Power spectrogram of AXUV-diode measurement at the X-point [104].

seeded discharges [181]. Nitrogen dominates $\overline{Z}_{\mathrm{eff}}$ during the seeding phase, where $\overline{Z}_{\mathrm{eff}}$ is the Z_{eff}-profile line i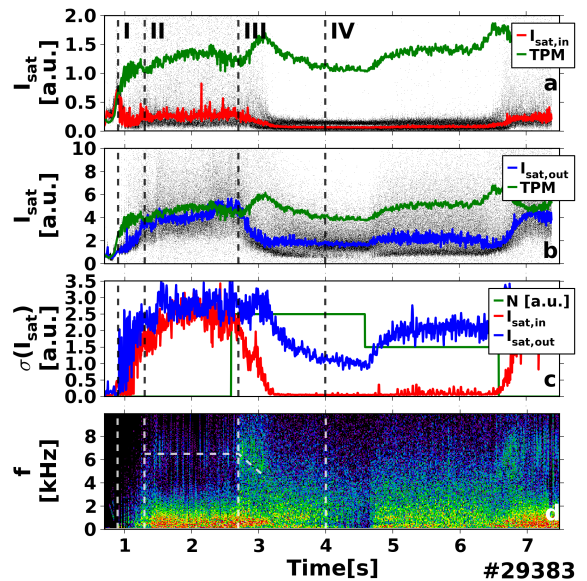ntegrated along the central DCN interferometer chord H1 shown in figure 3.7. $\overline{Z}_{\mathrm{eff}}$ increases from $1.3 - 1.4$ in the deuterium reference phase to $2.0 - 2.3$ with nitrogen seeding. The core nitrogen concentration, c_{N}, varies from a pre-seeding level of 0.5 % to $2.0 - 3.0$ % during seeding. Other impurities have been measured by charge exchange recombination spectroscopy before nitrogen seeding. The concentration levels of carbon and helium are $c_{\mathrm{C}} \approx 0.1$ % and $c_{\mathrm{He}} \approx 0.5$ %, respectively. The tungsten content is determined spectroscopically to be on the order of $c_{\mathrm{W}} \approx 5 \times 10^{-5}$. Time traces of the main control and plasma parameters of the exemplary discharge #29383 are shown in figure 4.1.

4.3 The Evolution of Detachment in H-mode

This section summarizes how the detachment evolves. It provides a framework for a more detailed analysis of the individual observations of different plasma quantities in the following sections. The observations described are common to all discharges included in the study. Similar to a classification, which was developed for the evolution of detachment in L-mode discharges in Ref. [1], the evolution of H-mode detachment can be divided into four phases that are indicated in figure 4.2:

   I. Onset of Detachment

  II. Fluctuating State

 III. Partial Detachment of Outer Target

 IV. Complete Detachment

Figure 4.2.a-b show the evolution of the sum of the ion saturation current density measurements in the lower divertor seperately for the inner and outer target, $I_{\mathrm{sat}} = \sum_{LP} j_{\mathrm{sat,LP}}$, where $j_{\mathrm{sat,LP}}$ are individual measurements from Langmuir probes shown in figure 3.7. For comparison a Two-Point Model scaling of I_{sat} is plotted. The scaling is given by $I_{\mathrm{sat,TPM}} = c_{t_0} \overline{n}_{\mathrm{e,edge}}^2$, where $\overline{n}_{\mathrm{e,edge}}$ is the line integrated edge density measured by the edge interferometer (H-5 in figure 3.7) as a proxy for the separatrix density and c_{t_0} is a normalization constant chosen such that $I_{\mathrm{sat}} = I_{\mathrm{sat,TPM}}$ at the reference time, t_0, with attached targets. For discharge #29383 in figure 4.2 the reference time is $t_0 = 0.9$ s for the inner target and $t_0 = 1.5$ s for the outer target. Experimental I_{sat} values below the scaling indicate a pressure loss along fieldlines, i.e. detachment.

I. Onset of Detachment:
During the onset of detachment after 0.9 s, I_{sat} to the inner target drops below the TPM-scaling in figure 4.2. The inner target detaches between ELMs without additional impurity seeding. The outer target stays attached. The early detachment of the inner target and the strong in-out asymmetry of the detachment is a regular observation in AUG H-modes. In fact it is a challenge to achieve the required low densities for fully attached targets in both divertors in H-mode discharges at AUG.

II. Fluctuating state:
At 1.3 s the inner target is detached and radiative fluctuations at the X-point with a frequency of $6 - 8$ kHz appear during inter-ELM phases. Figure 4.2.d shows these fluctuations in a power spectrogram of the intensity measurement of an AXUV bolometer chord at the HFS close to the X-point. ELMs in this phase are responsible for a transient sharp increase of I_sat at the targets as can be seen in the scatter of the unaveraged black trace in figure 4.2.a-b. Figure 4.2.c gives the standard deviation of I_sat in the down sampling interval and is a measure for the ELM size at the target. ELMs reattach the inner target transiently and the radiative fluctuations vanish. The outer target stays attached.

III. Partial detachment at outer target:
With the beginning of nitrogen seeding at 2.7 s the outer target changes from attached to partially detached in between ELMs. Analysis of the timing shows that the occurrence of radiative fluctuations at the X-point shifts gradually from in between ELMs to during ELMs. The fluctuation frequency decreases and merges with a band due to ELMs in the spectrogram in figure 4.2.d. After this transition the ELM size in both divertors is decreased considerably as can be seen by the reduction of the standard deviation of I_sat shown in figure 4.2.c. The inner target I_sat standard deviation vanishes, which indicates that the ELMs do not reattach the inner target anymore. Concomitantly, a strong localized radiation at the X-point is measured by bolometers and f_rad increases from about 50 % to about 85 %. A transient increase in line integrated density with ongoing detachment of the outer target by typically $10 - 20$ % is observed [121, 168, 201, 297]. At 3.1 s the inner vertical target component below the divertor baffle is completely detached.

In similar discharges with wider Langmuir probe coverage (#29924), the particle flux to the inner target in the far SOL above the divertor baffle, see figure 3.7, increases by a factor of about 2 with the onset of nitrogen seeding. Unfortunately, the coverage and spatial resolution of Langmuir probe measurements in the far SOL was not sufficient in these experiments to determine if the integrated target flux to the inner target, including the far SOL, is reduced or whether the particle flux is redistributed from the vertical plate into the far SOL.

IV. Complete Detachment:
Starting at 4.0 s particle flux in the far SOL at the the inner target rolls over. Simultaneously, the characteristic of a number of diagnostics measurements change (bolometer, outer target Langmuir probes, divertor shunt current, H_α). The signals first show signatures of high frequency ELMs with a broad frequency distribution and then change to small amplitude fluctuations without a fixed frequency or phase relation. Only sporadically, clearly distinguishable, inter-ELM-like events are observed. Meanwhile, the localized radiation at the X-point shifts further up into the confined plasma. Strong Balmer- and NIII-line radiation at the X-point emerges. Both spectral lines are indicators of increased ionization and rather low temperatures inside the confinement. Both targets are completely detached at 4.5 s. Particle and power fluxes at both targets are reduced to low levels.

In our experiments complete detachment seems to be intimately coupled to the appearance of MARFE-like radiation in the X-point region [198, 199]. The localized radiation proved to be reproducible, stable and well controllable. No radiation collapse occurred even with a change in N-seeding rates of up to a factor of 1.5. With the appearance of Balmer radiation in the X-point region the midplane profiles show a loss of pressure in the pedestal. The pressure reduction at the pedestal top ($\varrho_{\mathrm{pol}} = 0.95$) is about 60 % during complete detachment compared to the non-seeded phase. Despite the pedestal pressure loss, the core pressure profile inside $\varrho_{pol} < 0.7$ is only slightly affected. Hence, the overall confinement is only slightly reduced. H_{98} ranges from 0.8-1.0 with complete detachment compared to 0.85-1.05 in the non-seeded reference phase.

4.4 Detailed Analysis of Divertor Plasma

The observations during the evolution of detachment with nitrogen seeding are presented in more detail in this section. Each diagnostic group will be discussed along the sequence detachment states introduced above.

4.4.1 Target Profiles

Representative Langmuir probe and infrared camera target profiles for attached and completely detached conditions in #29383 are compared in figure 4.3. The profiles of j_{sat} and q_{t} are derived with the assumption of a sheath heat transmission coefficient $\gamma_{\mathrm{sh}} = 8$, $T_{\mathrm{e}} = T_{\mathrm{i}}$ and pure deuterium plasma ($Z_{\mathrm{eff}} = 1$) for the evaluation of the probe data. A significant nitrogen content in the divertor plasma could lead to an underestimation of n_{e} by the Langmuir probes [292]. Temperatures below 2 eV are likely to be overestimated [290]. Due to a low target plate surface temperature, the heat flux can be reliably diagnosed with infrared cameras only around the strike point (0 cm $< \Delta S <$ 5 cm) in our discharges. The profiles in figure 4.3 are ELM-synchronized and only data in between ELMs is included for the high recycling case. For the detached case no clear ELMs are observed anymore and no ELM synchronization is applied.

Qty	Reduction Factor	
	Inter-ELM	With ELMs
$I_{\mathrm{sat,in/out}}$	5 / 2.5	$\leq$100 / 2.5
	Average	
$P_{\mathrm{tar,in/out}}$	5 / 2	

Table 4.1: Reduction factors of peak fluxes to the targets from attached to completely detached targets are summarized for #29383 [104].

In all experiments of this study, the maximum of the j_{sat} profile at the outer target has been reduced by approximately one order of magnitude to values below 5×10^{22} m^{-2}s^{-1} during detachment, see figure 4.3.a. At the inner target the maximum was reduced to below 5×10^{21} m^{-2}s^{-1} already prior to the transition to complete detachment (not shown). Also the peak heat flux to the outer target has been reduced by more than a factor of 3 to below 0.5 MWm^{-2}. table 4.1 summarizes the reduction of the fluxes to both targets from the high recycling to the completely detached phase.
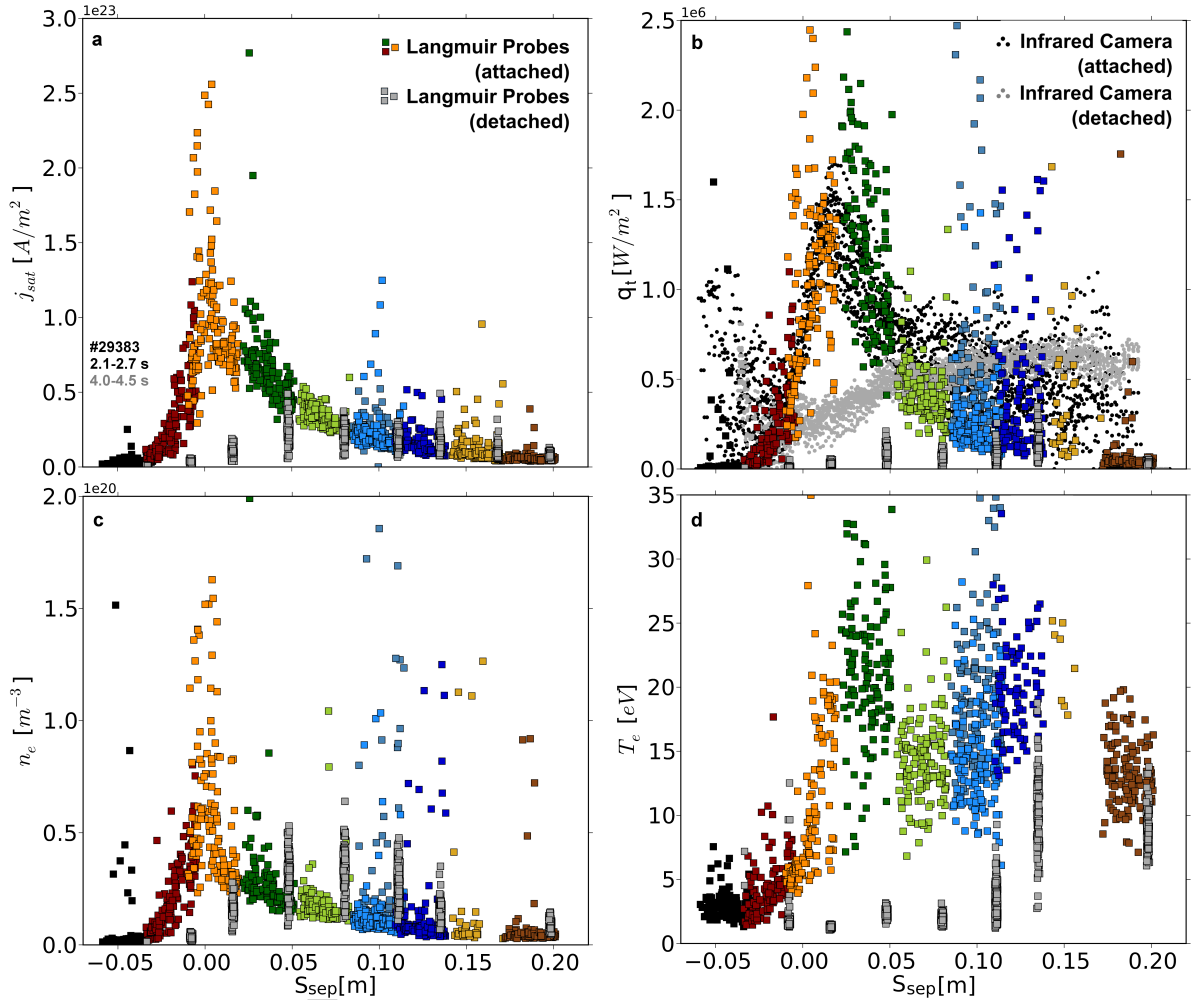
Figure 4.3: Inter ELM, outer target profiles of j_{sat} (a), q_t (b), n_e (c) and T_e (d) for #29383. Different colors signify individual Langmuir probes. Detached profiles are plotted in grey. No strikepoint sweeps are applied during detachment. The plotted time intervals are $20 - 2.3$ s (reference) and $4.0 - 4.5$ s (seeded). Figure adapted from Ref. [104].

Figure 4.3.d shows that the inter ELM electron temperature at the target decreased from $T_e \approx 10 - 30$ eV in high recycling conditions to $T_e \approx 1 - 2$ eV in detached regions.

4.4.2 Recycling & Line Emission

Spectroscopy combined with a database for atomic data [137] provides information about the temperature distribution and the spatial distribution of ionization in the divertor volume. This is particularly interesting with respect to the formation and evolution of radiation, ionization and recombination fronts during the detachment process as proposed in various detachment models [119, 143, 298], see figure 2.4. The spectroscopic measurements in our experiments comprise a singlet NII line at $\lambda = 399.60$ nm (3p-3s) and a doublet NIII line at $\lambda = 409.73/410.34$ nm (3p-3s) as well as the Balmer lines D_δ at $\lambda = 410.07$ nm and D_ε at $\lambda = 396.90$ nm. The fractional abundance of the coronal ionization equilibrium of nitrogen peaks at $5 - 10$ eV for NIII and $1 - 5$ eV for NII, see figure 3.8. Hence, the NIII line emission is an indicator for the ionization region

of neutral deuterium and the NII line is most intense in regions where charge exchange collisions should start to become important. The high Balmer lines $D_{\delta,\varepsilon}$ are indicators for recombining plasma. Stark broadening analysis of the D_ε and D_δ lines provides electron density, $n_{e,Stark}$, in the volume [299].

Figure 4.4 schematically shows the changes of the spatial distribution with proceeding detachment of the electron density and Balmer, I_{D_δ}, as well as nitrogen, I_{NIII}, line intensities in the divertor volume. Figure 4.4.a shows the divertor for attached targets and in the fluctuating state with a detached inner target (FS). As the inner target detaches the region of high electron density moves along the inner target to the divertor baffle, where the label 'FS' is shown in figure 4.4.a. The particle flux to the vertical inner target is reduced to very low values ($j_{sat} \leq 5 \times 10^{21}$ m^{-2}s^1). The high density region in the inner divertor is also seen to move away from the inner target towards the X-point. In the attached and fluctuation state, the Balmer radiation in the inner divertor is concentrated along the target plate in the inner divertor leg. The outer divertor stays attached during this evolution. The outer target profiles of the line radiation and the electron density peak at the strikepoint and the maximum is located close to the target plate.

With nitrogen seeding the outer divertor detaches partially at first as shown in figure 4.4.b. The inner divertor volume below the X-point height does not show significant line emission ($I < 5 \times 10^{18}$ Ph sr^{-1}m^{-2}s^{-1}) anymore and Stark broadening measurements limit the electron density to $n_{e,Stark} < 5 \times 10^{19}$ m^{-3} in this region. This is in line with very low particle fluxes measured by Langmuir probes at the inner vertical target. The vertical line of sight adjacent to the inner target plate, i.e. at the divertor baffle, shows a reduction in D_δ by a factor of 10 and the density drops from $n_{e,Stark} = 5$–6×10^{20} to 2–3×10^{20} m^{-3}. In contrast, the Langmuir probes at the inner target above the baffle, i.e. in the far SOL, measure an increase in j_{sat} of up to a factor of 4. A similar increase in j_{sat} at the outer far SOL target is seen in similar discharges with wider Langmuir probe coverage (#30308). Such an increase was not expected and is discussed in more detail in section 4.4.6. With nitrogen seeding $n_{e,Stark}$ at the outer strikepoint reduces by a factor of 2. Initially, the line intensities I_{D_δ} and I_{NIII} increase along the whole outer target by a
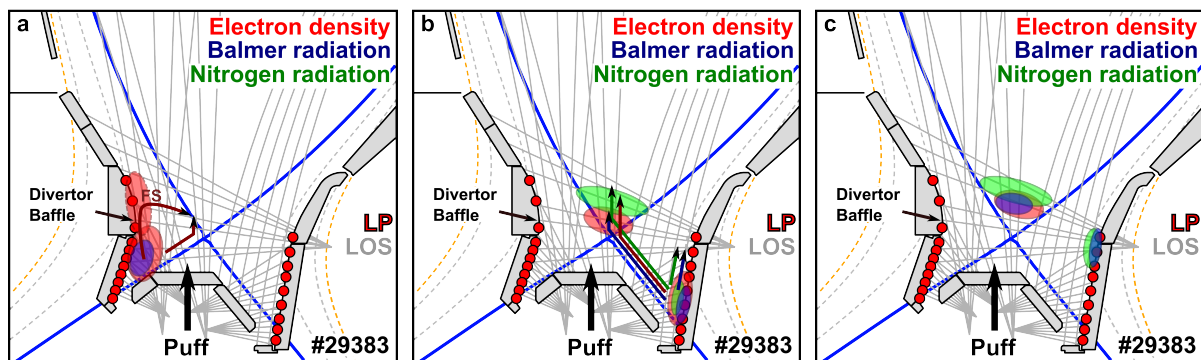

Figure 4.4: Divertor evolution during detachment measured by spectroscopy. Active Langmuir probes are shown in red. The LOS geometry of the divertor spectroscopy is shown in grey. The transition from attached and fluctuating state (label FS) (a) to partially detached outer target and to completely detached targets (c) is shown. Figure adapted from Ref. [104].

factor of 4 to 6 and 3, respectively. At first the profiles still peak around the strikepoint. Subsequently, with the partial detachment around the outer strikepoint the maximum emission moves away from the strikepoint along the target as indicated by the arrows in figure 4.4.b. Simultaneously, a second emission region of NIII moves to the X-point and additional NIII line emission emerges above the X-point inside the confined plasma.

In summary, the observations up to this phase show that the inner divertor detaches completely, while the outer target shows partial detachment around the strikepoint. In the inner divertor the vertical target below the divertor baffle and the far SOL target above the baffle behave differently, indicating that the divertor baffle with its change in target orientation might play an important role in determining the exact detachment evolution in the inner divertor.

With the transition from partial detachment at the outer target to complete detachment, see figure 4.4.c, the maximum in the Balmer and NIII-emission moves further up the outer target plate and the profiles flatten out. Concomitantly, the NIII emission region above the X-point moves radially further inward and below it strong Balmer radiation emerges inside the separatrix. A region with high electron density at the X-point coincides in this phase with the Balmer emission zone. The presence of significant D_δ Balmer radiation above the X-point is unexpected. It indicates low temperatures in the 1-10 eV range inside the confined plasma close to the separatrix. Together with a midplane separatrix temperature in the range of 60-100 eV this implies strong parallel temperature gradients on closed fieldlines. The electron density profile along the outer target has now a minimum at the strikepoint with $n_{e,Stark} = 1 \times 10^{20}$ m^{-3} and is flat for $\Delta S = 5$ cm with $n_{e,Stark} \approx 3 \times 10^{20}$ m^{-3}. The profile is similar to the Langmuir probe measurements in shape, but the Langmuir probes measure significantly lower density $n_{e,LP} = 2 - 4 \times 10^{19}$ m^{-3} as shown in figure 4.3.c. The discrepancy in the measured electron density of spectroscopy and Langmuir probes is about a factor of 10. This discrepancy indicates that the ionization front and hence the maximum in electron density has moved away from the target surface. For the density to drop as strongly as suggested by the Langmuir probes, a recombination region should be present in front of the target [143]. With the emerging Balmer radiation at the X-point, Langmuir probe measurements indicate a decrease of j_{sat} in the far SOL of both divertors. The spectroscopic electron density, $n_{e,Stark}$, at the inner divertor baffle reduces by another factor of 2.

The observations of the plasma evolution that leads to complete detachment show that with increasing partial detachment of the outer target a qualitative change in the divertor from divertor to X-point dominated radiation takes place. This transition does not only change the divertor plasma, but establishes very low temperatures inside the confined plasma. Unexpectedly, the intense, localized radiation at the X-point seems to be able to sustain significant parallel temperature gradients along closed fieldlines without driving the plasma unstable.

Information on the plasma and the recycling in the main chamber is provided by limiter spectroscopy at AUG. It observes the outboard limiter from the top of the inboard limiter, see figure 3.7. The limiter spectroscopy includes D_ε, NII, NIII and WI line intensities. The intensities of these lines change with the application of nitrogen seeding. The nitrogen line intensities at the limiter increase by about a factor of 4, whereas the

tungsten line intensity decreases. Thus, less tungsten influx (sputtering) is observed from the limiters despite an increased nitrogen recycling. The Balmer line intensity evolution observed with the limiter spectroscopy scales with the neutral flux measurement behind the HFS limiter (F11) and the far SOL density measurement in the inner divertor (V2), see section 4.4.6. The increased Balmer line intesity could be interpreted as a reduction in local recycling at the LFS limiter (S/XB). However, it is also possible that diffuse reflections of the local emission from the HFSHD region in the inner divertor at the limiter could be detected by the limiter spectroscopy as an increased Balmer line intensity.

4.4.3 Radiation Losses in the Divertor

Radiation in the divertor volume disperses power and reduces the plasma temperature to values necessary for detachment. Bolometers measure the radiated power along a line of sight and the location of the radiating regions can be deduced. In AUG the total radiated power, P_{rad}, is measured by foil bolometers and a fast evaluation of P_{rad} is used to determine f_{rad}. In our detachment studies f_{rad} increases from 50–60 % in unseeded reference phases to 80–90 % during nitrogen seeding with radiation at the X-point. A tomographic reconstruction of the radiated power density of discharge #29383 without and with nitrogen seeding is shown in figure 4.5. The evolution of the total radiation in the bolometer measurements is similar to that of the NIII-line emission observed with divertor spectroscopy: In the non-seeded phase the bulk of the radiation stems from the inner divertor as shown in figure 4.5.a. With the onset of nitrogen seeding the dominant radiation first shifts to the volume of the partially detached outer divertor and then to the X-point as the divertor detaches completely, see figure 4.5.b. The radiation moves into the confined plasma to above the X-point. At the same time also NIII and Balmer line radiation is spectroscopically observed inside the confined region. The X-point radiation is correlated to the maximum pressure loss along a field line from upstream to target, an upstream pressure loss at the
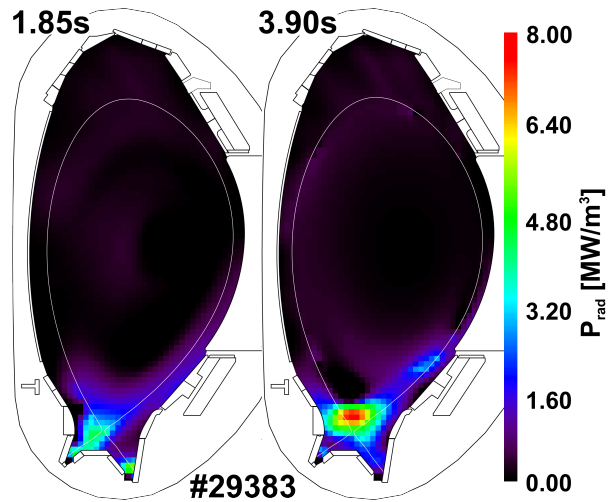

Figure 4.5: Tomography of bolometer measurements without (1.85 s) and with (3.9 s) nitrogen seeding. The radiation characteristic changes from detached inner divertor to stable, MARFE-like X-point radiation [104].
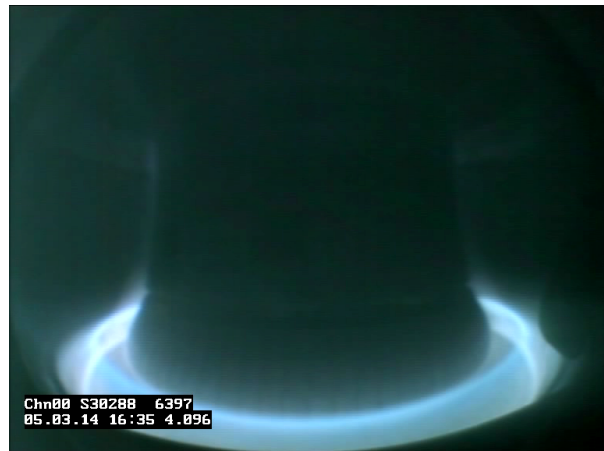

Figure 4.6: X-point radiation in a nitrogen seeded, low-power L-mode discharge (#30288).

pedestal top, see section 4.5, and completely detached targets. In this phase, ELMs are suppressed and replaced by broadband fluctuations, see section 4.5.1.

Similar X-point radiation connected to detachment has already been observed in a number of experiments [129, 131, 300, 301]. However, the experimental observations located the X-point radiation either outside of the separatrix (DIII-D) or did not comment on its stability and stationarity (JT-60U). In the detachment studies presented here the MARFE-like X-point radiation proved to be reproducible and stable, but not stationary. The radiating region shows an ongoing radial inward movement on a slow timescale of 1 s. The experimental observation that the X-point radiation reacts to a reduction of the seeding rate on a time scale of several 100 ms should allow for a feedback control of the X-point radiation position using the nitrogen seeding rate as the actuator and bolometer lines of sight as a controller. More importantly, this indicates that the X-point radiation itself is in equilibrium, while the divertor conditions are still slowly evolving.

The radial emissivity profile at the midplane, excluding the X-point radiation, during nitrogen seeding peaks at $0.8 < \varrho_{pol} < 1.00$. Such a peak in the edge of the confined region is only expected for non-coronal enhancement of the radiation cooling factor, L_Z, [92, 302].

4.4.4 Radiative Fluctuations

AXUV diode bolometers at AUG provide insight into the fast dynamics of the radiation distribution. The AXUV diodes show radiative fluctuations in lines of sight close to the HFS of the X-point. Such fluctuations are shown for discharge #28903 in figure 4.7.a-c. The observations during the fluctuating state are consistent with what was reported in Ref. [108]. The fluctuations are first observed in between ELMs when the inner divertor is detached along the vertical target, figure 4.7.a. ELMs transiently reattach the
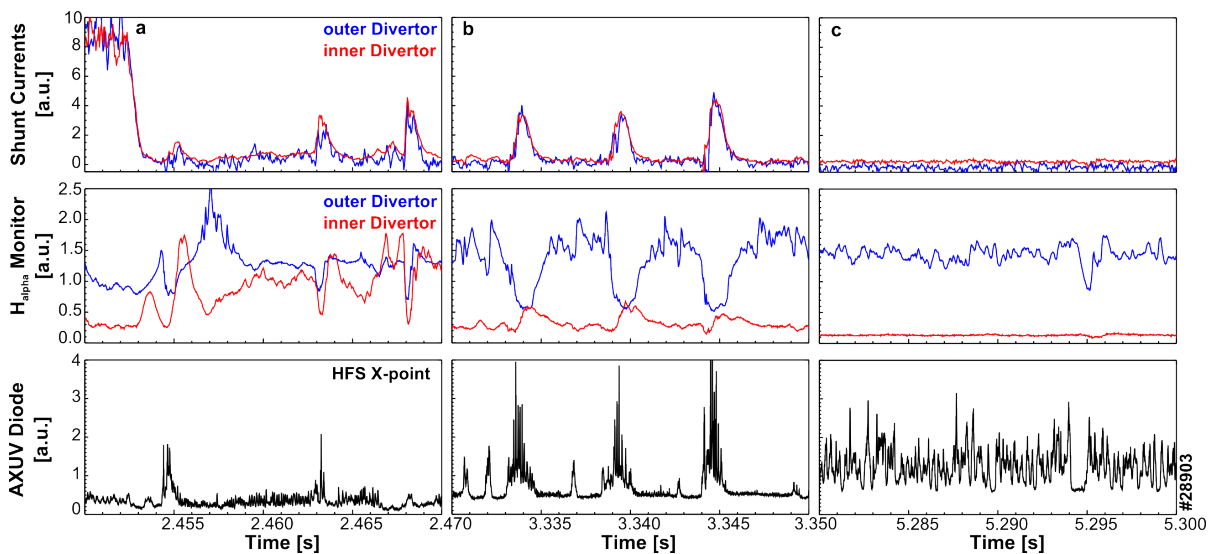

Figure 4.7: Radiative Fluctuations measured by HFS X-point AXUV line of sight. Fluctuations change from ELM (a) to inter-ELM time intervals (b) and then vanish (c).

inner target and the radiative fluctuations disappear during the ELM. With advancing
detachment during nitrogen seeding the outer divertor detaches first in between ELMs
and then permanently. Accordingly, the radiative fluctuations switch from in between
ELMs to during ELMs, see figure 4.7.b, and then vanish with detachment of the outer
target. Hence, the appearance of the radiative fluctuations seems to correlate with
a simultaneously detached inner target and attached outer target. The frequency of
the radiative fluctuations decreases with nitrogen seeding as shown in figure 4.3.d. In
Ref. [108] a correlation of the radiative X-point fluctuations with the occurrence of a high
field side high density region in the inner divertor is observed. In our experiments the
radiative X-point fluctuations are clearly distinguishable in the bolometer signals from
the broadband ELM distribution until the high density in the inner divertor region is
completely eliminated by nitrogen seeding, see figure 4.11. With complete detachment
uncorrelated broadband fluctuations, that are distinct from the previously described
fluctuations, appear, see figure 4.7.c.

4.4.5 Tungsten Erosion

As discussed in section 1.6 a limitation of the core
contamination with tungsten is crucial for plasmas
with good confinement. In AUG plasma-wall in-
teraction at the main chamber wall and in the di-
vertor releases tungsten into the plasma [75]. For
the presented discharge scheme the tungsten con-
tamination of the core plasma is moderate ($c_W <
5 \times 10^{-5}$), if fast cooling of the divertor by a prompt
increase of the nitrogen seeding rate to levels in the
range of 1×10^{22} e$^-$s^{-1} is applied. In discharges with
high heating power the fast cooling avoids an ini-
tial phase with an attached divertor, during which
the tungsten influx is enhanced by sputtering at the
divertor plate by nitrogen.

Spectroscopic measurements in the divertor, DVL
in figure 3.7, and at the LFS limiter use the WI
line at $\lambda = 400.9$ nm as a measure of the tungsten
influx using the S/XB-method described in chap-
ter 3. The inter-ELM tungsten influx in the outer
divertor close to the strikepoint is suppressed as
soon as the Langmuir probe at this position mea-
sures $T_e \leq 5$ eV, see figure 4.8. The reduction in
ELM size with nitrogen seeding is also very bene-
ficial since enhanced tungsten influx during ELMs
is no longer observed with a completely detached

Figure 4.8: Fast cooling of the di-
vertor by a fast ramp-up of the ni-
trogen seeding leads to an almost
complete suppression of W-erosion at
the divertor target and the low-field
side limiter. The critical temperature
at the observed region close to the
strikepoint is $T_e = 5$ eV [104].

divertor. Spectroscopy at the LFS limiter also observes a reduction of tungsten influx
from the main chamber walls with nitrogen seeding both in between ELMs and during
ELMs. Due to the limited time resolution of the limiter spectroscopy a full resolution of
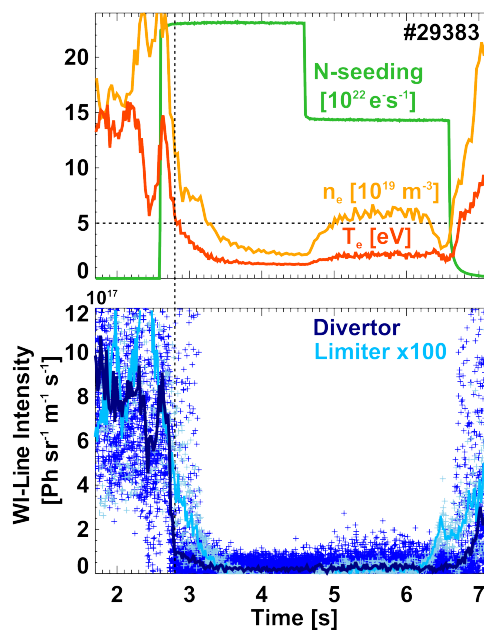
the ELM periods is only possible at low ELM frequencies prior to nitrogen seeding.

The fast cooling of the divertor leads to a fast transition to detachment. This is desirable for protecting the divertor, but is a challenge in diagnosing the divertor plasma in this phase. Attempts at discharges with a slow ramp up of the nitrogen seeding, instead of the fast cooling approach, tended to disrupt due to a radiative collapse that was induced by tungsten accumulation. This behavior can be explained by the competing effects of nitrogen seeding on tungsten erosion. A higher nitrogen content in the divertor plasma increases the nitrogen flux fraction to the target. With higher charge ($Z > 1$), nitrogen is accelerated to higher energy by the sheath potential drop. Additionally, the momentum transfer to tungsten is more efficient with the larger mass of nitrogen.

This makes sputtering by nitrogen much more efficient than by deuterium. An increased tungsten content of the core plasma can lead to central impurity accumulation with a disruptive radiative collapse of the plasma. Moreover, with a sufficient temperature reduction at the target plates by nitrogen line radiation, a suppression of the sputtering can be achieved. As a result the core tungsten content stays low without the risk of tungsten accumulation. An evolution of the tungsten source in a JET discharge can be seen in figure 4.9. As described, the data shows that only after a sufficient temperature reduction by seeding the sputtering is reduced.
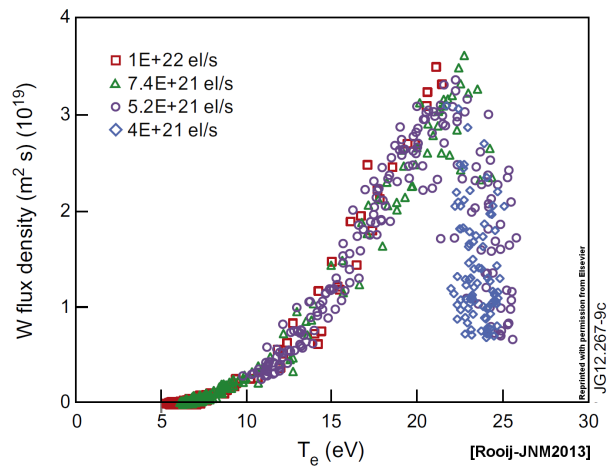

Figure 4.9: Impact of temperature and impurity seeding om tungsten influx in a JET discharge with nitrogen seeding [284].

4.4.6 Fueling, Neutral Pressure Evolution & High Field Side High Density

The poloidal neutral pressure distribution in a tokamak is determined by the recycling sources, neutral conductances through the structural components behind the plasma facing components and the details of the particle pumping in the machine. The neutral pressure distribution determines the available neutral particles for ionization in the plasma and influences the details of the fueling of the plasma. At AUG the neutral pressure distribution is monitored by a number of poloidally distributed ionization gauges that are shown in figure 3.7. Different gauge sensitivities for N_2 and D_2 make a quantitative analysis of the neutral pressure during strong nitrogen seeding without knowledge of the actual nitrogen concentration difficult. A spectroscopic determination of the nitrogen concentration in the pump chamber failed to deliver conclusive results, see chapter 3.

Gauges	low Γ_D	high Γ_D
F07/F14	300	600
F07/F12	8	5
F07/F11 (no-N)	12 (1-2)	5 (1-2)
F07/F09	1.5	0.5
F05/F06	1.5	2

Table 4.2: Neutral pressure distribution for high and low deuterium fueling rates.

Timetraces of the neutral pressure are shown in figure 4.11. Most gauge signals follow the trend of the roof baffle gauge (F07) and increase with nitrogen seeding. With the onset of seeding, an initial change in the neutral pressure ratios as listed in table 4.2 by up to 25 % is observed. Surprisingly, the ratios change only slightly by about 5–10 % during the sequence of the different divertor phases. The magnitude of the neutral pressure itself also seems to have no effect on the pressure ratios, which depends foremost on the puff rate. The pressure ratio evolution for a discharge with a scan in deuterium fueling (#29925) is shown in figure 4.10.

A change in the pressure ratios could be induced either by a change in conductance, by a change in local impurity concentration or by a change in the neutral source distribution. A change in conductance should depend on the neutral pressure, especially if the neutral gas changes the transport regime from ballistic to collisional. Such a change with the neutral pressures is not observed, which indicates that the neutral transport regime in the subdivertor structures does not change. To study the effect of the local impurity concentration, the ratio of the mass spectrometer signals for N_2 (m=28) from the HFS (HPQI) and the LFS (HPQO) normalized by the local neutral pressure or the concentration from an improved spectroscopic gauge F12 could be used. Both measurements were not available at the time of the experiments.

The determination of the neutral source distribution is not easily done and only major changes can be clearly observed. Such a change in the recycling at the inner far SOL target is seen with the evolution of a high field side high density region, HFSFD, in the inner divertor [108, 127]. This HFSHD changes a HFS gauge measurement (F11): With the transition from the onset of detachment to the fluctuating state, a HFSHD region is formed in the far SOL of the inner divertor up to the divertor baffle. HFS reflectrometry measurements and visible video diagnostics indicate that this HFSHD region might extend up to the midplane. Along with spec-
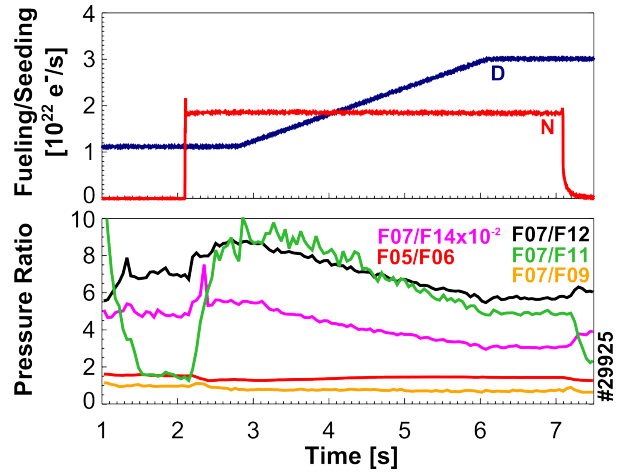

Figure 4.10: Neutral pressure distribution during deuterium puff ramp.
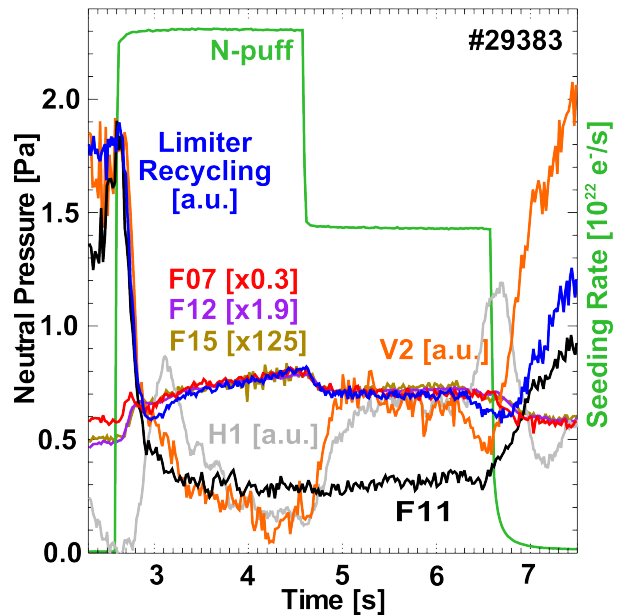

Figure 4.11: Timetraces of neutral pressure measurements, spectroscopic measurements of limiter recycling, nitrogen seeding rates and high-field side density (V2) are shown. Figure adapted from Ref. [104].

troscopy [299] and the vertical CO_2-interferometer chord V2 [238], the HFS limiter gauge observes the HFSHD by an increase in neutral flux. The neutral pressure at the HFS gauge and the baratron below the inner divertor (B-Fu) are coupled. At this stage the pressure drop from behind the inner divertor (B-Fu) to below the roof baffle (F07) is small. With the onset of nitrogen seeding and partial detachment of the outer target our experiments show a drop of the HFS density at the inner divertor baffle by a factor of 2–4, accompanied by a neutral pressure drop by a factor 3–4 at the HFS limiter gauges (F11) and by about 25–50 % below the inner divertor (B-Fu). The baratron pressure decouples from the HFS gauge pressure and a significant pressure drop from behind the inner divertor to below the roof baffle is established. The experimental data suggests that the HFSHD region in the inner divertor is a source of neutrals that sustains the high neutral pressures in the HFS divertor and below the roof baffle. The correlated increase of the baratron B-Fu and the HFS gauges (F11) to similar pressures without a similar change below the roof baffle (F07) indicate that neutral conductance through the slits between the inner divertor tiles is important. This might be particularly important for the neutral conductance model in future numerical modeling, see chapter 5.

Correlated to the extinction of the HFSHD, an increase of the far SOL j_{sat} at the inner target was observed in section 4.4.5. The increase in local recycling at the inner far SOL plate up to at least $\Delta S = 0.35$ m seen in Langmuir probes seems at first to be in contradiction to the reduced neutral flux measurements of the HFS gauge (F11) and the reduced baratron neutral pressure. However, shielding of the target from parallel ion fluxes by the vanishing HFSHD through increased recombination and charge exchange collisions could have been responsible for a suppression of the ion flux before the seeding. A reduced shielding of neutrals would lead to an increase of j_{sat} in the far SOL and reconcile the Langmuir probe and neutral flux measurements. Unfortunately, this explanation does not apply to the outer divertor, where a similar evolution of j_{sat} is seen in the far SOL. Another possible explanation could be the increase in radial transport in the SOL by blobs with increasing degree of detachment that has been measured in Ref. [303].

Similar to observations on AUG in Ref. [169], the HFS density measured along the interferometer chord V2, see figure 3.7, scales well with the power reaching the inner divertor target, $P_{\text{tar,in}}$. The decrease in the HFS density is correlated in time to the increase of line integrated electron density along the interferometer chord H1 by $10-20$ %, a drop in main chamber recycling deuterium fluxes and a fast increase in the divertor neutral pressure. The timescales of these changes are comparable, see Figures 4.2 and 4.11. The concomitance suggests not only a change in the recycling pattern close to the plate, but also a correlated impact on core plasma fueling and main chamber recycling. The increase of the line-integrated density with detaching targets is also observed in Ar- and Kr-seeded discharges in AUG [96], in AUG L-modes [169] and in JET H-mode density limit studies [129]. The observations indicate that by the reduction of the HFS density an additional gas reservoir is tapped, which fuels the main plasma. In most of our discharges, the initial increase in line integrated density is only transient. With proceeding detachment and the appearance of NIII-line radiation at the X-point the line integrated electron density decreases again and the neutral pressure in the divertor increases further. A transition to complete detachment and X-point radiation seems to

induce the decrease in the electron density, effectively reducing the particle confinement time.

A characteristic divertor performance measure for pumping efficiency is the neutral compression, c. It is defined by the ratio of the neutral density in the (sub)divertor and the main chamber. It describes the ability of the divertor to enrich neutrals in the divertor for better pumping. In our experiments, c varied in a range from 300–600, see table 4.2, for different discharges. Unexpectedly, within a discharge and with a transition to detachment c varied only slightly by about $5-10$ %. The neutral compression determined from ionization gauges (F07/F14) stays high of the order of $c = 100$ during complete detachment. As mentioned above, a fast decrease of the neutral compression of about 25 % with the beginning of nitrogen seeding is observed.

A characteristic divertor performance measure for the ability of the divertor to retain impurities is the impurity retention, η. The impurity retention is given by the ratio of the impurity densities in the divertor and the core plasma. It describes the ability of the divertor to keep impurities from escaping the divertor to the main chamber, where they can possibly have a detrimental impact on the plasma performance. Unfortunately, the impurity density in the divertor is not readily obtained and the line intensity of a low ionization state ion must be used as a proxy. The required implicit assumption for such an analysis for different plasma regimes is that the plasma parameters n_e and T_e do not change significantly along the line of sight. This can be valid within a single discharge scenario, but is of course not the case in a transition from attached to completely detached targets. We can resort to using the ratio of the neutral impurity influx at the divertor target (S/XB) and the core impurity density. We obtain a modified η^* ranging from $1.3 - 2.7 \times 10^4$ during nitrogen seeding. Lower values of η^* are observed for lower deuterium fueling and higher heating power. A higher strikepoint or X-point position decreases η^* as well.

In the fueling scan previously discussed (#29925) not only the neutral pressure distribution changes, but also the core impurity content, the ELMs and the confinement vary with increasing fueling rate, Γ_D, at constant seeding, Γ_N. The nitrogen and tungsten concentrations, the radiated power, the ELM frequency, confinement and the line integrated electron density decrease with increasing Γ_D, whereas the ion flux to the target and the ELM size increase.

4.5 ELMs, Upstream Profiles & Confinement

4.5.1 ELMs & SOL Fluctuations

In our experiments ELMs of type-I and type-III appear during the unseeded phase. Figure 4.13 shows the ELM frequency and the fluctuation level of the I_{sat} signal from the Langmuir probes at both divertor targets as measure of the ELM size. Consistent with Refs. [106, 123, 260], type-I ELMs are gradually replaced by smaller type-III ELMs with the onset of nitrogen seeding. The frequency of the type-III ELMs increases with increasing degree of detachment of the outer target from $f_{ELM} \approx 200$ Hz into the kHz-
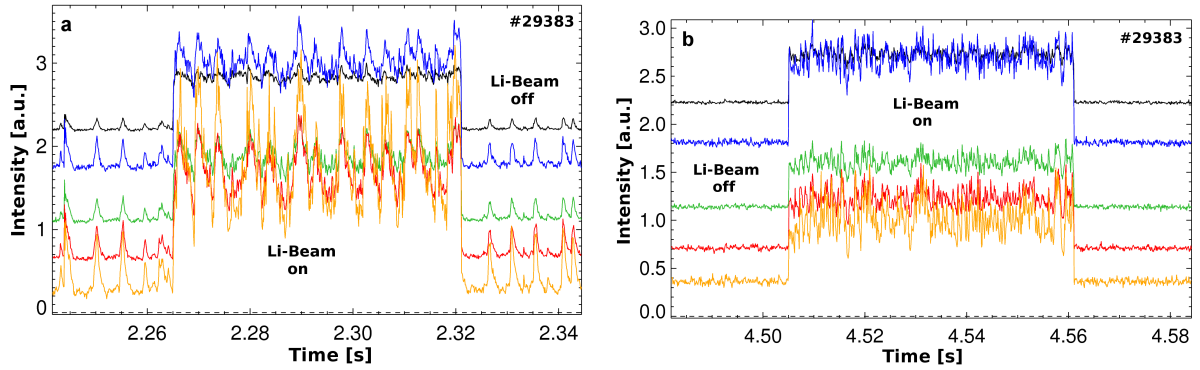
Figure 4.12: Filtered photodiodes from the lithium beam diagnostic measure different fluctuation amplitudes in attached (a) and detached (b) conditions. The fluctuation amplitude increases in the radial direction into the far SOL (black to orange).

range and the ELM size decreases significantly. The change in the stored thermal energy of the plasma decreases from 10–15 kJ to below 2 kJ. With the transition to complete detachment the impact of ELMs on the target ion saturation current is reduced by about a factor of 4 for the outer target, see figure 4.13. At the same time, the rather well defined ELM frequency changes into a broadband frequency distribution. In discharges with low X-point position the ELMs transform into high-frequency, broadband fluctuations without fixed phase relation and without clear ELM signatures. ELM suppression occurs. The incoherent fluctuations can be observed in the fast AUXV diode bolometers, the target shunt current and the divertor D_α diode measurements, see figure 4.7.c. The transition from ELMs to broadband fluctuations is correlated to a pressure loss in the pedestal and the appearance of Balmer radiation inside the confined plasma during the X-point radiation phase with complete detachment.

The replacement of large type-I ELMs by small type-III ELMs with strong nitrogen seeding can be interesting for plasma operation of future devices. During complete detachment with the MARFE-like radiation at the X-pointer even ELM mitigation and suppression can be observed. The small or mitigated ELMs are obtained at rather high confinement of $H_{98} = 0.8 - 1.0$ and a relatively low increase in Z_{eff} with $\Delta Z_{eff} = 0.7 - 1.0$. An H-mode with type-III ELMs would be beneficial for target protection in ITER and such operation has been suggested [66]. Along with the change of ELMs, the fluctuations in the SOL seem to evolve with progressing detachment. This is consistent with L-mode observations in AUG [303, 304]. Figure 4.12 shows the active (beam on) and passive (beam off)
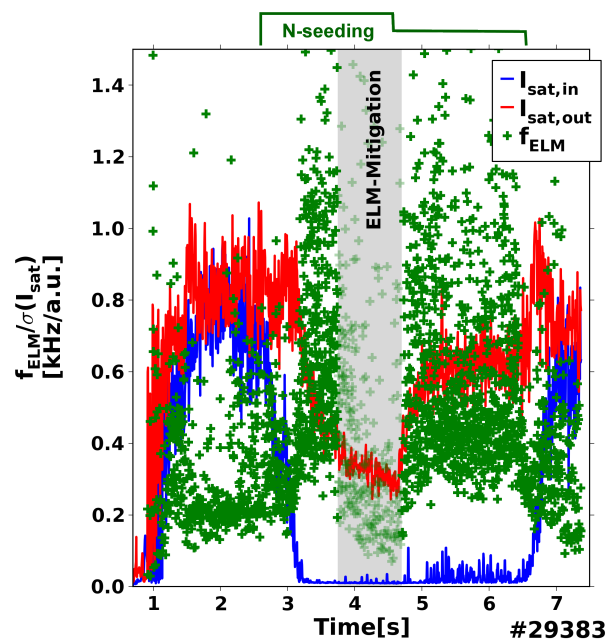

Figure 4.13: Standard deviation of I_{sat} from inner (blue) and outer (red) divertor is plotted as measure for the ELM size in the divertor. The ELM frequency (green) increases dramatically with nitrogen seeding. The shaded region of the ELM frequency is an interval without clear ELM signatures but broadband, high frequency fluctuations. Figure adapted from Ref. [104].

intensity measured by the lithium beam
photomultipliers. The fluctuation ampli-
tude between ELMs is significantly en-
hanced in the completely detached phase
and increases in the radial direction into
the far SOL.

For low power H-modes of our series with
$P_H \approx 5 - 6$ MW the ELMs are absent during the whole seeding phase. This triggered
an investigation if the discharges are still in H-mode or already L-mode like. A com-
parison of reflectometry data as an indicator of the turbulence level showed that the
fluctuation amplitudes in the pedestal are reduced with respect to regular L-mode, but
are enhanced with respect to 'regular' H-mode phases. These low power discharges are
in fact degraded H-modes with a reduced confinement factor of $H_{98} \approx 0.80 - 0.85$. In-
stead of high frequency ELMs they feature the broadband fluctuations, that are usually
observed during complete detachment.

4.5.2 Upstream Profiles & Confinement

A relevant plasma scenario that is optimized for power exhaust must as well be com-
patible with the requirements of plasma performance and confinement properties for the

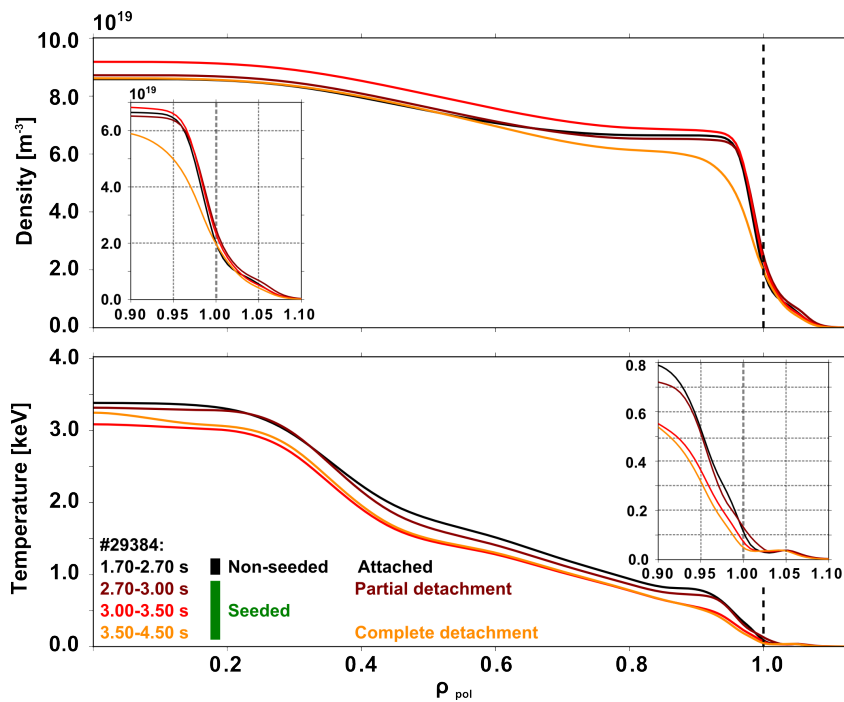**Figure 4.14:** Midplane profiles of electron density and temperature from non-seeded ref-
erence phase (black - $1.7 - 2.7$ s) to completely detached phase (orange - $3.5 - 4.5$ s) of
discharge #29384. Profiles are ELM-synchronized and only inter-ELM measurements are
shown, except for the completely detached phase. The ion temperature behaves similar to
the electron temperature and is not shown for clarity [104].

operation of a future reactor. In this section, therefore, the midplane profiles and the confinement of the presented detachment scenario is investigated.

As regularly observed on AUG [305, 306] confinement improves with nitrogen seeding before the transition to a detached outer target by $\Delta H_{98} = 10$–20 % in most of our discharges (e.g. #29925). If discernible in the fast evolution, the partial detachment of the outer target seems to be associated with a reduction of H_{98} by about $10 - 20$ %. Hence, the confinement improvement by nitrogen seeding is masked by a confinement loss due to detachment and/or the change of ELM activity. In the discharges in our study, the overall confinement, described by H_{98}, is reduced by 5–10 %, when comparing the non-seeded phase with the completely detached phase.

For a more detailed analysis of this confinement loss, the midplane profiles of n_e and $T_{e,i}$ of discharge #29384 are analyzed. Discharge #29384 differs from #29383 only in a 33 % higher deuterium fueling. Figure 4.14 shows the profiles for attached, unseeded and completely detached conditions. With the transition to a detached outer target $(2.7 - 3.5$ s$)$ the pedestal $(\varrho_{pol} = 0.95)$ temperature, $T_{e,ped}$, reduces by about 40 %, while the pedestal density, $n_{e,ped}$, does not change. The pressure loss is about 40 %. Once the outer divertor is completely detached and Balmer radiation appears inside the confined region above the X-point $(3.5 - 4.5$ s$)$ $n_{e,ped}$ is reduced by about 25 % and $T_{e,ped}$ is diminished by another 15 %. The pedestal top pressure is largely reduced by about 60 % compared to the unseeded value. The pedestal top values stabilize at $n_{e,ped} \approx 5 \times 10^{19}$ m^{-3}, $T_{e,ped} \approx T_{i,ped} \approx 300$ eV. The ion temperature (not shown) and the electron temperature are well coupled in the pedestal and $T_e \approx T_i$ holds true during this evolution.

Despite the reduction in pedestal top pressure and a loss in confinement, it is important to note that the core profile values inside $\varrho_{pol} < 0.7$ are reduced only by about 10 % during the phase of complete detachment. The profile data suggests that increased gradients in the region from $0.8 < \varrho_{pol} < 0.95$ recover most of the pedestal top pressure loss towards the core [61].

The large pedestal pressure loss and the large reduction of power into the divertor by the X-point radiation facilitate detachment and target protection largely. The impact on the core plasma inside $\varrho_{pol} < 0.7$ is comparably small. The plasma performance is not decreased tremendously as the pressure loss is concentrated on regions that does not contribute to the active volume for fusion reactions of the core plasma. The confinement loss at the edge of the core plasma is in fact beneficial for the divertor without a similar effect on the central part of the core plasma.

4.6 Divertor Geometry Effects

Divertor geometry effects on detachment have been studied with a vertical scan of the X-point height, which changes the closure of the divertor. A significant impact has been found on the impurity retention and the fueling of the core plasma. Our experiments show that the line integrated electron density and hence the fueling efficiency, $F = \overline{n}_e/(\Gamma_D + \Gamma_N)$, is sensitive to the position of the X-point or the strikepoint. A vertical

scan of the X-point moved the strikepoints twice by $\Delta S = 3$ cm up along the target. Both times the line integrated density increased by about 10 % despite constant fueling and seeding rates. The nitrogen core concentration, along with the nitrogen main chamber recycling, increased each time by about 15 %. The tungsten core concentration decreases from 5×10^{-5} by 40 and 30 % despite strongly increasing LFS limiter tungsten sources (x10). The confinement changes from $H_{98} \approx 0.85$ to 0.88. With the strikepoint position moving upward the ELM frequency decreases and the frequency distribution changes from broadband to a usual narrow frequency band. With increasing strikepoint height the neutral compression in the divertor increases and the ion flux to the target reduces further. In similar experiments with a strikepoint scan it was observed that the HFS high density region is largely fixed in position to the inner divertor baffle [127], see label 'FS' in figure 4.4. The MARFE-like X-point and the target radiation profiles relative to the X-point and the strikepoint position are unchanged.

The reaction to a change in the clearance between the separatrix and the outer wall (R_{aus} scan) is less clear, because such a scan is automatically coupled to a strikepoint scan at the targets. In line with Ref. [75] our experiments indicate that the tungsten concentration is very sensitive to R_{aus}. Subsequently, the electron temperature and confinement are affected by the additional radiation cooling due to increased tungsten content.

4.7 Extension to ITER-relevant Plasma Scenarios

The presented experiments have been executed at a plasma current of $I_{\mathrm{P}} = 800$ kA and a safety factor of $q_{95} \approx 5.0$. The stability, controllability and reproducability of the plasma scenario in combination with the unexpectedly minor confinement loss with complete detachment is a prerequisite for the application of such a scheme in a future fusion device. In additional experiments an extension of the above observations to a more reactor like plasma regime has been explored. The baseline scenario of ITER is supposed to operate at a safety factor of $q_{95} = 3.0$ and will have substantially higher line integrated electron densities and neutral pressures in the divertor [55, 62]. By increasing the plasma current in our experiments to 1.2 MA a $q_{95} \approx 3.5$ is reached. Higher line integrated electron densities up to 1×10^{20} m^{-3} and higher neutral pressures in the divertor up to 5 Pa are achieved. The heating power was increased to reach ITER-relevant power densities P_{H}/R, which is a measure of the severity of the power exhaust problem [99, 297, 307, 308]. Stable complete detachment has been achieved for heating power of up to $P_{\mathrm{H}} = 10 - 13$ MW at $I_{\mathrm{P}} = 1$ MA with good confinement of up to $H_{98} \approx 0.95$. In first, unoptimized experiments with a heating power up to $P_{\mathrm{H}} = 18 - 20$ MW, which corresponds to $P/R \approx 7 - 9$, and at neutral pressures of up to 8 Pa detachment has been achieved at relatively low confinement of $H_{98} = 0.8$. It has not been demonstrated in a stable plasma discharge, yet. A first analysis of these experiments indicates that the observations seem to hold true for these conditions. Especially, the MARFE-like X-point radiation is still coupled to complete detachment of the outer target. At higher I_{P} and higher P_{H} no ELM mitigation has been observed yet and the transition to broadband fluctuations is not clearly recovered. However, a change of ELMs to small, high frequency type-III

ELMs is still observed.

An open task for the presented discharge scheme is the optimization of the discharges with respect to confinement and a more detailed analysis of the plasma performance in view of its application in future fusion reactors. Connected to this is the development of a reliable feed-back control system for the achievement and the sustainment of complete detachment with optimal core plasma parameters.

4.8 Discussion & Summary

The presented experimental H-mode detachment studies showed that the L-mode classification of detachment [1] is valid also in H-mode with the addition of a new regime with intense, very localized radiation at the X-point similar to the observations reported in Refs. [168, 206, 309]. Our experiments show that the X-point radiation and a pedestal top pressure loss are closely related to complete detachment in H-mode plasmas in AUG. Significant Balmer radiation inside the confined plasma at the X-point during complete detachment indicates $T_e \leq 5$–10 eV and significant neutral deuterium density inside the X-point. Upstream measurements of $T_{e,sep} \approx 50$–100 eV imply strong parallel temperature gradients in the confined plasma close to the separatrix that are sustained by the localized power losses due to the X-point radiation. The local radiation cooling by the X-point radiation also reduces the power flux into the divertor. Thereby, the level of recycling that can be sustained in the divertor drops along with the particle fluxes to the target plates. As a consequence the particle and heat fluxes to the targets are reduced. In addition, experimental line ratio measurements and the increased high-n Balmer line radiation at the X-point during complete detachment indicate in line with modeling in chapter 5 that volumetric recycling, e.g. local ionization and recombination, inside the X-point radiation region can be significant under such conditions.

In the approach to complete detachment an increase of the line integrated plasma density and hence the fueling efficiency is observed. This increase is accompanied by a decrease in the HFS high density and local recycling at the inner divertor baffle, indicating a shielding effect of the HFS high density for neutral fueling of the core plasma from the divertor. The reduction of the HFS high density region in spatial extent and in magnitude with nitrogen seeding is probably caused by increased radiation losses in the SOL and divertor volume that reduce the available power for ionization. The increase of the line integrated density is transient in most of our discharges. A correlation of the drop of the line integrated density to the appearance of NIII line radiation at the X-point has been observed.

A correlation of the neutral pressure measured by the HFS heatshield ionization gauges (F11) and the baratron below the inner divertor (B-Fu) implies a significant neutral conductance from the recycling region in front of the inner target to the volume behind the inner target. A possible implication for the recycling of neutrals along the inner target is that the neutrals could redistribute a significant fraction of the recycling flux into the far SOL via the subdivertor structures.

The presented experimental evidence shows that a stable operation with complete de-

tachment induced by nitrogen seeding in AUG H-modes is possible. In contrast to observations in Refs. [105,133,310], a back transition to L-mode due to an H-mode density limit was not observed. Overall, this plasma regime is very attractive for a future fusion reactor as it features almost unaffected core plasma profiles for $\varrho_{\mathrm{pol}} < 0.7$ with reduced pedestal parameters $(n_{\mathrm{e}}, T_{\mathrm{e,i}})$ and increased gradients in the region $0.7 < \varrho_{\mathrm{pol}} < 0.95$ that recover the pedestal pressure loss towards the center. The intense and stable X-point radiation reduces the power flux into the divertor. The ELM size is reduced to a level at which no clear ELM signatures at the targets can be observed and the tungsten erosion at the targets and at the main chamber is significantly lower. The reduced separatrix pressure and ELM size facilitate continuous detachment of the divertor by relaxing the upstream conditions, due to reduced $q_{\parallel}$ and reduced upstream separatrix pressure, and avoid transient reattachment. The almost unhampered core profiles with large radiation power losses inside the confined plasma are a very interesting feature of this plasma scenario. A reduced pressure at the pedestal top might be acceptable or even preferential if the core plasma parameters are unchanged and provide the same active volume that features plasma parameters necessary for fusion reactions. The extension of the experimental investigations of the presented plasma scenario to high performance discharges with higher heating power and more reactor relevant parameters delivers promising results with respect to a possible extrapolation of the observations to a reactor plasma scenario.

CHAPTER 5

Modeling

Quantitative comparison of experimental measurements in H-mode plasmas with modeling from state-of-the-art fluid codes for the SOL like SOLPS [89] regularly fail to produce satisfying agreement within errorbars. A better experimental quantification and a qualification of the deficiencies of most recent models in a direct validation with experimental data is necessary to identify missing physics in the numerical models and gain a better understanding of the physical processes involved. This chapter describes the setup and the results of 2D modeling of the H-mode detachment experiments described in the previous section with the SOLPS code. The simulations are validated against experimental data and the modeling assumptions are analyzed[1].

5.1 Codes

The SOLPS5.0 code package (Revision 4555) [89, 311] is used for numerical simulations of the SOL and divertor plasma. SOLPS mainly consists of two coupled codes: B2.5 is a fluid code that solves Braginskii-like equations for the ions (D,C,He,N) and electrons. Eirene is a Monte-Carlo code that describes kinetic neutrals [2, 312]. Both codes are coupled via source terms for particle, momentum and energy.

The SOLPS package also supplies a number of additional programs for the generation of a numerical grid from magnetic equilbria, i.e. DG and Carre, and for post-processing and visualization, i.e. B2plot. A large number of scripts for running, maintaining and post-processing of simulations is also included. During this thesis additional scripts and code were added to the SOLPS code package for maintenance of the simulations as well as for an adaptation of the physical transport model.

In order to compare the results from the numerical simulations to experimental measurements it is often necessary to use virtual diagnostics. These mimic the measurement and data evaluation process of the experimental diagnostics for a direct comparison. Simple approaches are often not possible or direct comparison would be misleading, see chapter

---

1 Part of this chapter's content has been published in [130]

3. A Python interface to the SOLPS simulation data and a number of virtual diagnostics have been developed in the framework of this thesis.

In the following, we first discuss the framework of the code and its assumptions, before validating the simulations with experimental data and finally discussing the physical implications of the results that were found. The transport description in SOLPS and its validity are discussed in the next section.

5.2 Transport

A description of the plasma state is given by the one-particle distribution functions $f_\mathrm{a}(\vec{x},\vec{v},t)$. The number of particles of species a at time t in an infinitesimal volume d^3x at $\vec{x}$ with a velocity in d^3v around $\vec{v}$ is given by $f_a(\vec{x},\vec{v},t)\,d^3x d^3v$. Using the complete distribution function is usually neither practical nor feasible. Often the moments of the distribution function are used to describe the plasma evolution in a fluid approach. This has the advantage that the moments are often available from experimental measurements. For a fluid approach, several assumptions are required and a full kinetic treatment of the SOL physics might be necessary in certain regimes or at certain locations, e.g. at the plasma-wall interface (sheath) as described in chapter 2. To extend the validity of the fluid approach, it is sometimes sufficient to include kinetic corrections and boundary conditions, e.g. heat flux limiters or sheath boundary conditions.

5.2.1 Considering the Validity of a Fluid Approach

A fluid approach is only valid if the plasma constituents are sufficiently coupled via collisions, such that the distribution function is close to a Maxwellian. The collisional coupling is given by the mean free path of self-collisions of electrons and ions [48].

$$\lambda = \lambda_\mathrm{ee} \approx Z_\mathrm{i}^4 \lambda_\mathrm{ii} \approx \frac{10^{16} T_\mathrm{e,i}^2 [\,\mathrm{eV}^2\,]}{n_\mathrm{e,i}[\,\mathrm{m}^{-3}\,]} \tag{5.1}$$

The collisionality, $\nu_\mathrm{SOL}^* = L_\mathrm{SOL}/\lambda$, gives the ratio of the characteristic scale length of the system to the collisional mean free path. The SOL scale length, L_SOL, is determined by the parallel connection length or the gradient lengths of the plasma parameters. The main prerequisite of a fluid description thus is an ordering of length scales. All characteristic length scales need to be smaller than the parallel connection length (10–100 m) or gradient scale lengths (m–cm). Typical scale lengths are the heat conduction length that is dominated by the contribution from the high energy tail particles ($\approx 5 \times \lambda_\mathrm{e,i}$), the neutral mean free path (cm–m), the electron and ion mean free path (mm–m) and the sheath length ($10\lambda_\mathrm{D}$). If the ordering is violated kinetic effects can become important.

Often, the collisionality in the SOL is not sufficiently high and, strictly speaking, the fluid description is invalid. However, detailed comparison of fluid and kinetic modeling of such plasmas showed that the fluid results often remain close to the kinetically retrieved results for the important lower order moments [48, p.402].

5.2.2 Basic Fluid Equations

In order to study plasma transport, the fluid equations [43, 313] need to be presented. The moments of the particle distribution function allow to quantitatively describe the plasma and its transport. They also can be compared to experimental results. The kinetic equation describes the evolution of the distribution function f_a in time. The external electromagnetic fields $\vec{E}$ and $\vec{B}$ impose forces on charged particles with the nuclear charge number Z_a and mass m_a.

$$\partial_t f_a + \vec{v} \cdot \vec{\nabla}_{\vec{x}} f_a + \frac{Z_a e}{m_a} \left(\vec{E} + \vec{v} \times \vec{B} \right) \cdot \vec{\nabla}_{\vec{v}} f_a = \sum_b C_{ab} \left(f_a, f_b \right) + S_a(\vec{x}, \vec{v}, t) \tag{5.2}$$

where $\partial_t \equiv \frac{\partial}{\partial t}$ and $\vec{\nabla}_i$ with $i = \{\vec{x}, \vec{v}\}$ operates on space or velocity coordinates respectively. The Coulomb interaction between plasma particles acting in velocity space is represented by the Fokker-Planck collision operator C_{ab} and $S_a(\vec{x}, \vec{v}, t)$ is a source rate [314]. Multiplying the kinetic equation of motion, (5.2), with powers of the velocity $\vec{v}$ and integrating over the velocity phase space, we arrive at the fluid equations. The particle conservation equation or continuity equation is

$$\frac{\partial n_a}{\partial t} + \vec{\nabla} \cdot (n_a \vec{u}_a) = S_a^n \tag{5.3}$$

where n_a is the particle density, $\vec{u}_a$ is the fluid velocity and S_a^n is the particle source/sink. The momentum conservation equation is

$$m_a n_a \left[\frac{\partial \vec{u}_a}{\partial t} + \left(\vec{u}_a \cdot \vec{\nabla} \right) \vec{u}_a \right] - q_a n_a \left(\vec{E} + \vec{u}_a \times \vec{B} \right) + \vec{\nabla} p_a + \vec{\nabla} \cdot \overleftrightarrow{\Pi}_a = \vec{R}_{ab} + S_a^m \tag{5.4}$$

where m_a is the particle mass, q_a is the electric charge, $\vec{E}$ is the electric field, $\vec{B}$ is the magnetic field, p_a is the pressure, $\overleftrightarrow{\Pi}_a$ is the viscosity tensor, $\vec{R}_{ab}$ is the friction force exerted on particles of type a by particles of type b and S_a^m is the momentum source/sink. The energy conservation equation is

$$\frac{\partial}{\partial t} \left[\frac{3}{2} p_a + \frac{m_a n_a}{2} u_a^2 \right] + \vec{\nabla} \cdot \left[\left(\frac{5}{2} p_a + \frac{m_a n_a}{2} u_a^2 \right) \vec{u}_a + \vec{q}_a + \vec{v}_a \otimes \overleftrightarrow{\Pi}_a \right] = Q_{ab} + Q_{\mathrm{ohm}} + S_a^e \tag{5.5}$$

where $p_a = n_a T_a$ is the static pressure, $\vec{q}_a$ is the heat flux, Q_{ohm} is the ohmic heating, Q_{ab} is the collisional energy transfer between particles of different species and S_a^e is the energy source term. The electric and magnetic fields can be obtained from Maxwell's equations with the charge density $\varrho = \sum_a Z_a e n_a$ and the current density $\vec{j} = \sum_a Z_a e n_a \vec{v}_a$ [48, p.392]. Different species a and b can be coupled via source terms S^x, where $x = \{n, m, e\}$ and electromagnetic fields.

Each fluid equation of order k includes moments of higher order $(k + 1, ...)$. In order to arrive at a complete set of equations it has to be closed by approximating higher moments. The fluid equations for the high collisionality limit are known as Braginskii equations [315]. A higher order equation scheme (21–29 moments) has been derived by Balescu in Ref. [316] and a more general formulation for collisional to weakly collisional

plasmas can be found in Ref. [317]. The exact transport equations used in SOLPS have the same structure as the presented equations. Their actual form is given in Refs. [89, 311, 313].

Due to the strong anisotropy of the particle mobility in magnetically confined plasmas a decoupling of parallel and perpendicular transport is often possible. Then the fluid equations can be solved for the parallel and the perpendicular direction separately and the perpendicular fluxes effectively constitute additional source terms in the parallel transport equations.

5.2.3 Parallel Transport

Parallel transport in the SOL is collisional and can be described by the equations (5.3)–(5.5) even though in many cases the strong requirements of a fluid description on high collisionality are not fulfilled [48]. The collisional heat flux in 1D can be described as a diffusion process by the Spitzer-Härm heat flux derived by Spitzer [318]

$$q_{\parallel,a} = n_a \chi_{\parallel,a} \vec{\nabla} T_a = -\kappa_{\parallel,a} \vec{\nabla} T_a = -\kappa_{0,a}(T_a)^{5/2} \nabla T_a \tag{5.6}$$

with the heat conduction coefficients [48, p.394]

$$
\begin{aligned}
\kappa_{0,e} &= \frac{30692}{Z_i \ln \Lambda} \approx 2000 \ \left[\frac{W}{m \ eV^{7/2}} \right] \\
\kappa_{0,i} &= \frac{1249}{Z_i^4 m_i^{1/2} \ln \Lambda} \approx 60 \ \left[\frac{W}{m \ eV^{7/2}} \right]
\end{aligned}
\tag{5.7}
$$

where $T_{e/i}$ is given in eV and $q_{e/i}$ is given in Wm^{-2}. The numerical values are given for a pure deuterium plasma ($m_i = Z_i = 1$, $\ln \Lambda = 15$). In the parallel direction most of the conducted heat flux is carried by the electrons, because of their larger heat conduction coefficient. The heat flux in (5.6) has no limit with increasing temperature gradients. In reality, the heat flux is limited by the (kinetic) free-streaming of particles, $q_{lim} = \alpha_{lim} n v_{th} T$, where α_{lim} is the heat flux limit fraction. In SOLPS this limit is included by so-called flux limiters.

$$\hat{q}_{\parallel}^{-1} = \left(q_{lim}^{-1} + q_{\parallel}^{-1} \right)^{-1} \tag{5.8}$$

The correct values for α_{lim} must be determined by direct comparison of kinetic and fluid simulations and are still discussed [48, 319]. Typical values in SOLPS modeling are for the electron heat flux limiter $\alpha_{lim,e} = 0.2$ and for the ion heat flux limiter $\alpha_{lim,i} = 0.6$–1.5. The impact of flux limiters is expected to be larger for ions [101].

Another potentially important kinetic effect is the presence of a suprathermal electron population. Especially in the divertor [320], even small fractions of suprathermal electrons can enhance the thermal conductivity [321] and the radiation potential [322] significantly and can invalidate a local transport description [323]. The effects of suprathermal electrons are not included in SOLPS so far.

5.2.4 Perpendicular Transport

A generic description of perpendicular transport, often identified with radial transport, is a convective-diffusive ansatz for the flux. Using a diffusion coefficient D and a convective velocity v this reads in 1D

$$\Gamma(x) = -D(x)\frac{\mathrm{d}n}{\mathrm{d}x} + v(x)n(x) \tag{5.9}$$

For SOLPS the actual perpendicular flux is decisive and it is common practice to simplify (5.9) further to a pure diffusion equation with an effective diffusion coefficient D_{eff} such that the same flux is obtained.

$$\Gamma(x) = -D_{\mathrm{eff}}(x)\frac{\mathrm{d}n}{\mathrm{d}x} \tag{5.10}$$

The use of (5.10) in SOLPS simulations does not imply that the underlying physical transport is diffusive in nature. However, transport derived from (5.10) is numerically more stable. For source-free regions, e.g. the deep plasma core, (5.10) will always result in flat radial steady-state profiles. A perpendicular gradient requires $v/D \neq 0$ [34]. This can be included in SOLPS if necessary.

The physical reasons for perpendicular transport and hence the perpendicular transport coefficients in (5.9) is subject of this section. A similar scheme is also applied to energy transport with $n \rightarrow T$, $D_{\mathrm{eff}} \rightarrow n\chi_{\mathrm{eff}}$ and $\Gamma \rightarrow q$ taking into account that particle transport has heat transport coupled to it.

Classical transport is caused by perpendicular friction forces. Classical transport coefficients are derived in Refs. [44, 324] and typical values in tokamaks are $D^a_{\mathrm{CL}} \approx \chi^a_{\mathrm{CL}} \approx 10^{-5}$–$10^{-4}$ m^{2}s^{-1}. For closed field lines neoclassical transport includes toroidicity effects. Neoclassical transport coefficients resemble the classical results, but are enhanced by a geometrical factor [316, 325, 326]. Typical values in tokamaks are $D_{\mathrm{neo}} \approx \chi_{\mathrm{neo}} \approx 10^{-3}$–$10^{-1}$ m^{2}s^{-1}. Neoclassical transport also introduces additional effects, e.g. mirror forces, curvature and ∇B drifts [316, 324].

However, collisional transport is not able to explain the perpendicular transport coefficients derived from experimental measurements. The measured transport coefficients are of the order of $10D \approx \chi \approx 1$–$10$ m^{2}s^{-1} [29, 48, 327], which is orders of magnitude larger than predicted by collisional transport theory. The transport is labeled anomalous and is of turbulent nature. It remains a field of active research [303, 328–331]. Of particular importance for fluid simulations is that it has not yet been possible to parameterize the anomalous transport in the standard diffusive and convective ansatz [332, 333]. The perpendicular transport coefficients in SOLPS simulations are therefore ad hoc. An overview of tokamak transport processes, including turbulent transport, can be found in [58].

Density and potential fluctuations are routinely measured in fusion plasmas. Fluctuations induce turbulent transport in the confined plasma and intermittent transport in the SOL [329, 331, 334–337]. A major fraction of the intermittent transport in the SOL is carried by filaments of increased density and temperature that are elongated along the

magnetic field lines, so called blobs [334]. The blob is polarized due to curvature drifts and the electric field leads to a radially outward-directed propagation. Experimentally, filamentary transport in the SOL due to blobs has been observed across a variety of machines [303, 304, 328, 330, 338–343]. A main chamber wall recycling regime [327], and mechanisms for a fueling and the density limit [103, 339] have been attributed to increased perpendicular transport due to blobs. The intermittency of the transport along with the localized increase of density and temperatures inside the blob filaments can have a major impact on the assumption of a fluid model in the SOL. The interaction of the background plasma with kinetic neutrals as well as the the transport description of the background plasma can change [344].

In the divertor, filamentary transport and blobs have been experimentally observed as well [345]. First MHD analysis suggests the existence of divertor instabilities [346] that might cause such filaments and would increase the perpendicular transport in the divertor.

In H-mode plasmas, ELMs also significantly alter the transport during their occurrence. The intense pulses of energy and particles into the SOL as well as the filamentary structure of the ejected plasma leads to different transport compared to inter-ELM time intervals. This thesis concentrates on small ELM regimes or on inter-ELM periods to avoid additional complication of transport effects due to ELMs. However, ELMs might affect the inter-ELM plasma nonetheless, e.g. by increased impurity content due to sputtering during ELMs and by a redistribution of the impurities away from an inter-ELM steady state solution. The impact of ELMs on the presented SOLPS simulations has been tested with a mock-up ELM model for diffusive and convective ELMs [347]. No detrimental impact of the ELMs on the inter-ELM simulation has been found. In particular, the impurity concentration in the confined plasma was not affected.

5.2.5 Poloidal Variation of Perpendicular Transport

Experimental transport coefficients are mostly given as one-dimensional quantities [339]. However, poloidal variations of the perpendicular transport coefficients are expected to arise due to several effects such as magnetic geometry or drifts. Ballooning of transport [50, 89, 230, 348] describes the experimental observation that the perpendicular transport of power and particles into the SOL across the separatrix is the largest close to the outer midplane, where also the fluctuation level is the highest [304, 349]. The reason for the enhanced transport is a reduced MHD stability at the outboard midplane [42]. The ballooning nature of transport is described in SOLPS by a ballooning factor $c \times (B_{t,ref}/B_t)^\alpha$, where B_t is the local toroidal field, $B_{t,ref} \approx 2.82$ T is the toroidal field average across the whole simulation domain, c and α are free parameters. In the standard ballooning scheme the rescaling applies to the whole simulation domain. A scheme with ballooning only on closed field line has been introduced in SOLPS to avoid a reduction of the transport in the inner divertor.

As introduced above, divertor MHD-modes have been found [346], that could lead to an increased perpendicular transport in the divertor volume close to the target. Experimental observations of filaments in the inner private flux region and in the outer divertor

of the MAST tokamak might also indicate an increased radial transport in the divertor region due to filamentary transport [345]. The analysis of snowflake divertor configurations yielded a possibly enhanced transport in the X-point region due to low β_p [132]. As will be shown later, such an increase of transport in the divertor region is necessary in the simulations in order to match the experimental target profiles. The SOLPS code was accordingly adapted to allow for such a local variation of the transport coefficients in the divertor and/or at the X-point.

Additional plasma transport will arise in the plasma due to plasma flows and drifts.

5.2.6 Drifts

The gyro-motion of charged particles in a magnetic field leads to a separation of the parallel and the perpendicular dynamics of particle transport. The particle motion can be described in the guiding center approach [44], in which the gyration is averaged and the center of the gyro orbit becomes the new effective particle coordinate. The presence of gradients, perpendicular electromagnetic fields or time-varying electromagnetic fields can lead to a drift perpendicular to the magnetic field. In the fluid picture these single particle drifts are translated into a drift velocity of the fluid [42, 113].

The investigation of drifts and their complex interplay with the plasma evolution is a longstanding field of research [89, 167, 241, 350–352]. Self-consistent simulations including drift effect can shed light on the impact of drifts on the plasma evolution and on power exhaust by facilitating or inhibiting detachment. However, the analysis of the effect of drifts is very challenging [101, 113] as the interaction with the plasma is complex and non-linear. Missing physical effects in the numerical model might completely mask drift effects that would otherwise be utterly important. Numerical simulations that include drift effects are still not able to fully reproduce the asymmetric behavior that is observed in experiment, e.g. in the approach to detachment [130, 166, 167]. However, it has been shown that drifts contribute to the power and particle asymmetries observed in divertors [113, 167, 353, 354]. Analysis of drifts in this thesis will show that they significantly influence the distribution of the density, the radiation and the detachment fronts in the divertor and their stability.

The particle and power redistribution due to drifts will lead to return flows in the SOL and can lead to induced currents (thermo currents and Pfirsch-Schlüter currents). These flows and currents add to the "pure" drift transport. Flows and currents are not discussed in detail here and the reader is referred to [113, 354, 354–358]. In the presented simulations the flow pattern in the SOL and the divertor is changed and flow reversal in the divertor is reduced or suppressed.

Diamagnetic Drift ($\vec{B} \times \vec{\nabla} p$)
The combined, single-particle guiding center drift due to a gradient in the magnetic field, $\vec{\nabla} B$, and the curvature, κ, of the magnetic field is described by the drift velocity [29]

$$\vec{v}_{\vec{\nabla}\vec{B}+\vec{\kappa}_\mathrm{c}} = \frac{m}{2qB}\left(2v_\parallel^2 + v_\perp^2\right)\frac{\vec{R}_\mathrm{c} \times \vec{B}}{R_\mathrm{c}^2 B} \tag{5.11}$$

where R_c is the radius of curvature, q is the electric charge, $v_\perp$ and $v_\parallel$ are the perpendicular and parallel velocity respectively. Unlike the $\vec{E} \times \vec{B}$-drift, the $\vec{\nabla}\vec{B}$- and curvature drifts are charge dependent. For a toroidal field in clockwise direction in a top-down view the ion $\vec{\nabla}\vec{B}$ velocity points downward into the lower divertor. This magnetic field configuration is called forward field. For reversed field the toroidal field is in counterclockwise direction and the ion $\vec{\nabla}\vec{B}$ velocity points upward out of the lower divertor.

The diamagnetic drift is no single-particle drift, but a fluid effect that results from fluid averaging of the ∇B and curvature drifts with a background pressure gradient. In a fluid approach it replaces the guiding-center $\vec{\nabla}B$ and curvature drifts of the single particle motion.

$$\vec{v}_{\text{dia}} = \frac{\vec{B} \times \vec{\nabla}p}{qnB^2} \tag{5.12}$$

This drift is divergence free when combined with the Pfirsch-Schlüter flows [113, 359]. A more detailed analysis of the diamagnetic drift on in/out asymmetries in the divertor can be found in Ref. [354].

$\vec{E} \times \vec{B}$-Drift

The guiding center particle drift due to a static electric field, $\vec{E}$, is described by the drift velocity

$$\vec{v}_{\tilde{E}\times\tilde{B}} = \frac{\vec{E} \times \vec{B}}{B^2} \tag{5.13}$$

Poloidal $\vec{E} \times \vec{B}$-drifts are driven by a radial electric field, which is a consequence of the radial temperature gradients. Assuming a grounded vessel wall ($V = 0$), the plasma potential can be approximated by $3T_e(r)$ due to the sheath potential drop. The radial electric field then is

$$E_r = -\frac{dV}{dr} \approx \frac{3T_e}{e\lambda_{T_e}} \tag{5.14}$$

Figure 5.1: The poloidal (a) and radial (b) fluxes for high recycling target conditions due to $\vec{E} \times \vec{B}$-drifts are shown in red. The corresponding electric field is shown in blue [102].

where λ_{T_e} is the temperature fall off length in the SOL. The poloidal flux from the $\vec{E} \times \vec{B}$ drift can be approximated by

$$\Gamma_\theta \approx \frac{E_r n_e}{B} \tag{5.15}$$

For forward field and in high recycling the particle flux induced by the radial electric field is shown in figure 5.1.a. It is directed from the inner towards the outer divertor in the SOL and vice versa in the private flux region. This drift contributes to the experimentally observed pressure and power flux in/out asymmetries of the divertor [353]. For detached
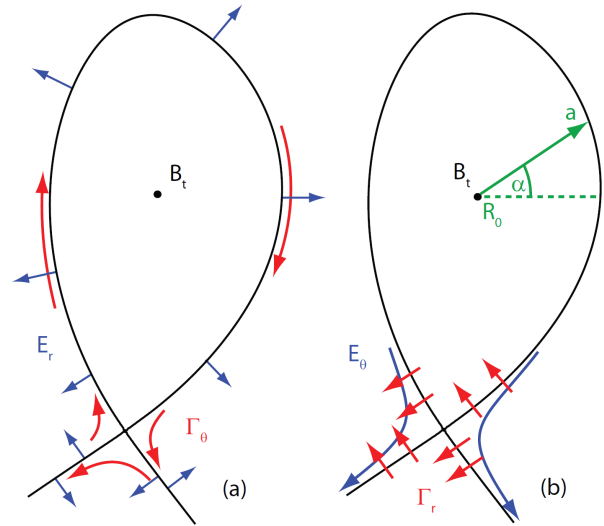
divertor targets the direction of the drift can change as detached temperature profiles tend to be strongly reduced close to the separatrix and the radial temperature gradient can reverse sign.

Radial $\vec{E} \times \vec{B}$-drifts are driven by a poloidal electric field. A parallel electric field arises due to parallel temperature and pressure gradients. Neglecting parallel currents, the poloidal component of the parallel electric field can be expressed as [353]

$$E_\theta = - \left(\frac{0.71}{e} \nabla_\parallel T + \frac{1}{en_\mathrm{e}} \nabla_\parallel p_\mathrm{e} \right) \frac{B_\theta}{B} \tag{5.16}$$

In the simplest case of a sheath-limited SOL a minimum static pressure drop from upstream to the target of a factor of 2, due to the acceleration of the plasma to sound speed, is a lower limit for E_θ. For high-recycling significant parallel temperature gradients and for detachment additional volumetric pressure loss along the parallel direction will occur. For a uniform temperature gradient from the midplane to the target along the whole connection length, L_c, and with a parameterization of the parallel pressure profile by $p_\mathrm{e} = p_\mathrm{e,u}(T_\mathrm{e}/T_\mathrm{e,u})^\alpha$, a radial flux can be estimated [353]

$$\Gamma_\mathrm{r} = \frac{E_\theta n_\mathrm{e}}{B} \approx (0.71 + \alpha) \frac{n_\mathrm{e} B_\theta (T_\mathrm{e,u} - T_\mathrm{e,t})}{B^2 e L_\mathrm{c}} \tag{5.17}$$

Radial $\vec{E} \times \vec{B}$ fluxes are considered as a contributer to the in/out asymmetries in numerical simulations. As shown in figure 5.1.b they transport particles through the private flux region from the outer to the inner divertor. The particle flux from the higher power/pressure outer divertor to the inner divertor could induce earlier detachment at the inner divertor by increased density and radiation [241]. Drift induced particle and power fluxes at the X-point could play a role in the stabilization of the X-point radiation that is described later. In contrast to the poloidal $\vec{E} \times \vec{B}$, the direction of the radial fluxes remains the same in high recycling and detached conditions as the poloidal temperature and pressure gradients always point from downstream to upstream. The poloidal location of the gradient region changes with progressing detachment from close to the targets to close to the X-point. A variation of the magnitude of the flux with detachment depends on the length across which the temperature and pressure drop occurs and on the alignment of this gradient region with the region of high density. The former tends to decrease significantly in discharges with strong radiation cooling by nitrogen in the divertor. The temperatures for efficient nitrogen radiation and deuterium ionization are similar. It is to be expected, that the high densities of the ionization region is well collocated with the gradient region due to radiation cooling.

For more details on the theoretical analysis of drifts, a number of extensive introductory textbooks for (neo)classical plasma transport theory have been written [42,44,316,360].

Despite the possible importance of drifts, their effects have been excluded in many previous numerical studies of fusion plasmas. The SOLPS code is able to account for the transport due to drifts, but numerical instabilities and problems with the formulation of the transport equations and boundary conditions can arise. Such simulations require small time steps that increase the time to achieve converged plasma solutions by a factor of 100. The long convergence time and a necessary intense maintenance of such

simulations in transient phases until a converged solution is obtained remain a challenge. Converged drift simulations that include seed impurities and are validated with experimental data have been developed on a timescale of two years in the course of this thesis.

5.2.7 Neutral Transport

The neutral transport description in the Monte-Carlo code Eirene is kinetic. The Fokker-Planck equation is solved with a Monte-Carlo approach using a track-length estimator [2,361]. The inclusion of volume reactions, e.g. collisions or ionization, is straightforward in a Monte-Carlo approach and the set of reactions for neutral-plasma interaction can be easily adapted. The interactions of the neutrals with the plasma are given in table 5.1 and table 5.2. Optional reactions given in these tables were included to perform sensitivity studies. More on the details of the neutral transport model of Eirene can be found in Ref. [2] and references therein.

5.3 Atomic Physics Model

The atomic physics model determines the interaction of the plasma constituents. The emission of electromagnetic radiation and the interaction with neutrals is of particular importance for power dispersal and momentum losses in the SOL and the divertor. In a plasma there are two main volumetric reaction types of importance for SOLPS modeling. One does not change the type of particle and is inherently described by the collision operator in (5.2), e.g. thermalization. The other transforms particles of one species into another one and can be included as source and sink terms in the fluid equations for different species, e.g. electron-impact ionization. This section focuses on the latter.

Electron Impact Ionization & Electron Impact Excitation

$$A^z + e^- \rightarrow A^{z+1} + 2e^- \quad \& \quad A^z + e^- \rightarrow A^{z*} + e^- \tag{5.18}$$
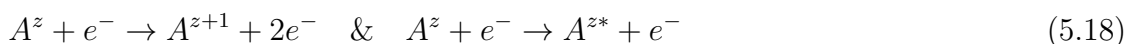
Inelastic collisions of ions or neutrals with an electron can either ionize or excite the particle. The first process determines the source rate for the ions in a fluid plasma description. The second changes the population distribution of the excited states of a particle. As a consequence line emission and increased, step-ladder like ionization occurs. If the lifetime of the excited state, τ, is lower then the residence time, τ_{res}, in the discretization volume of a simulation, the ensemble of ground and excited states of a particle can be represented by a single quasi particle. The reaction rates are then modified accordingly to effective, local rates that are derived from a collisional radiative model [90, 137, 362]. If $\tau_{\mathrm{res}} < \tau$ it can become necessary to treat (meta)stable states as separate species in the transport simulation.

Charge Exchange

$$A^z + B^{z+1} \rightarrow A^{z+1} + B^{z(*)} \tag{5.19}$$

In a charge exchange collision two particles exchange a valence electron. Resonant charge exchange occurs if similar energy levels exist for the valence electron in both particles. Charge exchange reactions produce a typical charge exchange excitation spectrum of the secondary ion, which is used for charge exchange recombination spectroscopy as a diagnostic tool, see chapter 3. Charge exchange is also a loss channel for plasma pressure via momentum losses, see section 2.2.

Three Body Recombination & Radiative Recombination

$$A^{z+1} + e^- + e^- \rightarrow A^z + e^- \quad \& \quad A^{z+1} + e^- \rightarrow A^z + h\nu \tag{5.20}$$
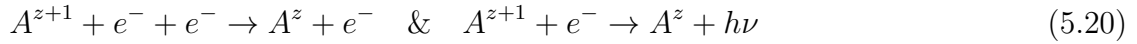
Recombination is a sink term for ions, plasma energy and momentum and a source term for the electron energy at low T_e (recombination electron heating [363]). Recombination is an important process to reach complete detachment and a significant particle flux reduction at the target, see section 2.3.

Molecular Reactions

Molecular physics, especially with deuterium molecules [229], can be important in a divertor plasma, where the recycling flux dominates [364, 365] the particle source term and the fraction of molecules in the neutral deuterium flux can be large [279, 366–368]. Numerical modeling showed that molecular assisted reactions can be important at low divertor temperatures [367], but simulations of TCV and AUG with divertor Div-I implied that the molecular assisted reactions are not dominant for open divertor tokamaks [101, 369, 370].

The simulations in this thesis showed that the dominant momentum loss in the divertor is due to elastic and charge exchange collisions of D with D_2. In collaboration with D. Reiter from Forschungszentrum Jülich a simple N_2 breakup model based on Ref. [371] was included into the Eirene database during this thesis, see table 5.2. Initial modeling

Idx	Reaction	Eirene Label	Type
	Default		
1	$D + e^- \rightarrow D^+$	AMJUEL H.4/10 2.1.5	Ionization
2	$D^+ + e^- \rightarrow D$	AMJUEL H4/10 2.1.8	Recombination[1]
3	$D + D^+ \rightarrow D^+ + D$	AMJUEL H1/3 3.1.8	Charge exchange
4	$D_2 + e^- \rightarrow D_2^+$	AMJUEL H4 2.2.9	Ionization
5	$D_2 + e^- \rightarrow 2D$	AMJUEL H.4 2.2.5g	Dissociation
6	$D_2 + e^- \rightarrow D^+ + D$	AMJUEL H.4 2.2.10	Ionizing dissociation
7	$D_2 + D^+ \rightarrow D_2^+ + D$	AMJUEL H.3 3.2.3	Charge exchange
8	$D_2^+ + e^- \rightarrow 2D^+$	AMJUEL H.4 2.2.11	Ionizing dissociation
9	$D_2^+ + e^- \rightarrow D^+ + D$	AMJUEL H.4 2.2.12	Dissociation
10	$D_2^+ + e^- \rightarrow 2D$	AMJUEL H.4 2.2.14	Recombining dissociation
	Optional		
11	$D + D^+ \rightarrow D + D^+$	AMJUEL H.0-3 0.1T	(In)Elastic collision
12	$D_2 + D^+ \rightarrow D_2 + D^+$	AMJUEL H.0-3 0.3T	Elastic collision

[1] Including radiative and three-body recombination.

Table 5.1: Deuterium neutral reactions included in Eirene.

that includes the nitrogen molecule break-up model indicates only a minor influence of the nitrogen molecules on the overall plasma solution in the presented plasma scenarios, see section 5.10.

Spontaneous Emission & Photon Absorption

$$A^{z*} \to A^z + h\nu \quad \& \quad A^z + h\nu \to A^{z*} \tag{5.21}$$

Spontaneous emission of a photon is a deexcitation process of an excited atom. The radiation is called line emission and can only be generated by particles that are not fully stripped of its electrons. The line emission rate of a plasma can be deduced from photon emission coefficients from the ADAS database. Such effective rates for photon emission of specific transitions or the non-coronal total radiation cooling rate, L_Z^{nc}, are used for modeling radiation energy losses. Line emission intensities can also be reconstructed with them using a virtual diagnostic for comparison with experimental spectroscopy measurements.

The reverse process of photon absorption occurs if the mean free path of a photon is smaller than the size of the considered system. If photon absorption occurs the plasma is called opaque to photons of that specific wavelength. Opacity for Lyman line radiation has been observed in the divertor of C-Mod [126], AUG [370] and JET [141]. For opaque plasmas the photon transport must be included in numerical models. The rate coefficients of collision radiative models can change significantly when photon reabsorption is accounted for Refs. [221, 232, 372, 373]. This could be particularly important for the in-

Idx	Reaction	Eirene Label	Type
		Default	
13	$N + e^- \to N^+$	AMJUEL H.4/10 2.7A0	Ionization
15	$N^+ + e^- \to N$	AMJUEL H.4/10 2.3.7A0	Recombination[1]
21	$C + e^- \to C^+$	AMJUEL H.2/10 2.6A0	Ionization
23	$C^+ + e^- \to C$	AMJUEL H.4/10 2.3.6A0	Recombination[1]
22	$C + D^+ \to C^+ + D$	METHANE H.3 3.3.2	Charge exchange
24	$He + e^- \to He^+$	AMJUEL H.4/10 2.3.9a	Ionization
27	$He^+ + e^- \to He$	AMJUEL H.4/10 2.3.13a	Recombination[1]
26	$He + D^+ \to He + D^+$	AMJUEL H.0-3 0.2T	Elastic collision
25	$He + D^+ \to He^+ + D$	AMJUEL H.3/9 3.3.1	Charge exchange
		Optional	
14	$N + D^+ \to N^+ + D$	METHANE H.3 3.3.2	Charge exchange[2]
16	$N_2 + e^- \to 2N$	AMJUEL H.2 2.7.5	Dissociation
17	$N_2 + e^- \to N_2^+$	AMJUEL H.2 2.7.9	Ionization
18	$N_2 + e^- \to N + N^+$	AMJUEL H.2 2.7.10	Ionizing dissociation
19	$N_2^+ + e^- \to 2N^+$	AMJUEL H.2 2.7.11	Ionizing dissociation
20	$N_2^+ + e^- \to N + N^+$	AMJUEL H.2 2.7.12	Dissociation
28	$He + He^+ \to He^+ + He$	HYDHEL H.1 5.3.1	Charge exchange
29	$He + He^{2+} \to He^{2+} + He$	HYDHEL H.1 6.3.2	Charge exchange

[1] Including radiative and three-body recombination. [2] Mock up model using carbon data.

Table 5.2: Impurity neutral reactions included in Eirene.

tense X-point radiation of nitrogen in the presented H-mode detachment experiments.

More detailed information about molecular and atomic reactions used in this work can be found in Ref. [364, 374–376]. A general review on ionization data and numerical methods can be found in Ref. [90]. A short description of impurity light emission and ionization is contained in [377]. The rate coefficients used in the framework of this thesis are taken from the Atomic Database in Applied Science, ADAS [137]. The accuracy of the data is mostly considered to be about $10 - 20$ %.

SOLPS Reactions

The neutral-plasma reactions that are included in the presented SOLPS calculations are summarized for deuterium in table 5.1 and for impurities in table 5.2. The optional reactions have been employed in sensitivity studies. For ion species particle-plasma reactions calculated by B2.5 include ionization and recombination from the ADAS [137] database. Radiation losses are derived from ADAS cooling rates that include bremsstrahlung for ions. Eirene calculates the neutral radiation and the electron cooling rate from neutrals. A simple break up model for N_2, as discussed in [378], was included into the atomic database of EIRENE (Amjuel) with help from D. Reiter from Forschungszentrum Jülich during this thesis.

5.4 Plasma-Wall Interaction

With the transport and volume reactions covered, the missing part for SOL simulations is the interaction of the plasma with the material surfaces at the main chamber wall and especially at the divertor target. As discussed in chapter 2 particles that impact on a surface will first pass through the sheath, where ions are accelerated by its potential drop. The particles then impact on the target surface and interact with the solid material in various ways depending on the impact angle, energy and the particle-solid material combination [379]. The most important interaction mechanisms are recycling and sputtering.

Recycling: Reflection, Release & Absorption

Particle fluxes to the divertor targets are generally large (10^{23} m^{-2}s^{-1}), especially in the high recycling regime. The recycling flux often constitutes the dominant particle source for the plasma and the integrated recycling flux is larger than the externally applied gas puff. Inert gases, like helium and neon, are fully recycling with a recycling coefficient $R = \Gamma_t/\Gamma_{recyc} = 1$, where Γ_t is the particle flux to the target and Γ_{recyc} is the recycling flux. For deuterium and nitrogen strictly speaking the recycling coefficient is $R < 1$, because they will be adsorbed at the surface and can be implanted into the bulk material. Material surfaces tend to saturate after a sufficient fluence. A dynamic equilibrium is reached such that the recycling coefficient becomes $R \approx 1$. For deuterium and clean PFC materials the fluencies necessary for saturation are achieved within 1–10 ms at the divertor targets and 1–10 s at the main chamber wall for typical H-mode conditions. For nitrogen, TRIDYN [380] calculations have shown that implantation of nitrogen in tungsten saturates for fluencies of 10^{23} m^{-2} [381]. In high recycling conditions the divertor targets then saturate within 1 s for typical H-mode conditions. The main chamber wall and remote surfaces

most probably saturate on significantly longer timescales and can exhibit a pumping characteristic with $R < 1$. For saturated walls the particle recycling is described in SOLPS with a two component model: a fast reflection of ions as neutral atoms and a thermal release of molecules/atoms for ion impact energies below a threshold E_{cut}. In the presented SOLPS simulations the default is $E_{\text{cut}} = 5$ eV. The correct physical value is an open question. TRIM calculations suggest that a value of 5–10 eV is reasonable for deuterium.

A fast particle reflection model was developed based on data from the Monte-Carlo code TRIM, that is based on a kinetic simulation of a collision cascade inside the material with the binary collision approximation [382, 383]. Obtained particle reflection coefficients for hydrogen and helium on tungsten and carbon targets are shown in figure 5.3. However, the binary collision approximation of the TRIM code gradually breaks down below 50–100 eV [384]. Comparison of the TRIM data, depicted in figure 5.3, to molecular dynamics simulations, shown in figure 5.2, indicate that even at very low impact energies the fraction of 'fast' reflected particles might be appreciable (70 %).

Figure 5.2: Reflection coefficient for deuterium on tungsten calculated with TRIM and molecular dynamics simulations.

The thermal reflection model mimics all processes that first absorb the particle in the volume, e.g. implantation, or adsorb it at the surface. After a sufficient residence time, e.g. due to bulk diffusion, the deuterium will eventually be adsorbed on the surface, recombine and thermally desorb as a neutral atom or molecule. For fully recycling species impinging on a saturated target material in steady-state, the flux of thermally desorbed particles equals the influx of particles that are not reflected directly as fast particle. The angular distribution of the particle velocity with respect to the target surface normal and the energy distribution is not well determined experimentally. In SOLPS simulations, usually, a cos or $\cos^2$ angular distribution centered around the surface normal is assumed for the velocity and a Maxwellian energy distribution with the surface temperature or
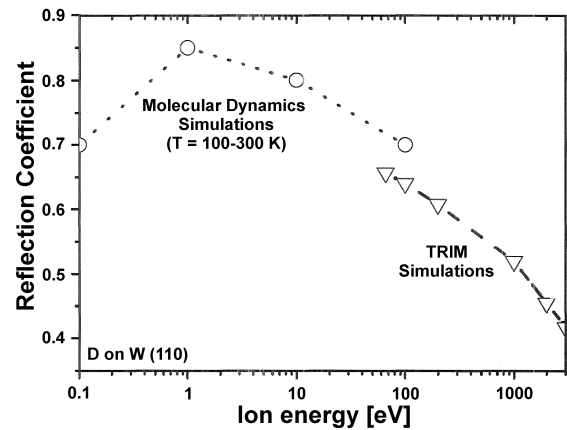

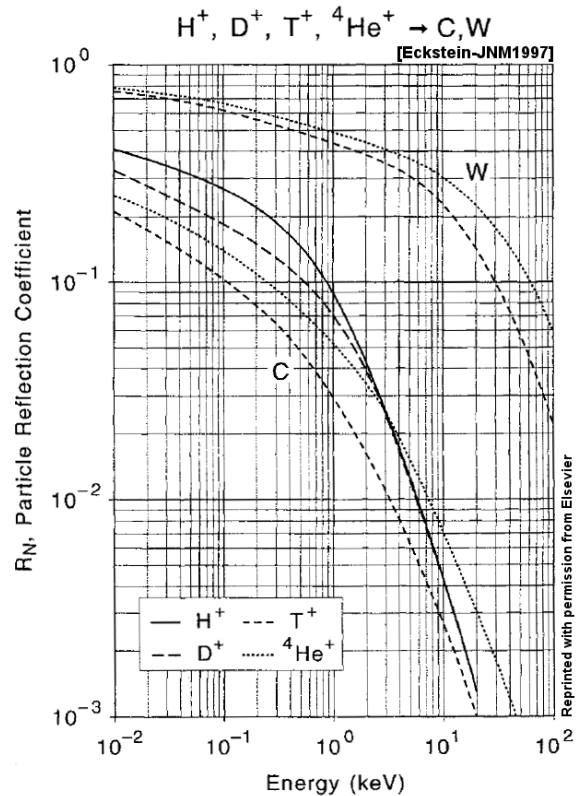**Figure 5.3:** Reflection coefficient for main fuel species on tungsten and carbon [382].

a monoenergetic source with $E_{kin} = T_{surf}$ is
assumed.

Non-recycling ($R < 1$) or sticking ($R \approx 0$) impurity ions also exist. Carbon for example can be considered as a sticking impurity for practical matters and in simulations. This is included in the simulations by absorption of a fraction $1 - R$ of the impinging flux at the surface. With carbon the additional complexity of layer formation and deuterium co-deposition arises. Carbon-layers and surface chemistry, e.g. carbon hydrate formation, can lead to a more complex recycling, that involves plasma chemistry and complex molecule break-up models [369]. Co-deposition on carbon targets or even carbon layers on tungsten targets can efficiently result in $R < 1$ for deuterium [81, 385] and in carbon-like wall properties, that will change the reflection probability of particles, the amount and distribution of recycled energy substantially. The same is true for the frequently used boron impurity in AUG (boronization).

To assess the effect of remaining carbon sources and the formation of boron and carbon layers at the cold inner target, a change of the wall material of the inner target from tungsten to carbon has been performed in the SOLPS simulations. In high recycling the change increases the neutral pressure in the divertor by 20 % and increases the peak density at the inner target by 40 %. For detached cases the reduction in peak pressure at the inner target can be up to a factor of 2. Additional carbon sources by sputtering were neglected in these simulations. This finding alludes to the fact that it is necessary to use accurate particle and energy reflection coefficients at low ion impact energies for which the validity of the binary collision approximation in TRIM gradually breaks down [384]. Experimentally benchmarked, more sophisticated molecular dynamics calculations should supplement these data.

Sputtering & Self-Sputtering

Sputtering is a source of intrinsic impurities in fusion plasmas and can be a major concern for plasma performance or erosion of PFCs. Sputtering occurs when plasma particles impinge on a material surface with sufficient energy such that particles from the surface or bulk material can overcome their bulk and/or surface binding energy after a collision. There are two sputtering mechanisms: First, physical sputtering due to energy and momentum transfer in collisions. Second, chemical sputtering is the physical sputtering or the thermal release of previously formed chemical compounds. The formed compounds can be volatile or weakly bound and thereby significantly enhance the erosion yield compared to physical sputtering. Also the threshold energy for sputtering to occur can be significantly reduced. Chemical sputtering is very important for hydrogen impacting on carbon surfaces. Although AUG is a full tungsten device and chemical sputtering is not a major issue, carbon layers can be formed at the cold inner divertor target of AUG [81, 386].

The physical sputtering yield is set by the energy transfer factor $\gamma = \frac{4m_1 m_2}{(m_1 + m_2)^2}$, where m_1 and m_2 are the projectile and target material atomic masses respectively. The energy transfer factor and the surface binding energy determines the sputtering threshold energy E_{th}, below which no sputtering occurs. With strict limits for allowable tungsten concentration in the core plasma, see section 4.5.2, and maximum allowed erosion rates in ITER and DEMO [92] sputtering is an important process. Adding seed impurities

has two effects on the overall wall material erosion: First, sputtering will be increased compared to deuterium due to larger γ values and larger sheath acceleration of impurity ions ($Z > 1$). Second, low-Z impurities like nitrogen can efficiently cool the divertor plasma due to increased line radiation. If the temperature drops below the threshold temperature ($\Delta E_{\mathrm{kin}}(T_{e,\mathrm{th}}) = E_{\mathrm{th}}$) sputtering will be suppressed, see figure 4.9. A more detailed introduction to sputtering can be found in Ref. [2, 71].

In H-mode the presence of ELMs changes the transport, the recycling and the erosion of wall material. High target temperatures and large particle fluxes during the ELM can enhance sputtering significantly. For low divertor target temperatures in between ELMS (high recycling) sputtering during ELMs is the dominant divertor tungsten source in AUG [75]. This can in turn also change the inter-ELM plasma significantly, e.g. by radiation cooling due to ELM-produced impurities. Tungsten sputtering is not included in our simulations, because the inclusion of tungsten in the simulations requires significantly more computational time and because the dominant tungsten source due to ELMs is not included in our simulations that concentrates on time intervals in between ELMs. The dominant effect of tungsten as a source of core radiation is effectively taken into account by adjusting the power into the simulation domain accordingly.

Physical and chemical carbon sputtering at the inner carbon target was included in the target material study simulations discussed in the previous paragraph to test the sensitivity of the simulated results to a possible additional carbon source at the inner target and hence to additional radiation cooling at lower electron temperatures, see figure 1.6. The carbon source by chemical sputtering is set to 0.5 % of the incoming flux. This results in almost identical conditions for close to detached cases due to the low fluxes and low temperatures at the inner target. The carbon in the inner divertor leads to an increase of the neutral density in the inner divertor on the expense of the neutral density in the outer divertor. This leads to a counterintuitive slight increase of the outer divertor target temperature and to a decrease of the total radiation by about 10 %.

Boundary Conditions

The structure of the simulation domain in real space (a) and the numerical grid regions (b) of a SOLPS simulation for single null plasmas are shown in figure 5.4. The numerical grid is divided into six distinct regions: The core, the SOL, inner and outer divertor SOL and inner and outer divertor private flux region. At the edge of the simulation domain boundary conditions need to be applied that effectively emulate the interaction with the targets and the PFC materials. This paragraph presents the applied boundary conditions in the SOLPS simulations and briefly discusses the sensitivity of
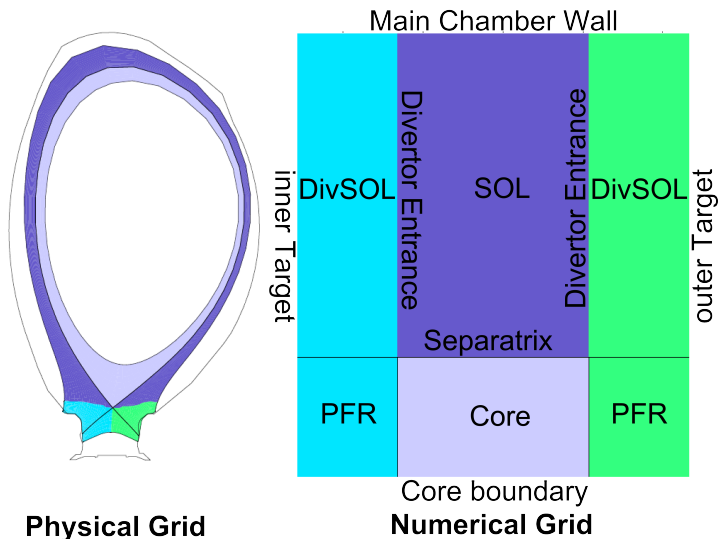

Figure 5.4: Four different SOLPS grid regions with mapping to the numerical grid [311].

the presented solutions to them. There are three types of boundaries at the edge of the SOLPS simulation domain: First, the main chamber and private flux region boundaries are aligned with the magnetic field lines. Fluxes to these boundaries are due to perpendicular transport. The power flux is absorbed and the particles recycle as neutrals at these boundaries. The perpendicular width of the SOL domain must be made large enough to accommodate at least several perpendicular decay lengths of the parallel power and particle fluxes to ensure that the radial boundary condition at the SOL edge will not influence the parallel dynamics. Second, the core boundary is also aligned with the magnetic field lines, but the heat and particle fluxes across this boundary have to include the power due to central heating of the plasma and ionization of particles in the core plasma respectively. Third, the target boundaries are subject to parallel fluxes of particles and energy.

The applied particle boundary condition at the target is that all particles recycle ($R = 1$) for all species but carbon. Carbon is sticking and does not recycle in the simulations ($R = 0$). The velocity and energy distribution of recycled neutrals is determined by Eirene as discussed above. At the core boundary ions and neutrals "recycle" as ions that are fully stripped of their electrons. An additional particle flux is added at the core boundary that accounts for the particle source due to the neutral beam heating. The particle flux is derived from the deposited beam power and the acceleration voltage applied in the neutral beam source. All particles are assumed to be of the first, full energy component and are ionized within the core boundary. Sensitivity studies showed that a variation of the core boundary flux dominantly affects the applied radial transport coefficients inside the pedestal top. Such a change does not affect the SOL and divertor conditions in the simulations. Helium and carbon densities are set to a fixed, experimentally determined value at the core boundary. At the main chamber and private flux region boundaries a perpendicular leak flux of each ion species, Γ_i, is recycled as neutrals with $\Gamma_i = \delta n_i c_s$, where c_s is the local sound speed, n_i is the ion density and δ is a free parameter. The parameter δ is particularly important in matching the upstream far SOL electron density and setting the main chamber recycling level. Values of $\delta = 0.005$–0.1 are employed. Wall pumping at the main chamber grid boundary can be mimicked by recycling only a fraction R of the plasma outflux. The wall pumping is particularly important to limit the core nitrogen content in simulations with nitrogen seeding that do not include drift effects. In line with experimental limits [387], values of $R \approx 0.95$–1 for nitrogen are used. Wall pumping for deuterium is not likely as the walls should be saturated with deuterium from previous discharges.

Sheath boundary conditions with separate ion and electron heat transmission coefficients, $\gamma_{e,i}$, are applied for energy fluxes at the targets. In line with literature [116] $\gamma_{e,i} = 2$–3 reproduce experimental target profiles in attached conditions. In detached conditions the solution is not very sensitive in the range $1 < \gamma_{e,i} < 5$ with the target parameters changing by 20 % at most. At the main chamber and private flux region boundaries, perpendicular temperature fall-off lengths, $\lambda_{e,i}$, are specified. Due to a lack of accurate experimental data the fall-off lengths are free parameters. A variation in the range $0.1 \text{ cm} < \lambda_{e,i} < 10 \text{ cm}$ at the main chamber and private flux region boundaries changed the target solution by less then 25 and 5 % respectively. Thus, the fall-off lengths are not dominant parameters in determining the power across the grid boundary. The power

crossing the private flux region grid boundary is set by the available power transported from the SOL into the private flux region. it is hence determined by the transport coefficients in the private flux region. For the main chamber boundary the dominant parameter is δ, because the effective conductive heat transport depends on the density ($\kappa = n\chi$), which is effectively set by δ. In all simulations the power flux to the main chamber walls is limited to ≤ 1 MW. The core boundary is used to couple the heating power into the simulation domain. For numerical stability a fixed temperature is set at the core boundary in a feedback loop such that the specified power into the domain crosses the core boundary. An equal distribution of the power to electrons and ions is assumed $P_{\mathrm{e}} = P_{\mathrm{i}} = 2.5\text{--}3.0$ MW. The power across the core boundary is determined from experiment by subtracting the radiated power inside the core plasma from the experimentally applied heating power.

Momentum boundary conditions have not been varied. At the target, sheath boundary conditions enforce the Bohm criterion with $u \geq c_{\mathrm{s}}$. The plasma velocity is not limited to c_{s} at the boundary. At all other boundaries the gradient in the radial Mach number profile is set to zero [89].

Additionally, a neutral puff flux is introduced via Eirene as a boundary condition. The puff sets the volume source terms for particles, energy and momentum from the neutrals. It is realized as point-like source with a cosine velocity distribution around the vertical direction at the coordinates where in the experiment the gas inlet valves are located. The nitrogen influx is set as a fixed influx. The deuterium flux can either be fixed or set in a feedback loop by the code to achieve a specified separatrix density.

5.5 Matching the Experiment

A detailed match of simulated plasmas to experimental plasma parameters requires two elements: First, the experimental measurements have to be compared to similar quantities derived from the modeled plasmas. An accurate comparison in itself is a challenge. Virtual diagnostics are crucial to accurately account for the characteristic measurement principles of each diagnostic, such as finite line of sight width, and include the experimental uncertainties in the evaluation of the synthetic diagnostics. In this thesis virtual diagnostics for the bolometry, the divertor spectroscopy, the Thomson scattering system, the ionization gauges and the Langmuir probes have been developed. Second, a merit function or an approach on how to match simulations with experiment has to be defined. Even given a set of validated virtual diagnostics that correctly compare experimental and modeling data, the definition of a simple merit function that characterizes the quality of the agreement of the numerical results with experimental data is not reasonable for a code like SOLPS. The high dimensionality in its input and output parameters with strong non-linear coupling between them prohibits the use of such a function. Unfortunately, this fact also prevents an automation of the fitting procedure for SOLPS. In the following, the applied process of achieving a validated plasma is described.

Matching Process
The quality of the match is characterized by simultaneous comparison of many diag-

nostics at different poloidal locations. With respect to a simpler TPM analysis and to available diagnostics a special focus is set on the outer midplane profiles that characterize the upstream conditions and the divertor targets. The approach to match experimental profiles is:

1. Set standard input parameters and boundary conditions for experimental plasma parameters.

2. Vary the radial profile of the transport coefficients, fueling and seeding rates to match the midplane profiles ($n_{e,i}$, $T_{e,i}$).

3. Vary the divertor boundary conditions to match the target profiles as closely as possible.

4. Vary the radial transport coefficient profiles and additional input parameters until a best, simultaneous match at the midplane and at the targets is achieved.

5. Check additional diagnostics for agreement (spectroscopy, bolometry, etc.) and adjust input parameters if necessary and possible.

Once the midplane profiles are matched, the further process is cumbersome as the effect of the input parameters can be highly interdependent. Educated guesses and a large number of simulations with parameter scans are necessary to achieve a decent simultaneous match. Including additional effects, such as drifts, will most often make it necessary to restart the whole procedure anew, because the equilibrium solutions change substantially. In addition, the history of a modeled plasma can allow or forbid access to a certain plasma solution. Sometimes the approach to a stable solution requires to transiently pass through an evolution, in which numerical instabilities or physical termination of the plasma, e.g. a radiation collapse, can occur. Hysteresis in the evolution of the plasma solution with a cyclic input parameter scan is also observed. All these effects and limitations lead to a timescale of the order of years to obtain a decently validated simulation.

Numerical simulations are often carried out as studies of physical trends in plasmas with parameters that only vaguely resemble the experimental ones [89, 347, 351, 388]. In contrast, the aim of SOLPS simulations in this thesis is to model an experimental discharge with a detailed validation of the simulated plasma by the experimental measurements. Such a comparison is necessary to validate the ability of the code to not only reproduce the correct trends in parameter scans, but to make an accurate numerical imitation of the experimental plasma. As will be shown, it has been possible to match the experimental measurements at the midplane and the target simultaneously. Integrated quantities, like f_{rad}, and qualitative distributions, like the absolute radiated power density, p_{rad}, or spectroscopically observed line radiation, are in good agreement with experiment. The comparison reveals on the other hand that in particular the simulated neutral densities in the divertor are significantly too low.

In comparison to previous modeling of high power H-mode plasmas, the level of agreement and the detailed analysis of the modeling is improved substantially. This work also is one of the first attempts to model high power H-mode plasmas close to detachment with a detailed experiment-code validation [130, 389–391].

5.6 Model Validation: Detailed Comparison with Experiment

The SOLPS simulations presented here focus on discharge #28903. This discharge is modeled for two time slices: At 2.4 s the inner divertor is detached and the outer divertor is in a high recycling state. The plasma is in the fluctuating state discussed in chapter 4 and no nitrogen is seeded. At 5.5 s nitrogen seeding is applied and completely detached targets are achieved. In both cases the separatrix electron density is about 2.5×10^{19} m^{-3}. The input power into the simulation domain is 5.5 MW for the high recycling case and decreased to 5 MW for the completely detached case due to increased core radiation. The computational grids for the numerical simulations are derived from the magnetic equilibrium.

The model validation against experimental data will be done for both cases separately. Carefully validated modeling of H-mode detachment at high heating power is presented for the first time. The extent

Figure 5.5: a)+b) Inter-ELM median values of the summed ion saturation currents to the target ,$\langle I_{\text{sat}} \rangle_{\text{ELM}}$, are given in blue and red for the inner and outer target respectively. $I_{\text{sat,TPM}}$ is given in green. c) Power spectrogram of AXUV-diode measurement at the X-point [130].

and quality of the match shown in this section is a novelty for SOLPS simulations of H-mode plasma scenarios. The agreement with the experimental data at the outer target and midplane simultaneously has been achieved by an increased perpendicular transport in the divertor, see section 5.8, and including drifts, see section 5.9, in the detached case. A match of the inner divertor target profiles at the same time necessitates rather strong additional assumptions on perpendicular transport.

5.6.1 High Recycling Regime

Simulations without drifts are able to reproduce almost all experimental measurements in the high recycling case and are presented in this section. A comparison of the experimental and modeled midplane profiles of electron density (a) and electron and ion temperature (b) for the high recycling case is shown in figure 5.6. Experimental data is shown as grey symbols and modeled profiles are given as solid lines. The electron density profile includes data from the lithium beam and the Thomson scattering diagnostic. The impurity density and the ion temperature of N^{7+} is measured by charge exchange recombination spectroscopy and the electron temperature is derived from electron cyclotron emission measurements. The scatter of the experimental data is due to a variation in the plasma parameters during the plotted time interval. The experimental profiles have
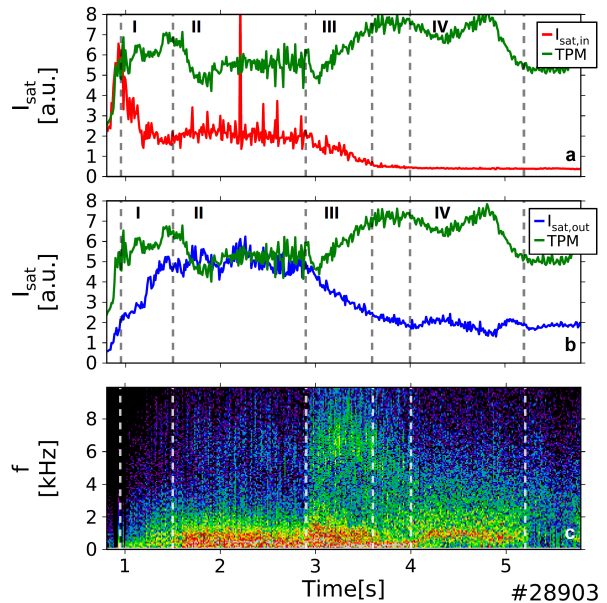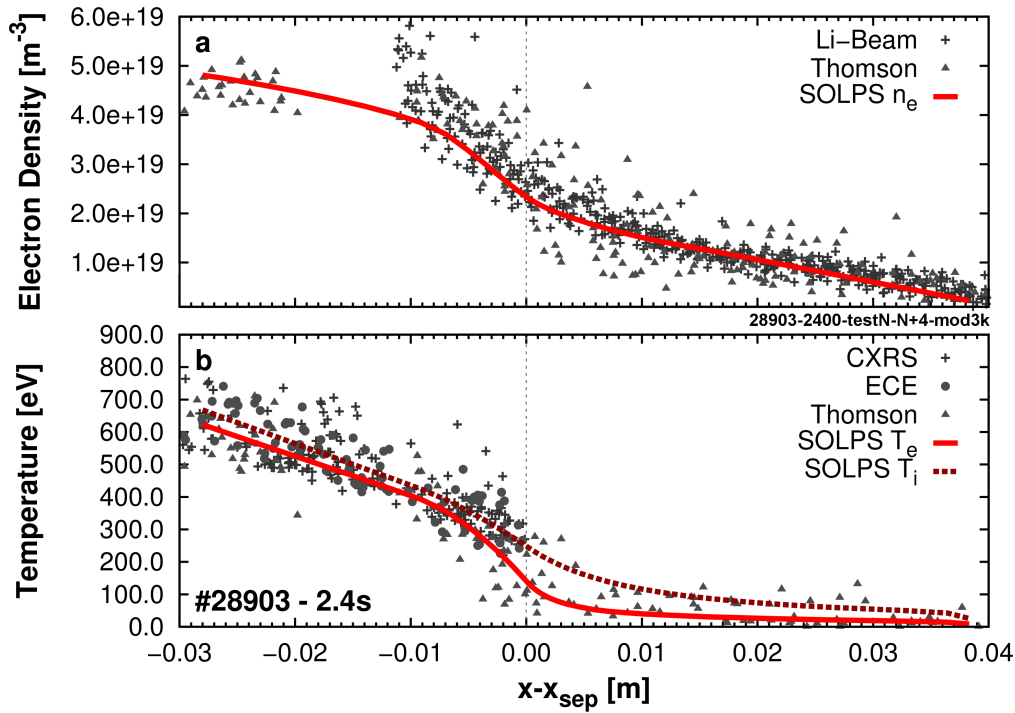
Figure 5.6: High-recycling case of #28903: Experimental data is shown as grey symbols. SOLPS data is shown in solid and dashed lines for (a) electron and N^{7+} density as well as (b) electron and ion temperature.
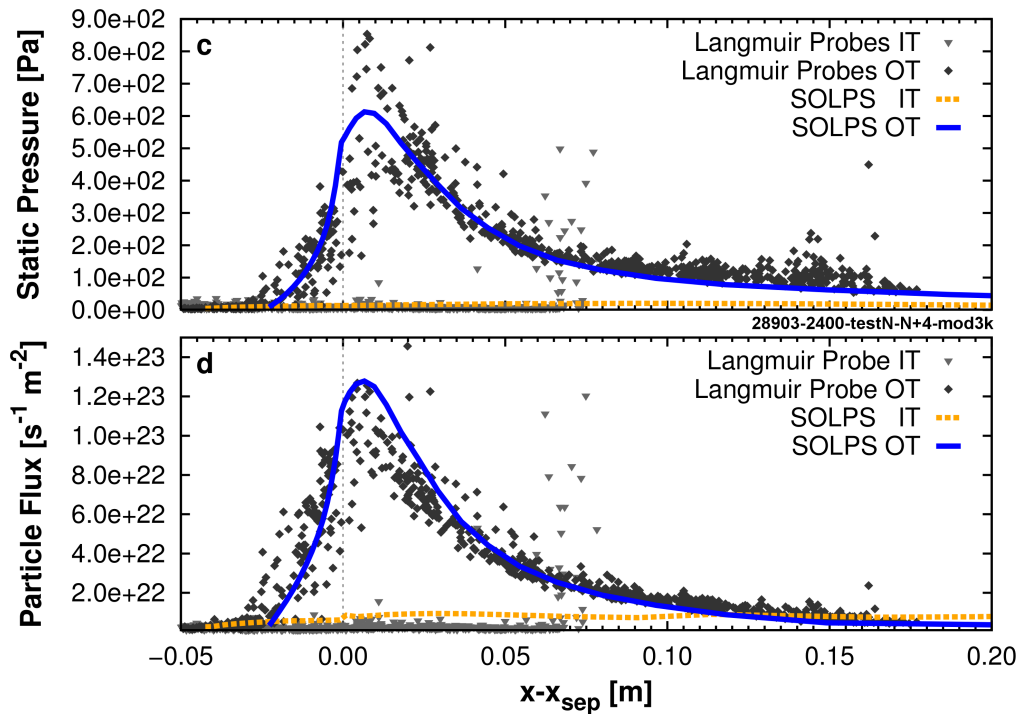

Figure 5.7: High-recycling case of #28903: Experimental data is shown as grey symbols. SOLPS data is shown in solid lines for and electron pressure (c) and particle flux at the outer (OT - blue) and inner (IT - orange) target.
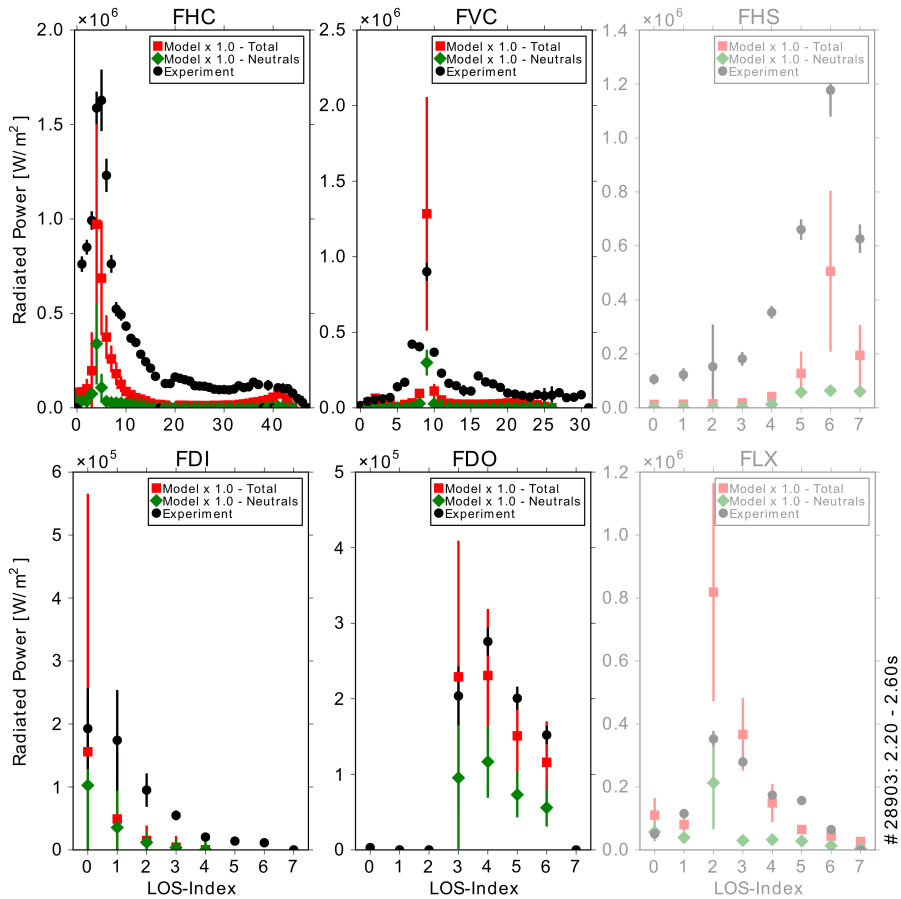
Figure 5.8: Experimental, line integrated radiated power density signals from foil bolometers (black) and the modeled radiated power density from a virtual diagnostic (red & green) are compared for the high recycling case of #28903. The experimental errorbars are the standard deviation of the signal during 400 ms. As a measure of the finite line of sight width of the diagnostic and possible misalignments the modeled errorbars represent the variation of the signal if the poloidal position of the endpoints of the line of sight is shifted by 5 cm. Some bolometer cameras (FHS & FLX) are not absolutely calibrated due to shadowing along the line of sight.

been shifted in the radial direction within the experimental uncertainties explained in chapter 3. The modeled and measured profiles show an excellent agreement within the scatter of the experimental data. Figure 5.7 shows the profiles of the static electron pressure (c) and the particle flux (d) along the target. The experimental ion saturation current is compared to the particle flux and the experimental static electron pressure is derived from Langmuir probe measurements of the electron density and temperature. The target profiles are shifted along the target within the limits given in chapter 3. The profiles at the outer target are shown in blue and dark grey diamonds. The profile shape peaks close to the strikepoint as expected for a high recycling divertor. The inner target profiles are shown in orange and in light grey triangles. As expected for a detached inner target during the fluctuating state, the profile shape is flat and the absolute values of the electron pressure and the particle flux are much lower compared to the outer divertor. The agreement of the target profiles of the electron density and temperature (not shown) is of similar accuracy in the high recycling case.
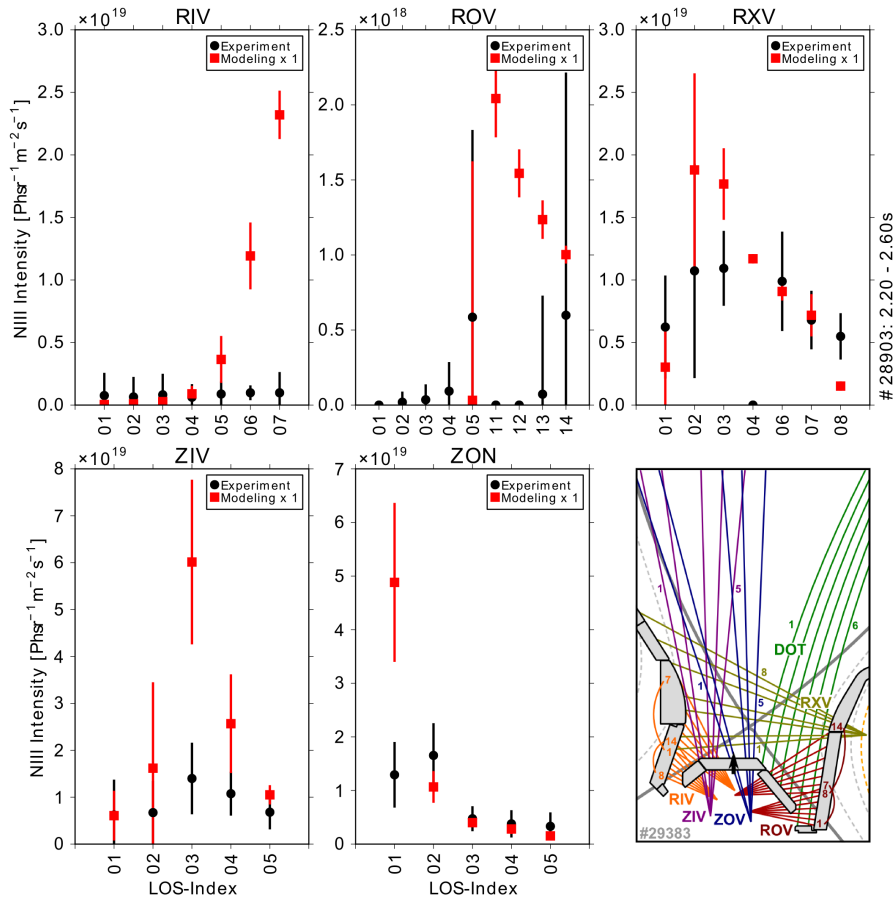
Figure 5.9: Experimental, line integrated NIII line intensities from divertor spectroscopy are compared to modeled ones from a virtual diagnostic for the high recycling case of #28903. The experimental errorbars are the standard deviation of the signal during 400 ms. The modeled errorbars represent the variation of the signal if the poloidal position of the endpoints of the line of sight is shifted by 1 cm.

The match of the target and midplane profiles indicates that the modeling correctly describes the dissipation integrated along the magnetic field in a TPM sense. However, the profiles of the plasma parameters and the localization of the power dissipation along the magnetic field are not well constrained by this comparison. The shape of the parallel profiles determines the poloidal location of the ionization and radiating regions and is very important for the overall plasma solution. Ideally, the parallel profiles should be measured directly, e.g. with a divertor Thomson scattering system as in Ref. [135]. In the absence of such a diagnostic the parallel profiles needs to be constrained by line integrated measurements. The spatial distribution of the radiated power can be validated by comparing the modeled signals from a virtual diagnostic with the foil bolometer measurements as shown in figure 5.8. The line of sight geometry of the foil bolometer system is shown in figure 3.6.a. The bolometer measurements show good agreement in the shape of the measured and modeled profiles along the fan of the bolometer cameras. The modeled line integrated powers are within a factor of 2–3 of the experimental ones. Lower absolute line integrated power in the simulation is expected due to missing contributions arising from radiation inside the core grid boundary for some bolometer cameras (FVC,
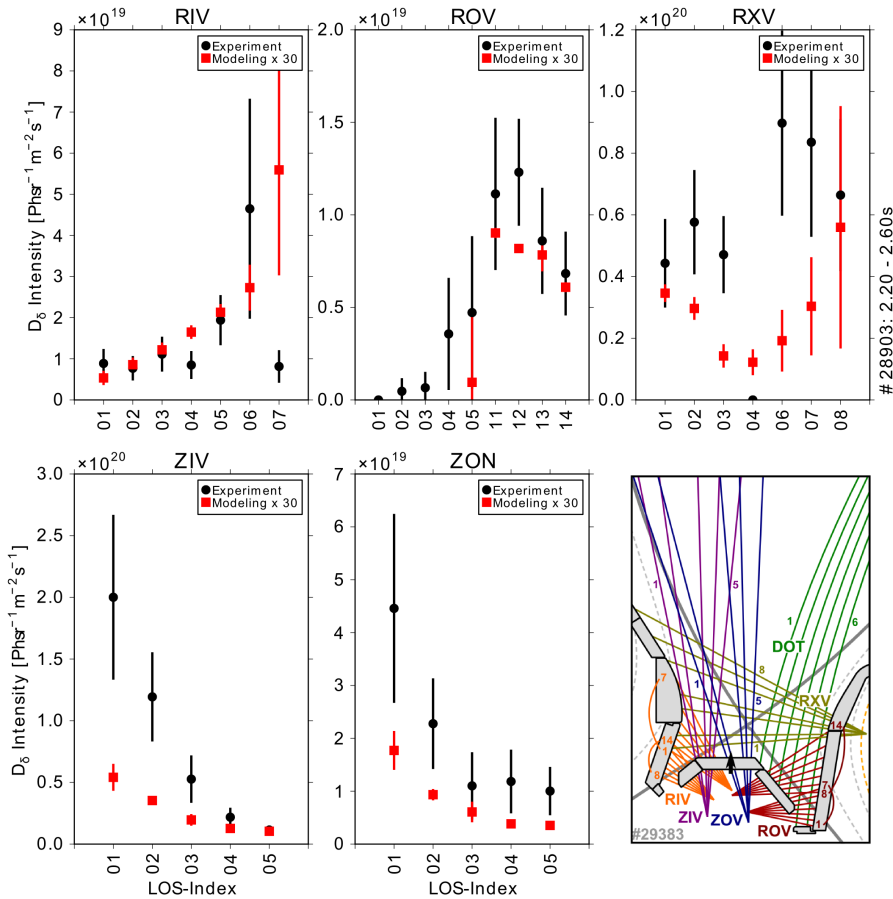
Figure 5.10: Experimental, line integrated Balmer D_δ line intensities from divertor spectroscopy are compared to modeled ones from a virtual diagnostic for the high recycling case of #28903. The modeled intensities are rescaled by a factor 30. The experimental errorbars are the standard deviation of the signal during 400 ms. The modeled errorbars represent the variation of the signal if the poloidal position of the endpoints of the line of sight is shifted by 1 cm.

FHC, FHS). The additional contributions from the core plasma would also reduce the stronger peakedness of the modeled profiles.

In summary, the spatial distribution of the radiation losses is well reproduced. Taking into account the radiated power inside the core grid boundary, the total radiated power is in good agreement with $f_{rad} = 54\,\%$ in the modeling and $f_{rad} = 59\,\%$ in experiment.

As described in section 4.4.5 the Balmer D_δ and NIII line radiation can be used as indicators of spatial regions of a certain temperature, i.e. the poloidal position of the temperature gradient region and regions of strong radiation, ionization or recombination. The line integrated line intensities in the divertor volume measured by the divertor spectroscopy are compared with a virtual diagnostic. The shape and the absolute intensity of the modeled NIII line profiles are shown in figure 5.9 and match with the experimental ones mostly within a factor of 3. The largest discrepancies are observed in the SOL of the outer divertor and in front of the inner divertor baffle, where the radiation is overestimated in the simulations. The profile shapes of the experimental Balmer D_δ

radiation are in agreement with the simulation as shown in figure 5.10. The modeled line intensity is about a factor 30 too low. In the proximity of the divertor baffle, where the HFSHD is located in experiment, the discrepancy is larger by an additional factor on 3. The electron density distribution in the simulation and in experiments is derived with the same Balmer D_δ Stark broadening diagnostic routines. Consistent with the previous observations, a comparison of these shows that the electron density is underestimated in the simulations by about a factor of 10 in the inner divertor volume away from the target. The lower Balmer line emission and density in the inner divertor volume is in line with an underestimation of the divertor neutral pressure and the deuterium fueling rates in the simulations by a factor of about 10. In the simulation, the neutral pressure ratios in the divertor at different poloidal locations are similar to the experiment, but the divertor compression, i.e. the ratio $n_{0,\text{midplane}}/n_{0,\text{div}}$, is a factor of 5–10 lower.

In conclusion, the modeling has demonstrated that a simultaneous match of the midplane and divertor target profiles can be achieved for high power H-mode experiments in the fluctuating state with a detached inner and a high recycling outer target. The radiation distribution and the radiated power fraction can be reproduced. This requires an increase of the perpendicular transport in the divertor as discussed in section 5.8. Comparison of the simulation with diagnostics that are sensitive to the plasma parameters in the divertor volume reveals remaining discrepancies, especially in the inner divertor. A larger temperature below the inner divertor baffle, an underestimation of the density in the HFSHD region and a too low neutral pressure are observed in the modeling. Despite the good agreement of the plasma solution with most of the experimental data, the remaining discrepancies point to a deficiency of the SOLPS code to describe the divertor compression and the core plasma fueling correctly, see section 5.10.2. Experimentally observed neutral pressures in the divertor cannot be reproduced at experimental separatrix electron densities. An increase in the neutral density at constant midplane conditions would lead to a better agreement of bolometer, neutrals flux and spectroscopic intensity measurements.

5.6.2 Detached Regime

In contrast to the high recycling case, simulations of the completely detached plasma require the inclusion of drifts into the simulations. A comparison of the modeled and experimental midplane profiles of the electron density (a) as well as the electron and ion temperature (b) with completely detached targets is shown in figure 5.11. A comparison of the static electron pressure and particle flux profiles along the divertor targets is shown in figure 5.11. The experimental profiles have been shifted radially and along the target within the uncertainties given in chapter 3. As expected for completely detached targets, the pressure and the particle fluxes at the outer target are strongly reduced compared to the high recycling case and the fluxes at the inner target are not sufficient for the evaluation of the experimental Langmuir probe data. The shown midplane and target profiles are well reproduced within the experimental uncertainties. In contrast to the high recycling case, the experimental target profiles exhibit a significantly higher temperature of around $T_e = 2$ eV and a lower density than the profiles in the simulations (not shown). As discussed in chapter 3 the Langmuir probe analysis below $T_e \approx 2$ eV overestimates
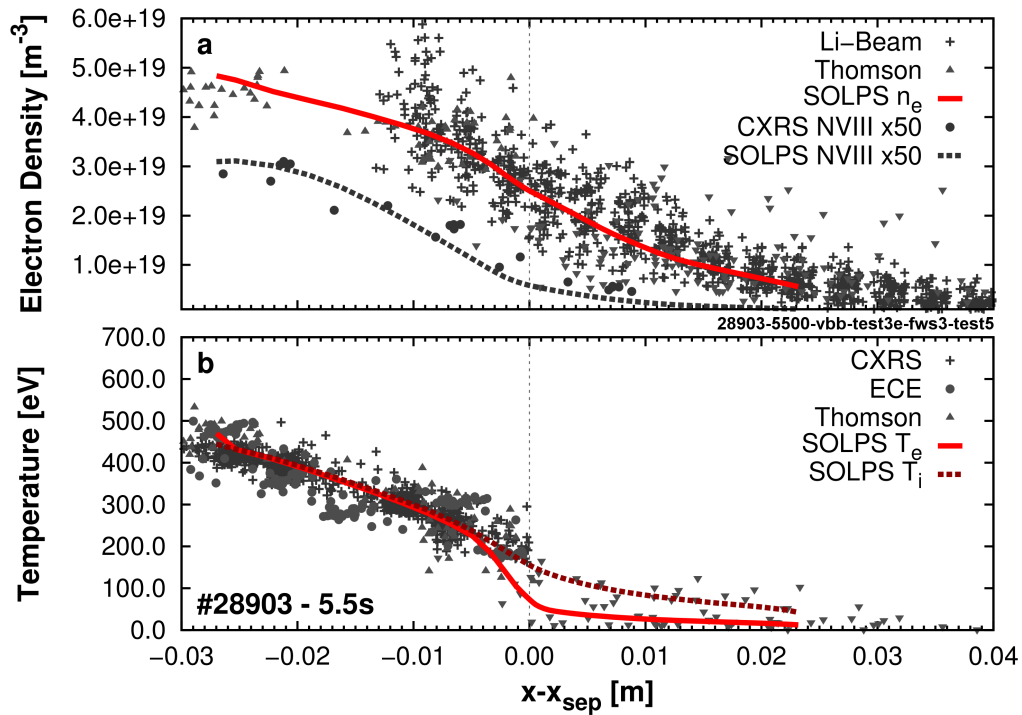
Figure 5.11: Completely detached case of #28903: Experimental data is shown as grey symbols. SOLPS data is shown in solid and dashed lines for (a) electron and N^{7+} density as well as (b) electron and ion temperature.
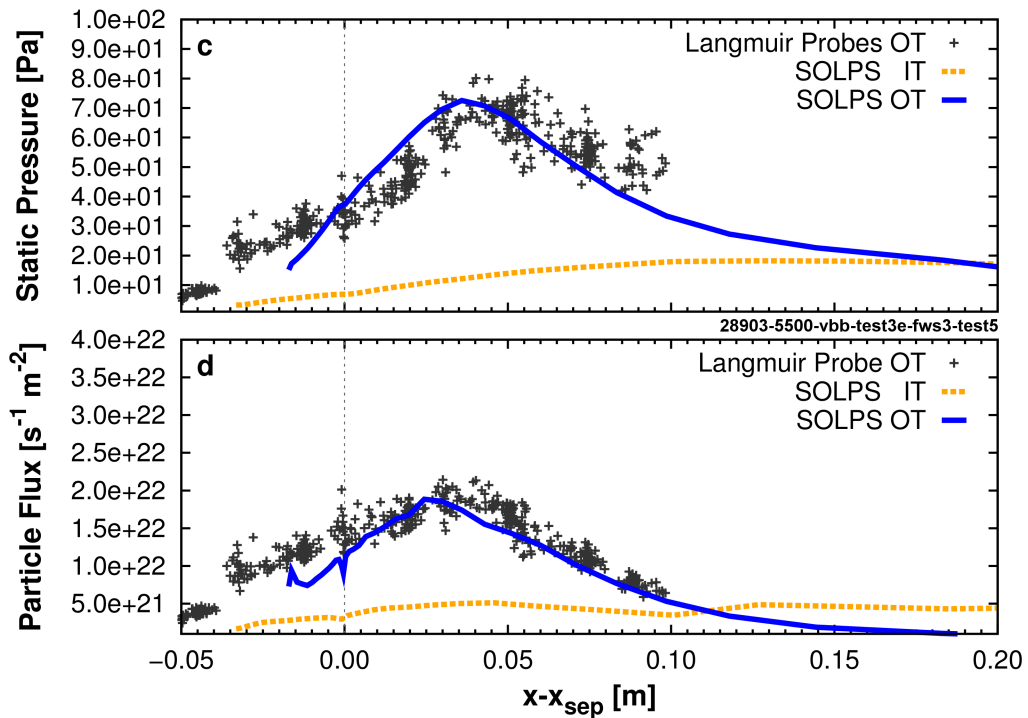

Figure 5.12: Completely detached case of #28903: Experimental data is shown as grey symbols. SOLPS data is shown in solid lines for and electron pressure (c) and particle flux at the outer (OT - blue) and inner (IT - orange) target.
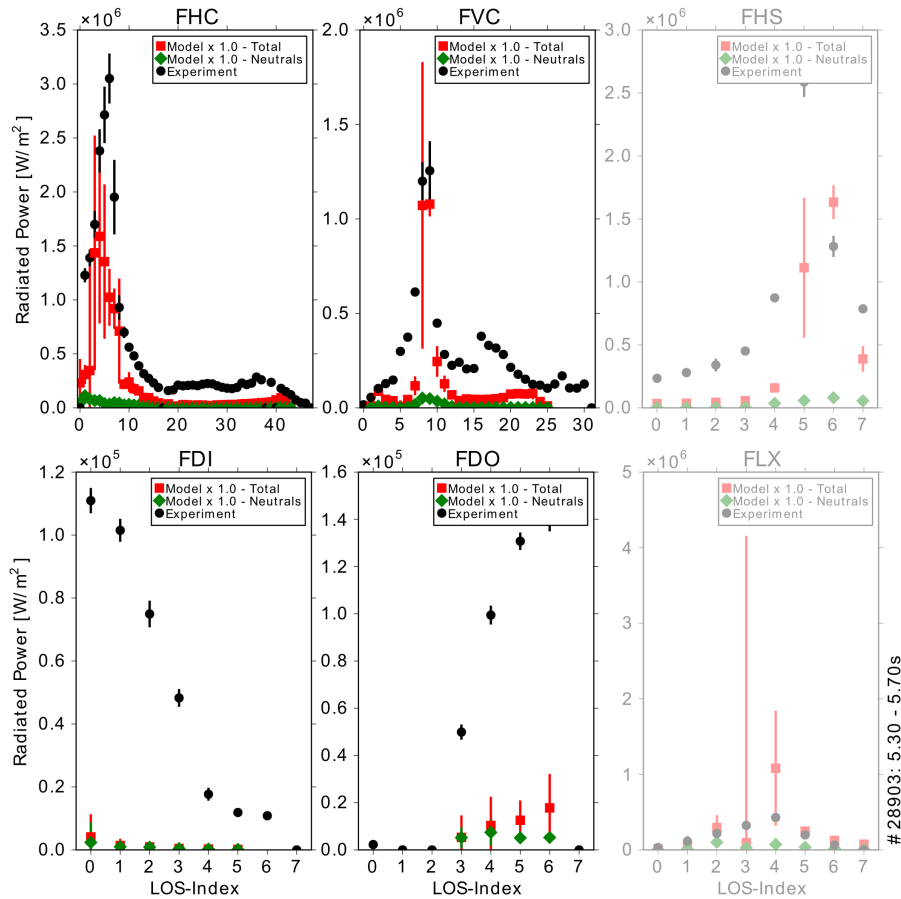
Figure 5.13: Experimental, line integrated radiated power density signals from foil bolometers (black) and the modeled radiated power density from a virtual diagnostic (red & green) are compared for the completely detached case of #28903. The experimental errorbars are the standard deviation of the signal during 400 ms. As a measure of the finite line of sight width of the diagnostic and possible misalignments the modeled errorbars represent the variation of the signal if the poloidal position of the endpoints of the line of sight is shifted by 5 cm. Some bolometer cameras (FHS & FLX) are not absolutely calibrated due to shadowing along the line of sight.

the temperature [290]. The target temperatures in the simulations compare well with the order of magnitude of spectroscopically derived temperatures using Balmer line ratios, which are about 0.3 eV close to the targets. With a simultaneous match of the midplane and target pressure profiles the experimental parallel power and pressure loss integrated along the magnetic field is recovered in the simulation.

The volumetric power losses due to radiation are again validated by comparing the modeled signals from a virtual diagnostic to line integrated measurements of the foil bolometers. The profile shapes are in good agreement for all bolometer cameras and a quantitative match within a factor of 1.2–2 was obtained for the cameras, for which the line integrals are dominated by radiation from the X-point (FVC, FHC, FLX & FHS). However, the simulations showed less radiation ($\Delta \approx 50$–150 kW/m^{-2}) in the inner and outer divertor legs close to the strikepoint (FDI & FDO) when compared to the experiment. However, the integrated radiated power in the divertor legs is small
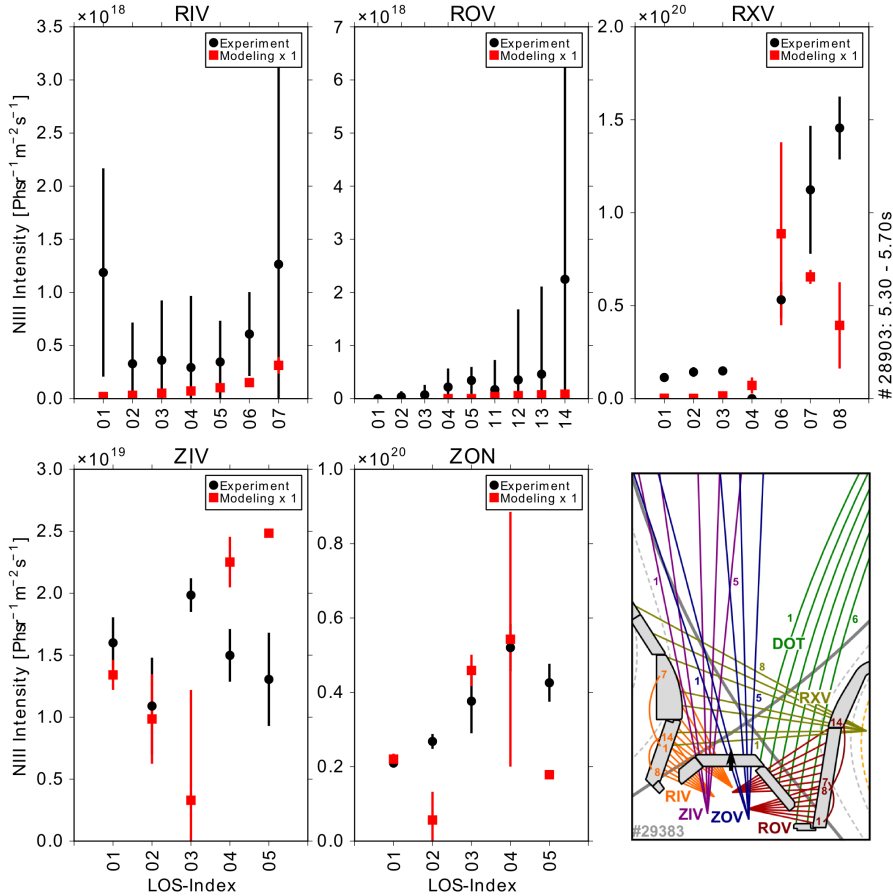
Figure 5.14: Experimental, line integrated NIII line intensities from divertor spectroscopy are compared to modeled ones from a virtual diagnostic for the completely detached case of #28903. The experimental errorbars are the standard deviation of the signal during 400 ms. The modeled errorbars represent the variation of the signal if the poloidal position of the endpoints of the line of sight is shifted by 1 cm.

compared to the radiated power at the X-point and the achieved radiated power fractions are the same for the modeling and the experiment with $f_{\mathrm{rad}} = 85$ %. Comparable to the experiment, the radiated power fractions saturate at this level in simulations with the same plasma parameters. Increased nitrogen seeding in the simulations and in experiment does not significantly increase f_{rad} without leading to a radiation collapse.

In order to achieve completely detached target profiles in the simulations, it is necessary to seed enough nitrogen to form the intense X-point radiation. As in the experiment this correlates in the simulations with a decrease of the midplane separatrix temperature from $T_{\mathrm{e,sep}} \approx 100$–120 eV to about 50–80 eV and to the appearance of an X-point MARFE inside the confined plasma. As observed in the experiment, the pressure gradient inside the separatrix increases with the transition to localized radiation within the confined plasma due to increased density and ion temperature gradients. In the simulations this regime is very unstable without the increased divertor transport and when neglecting drifts.

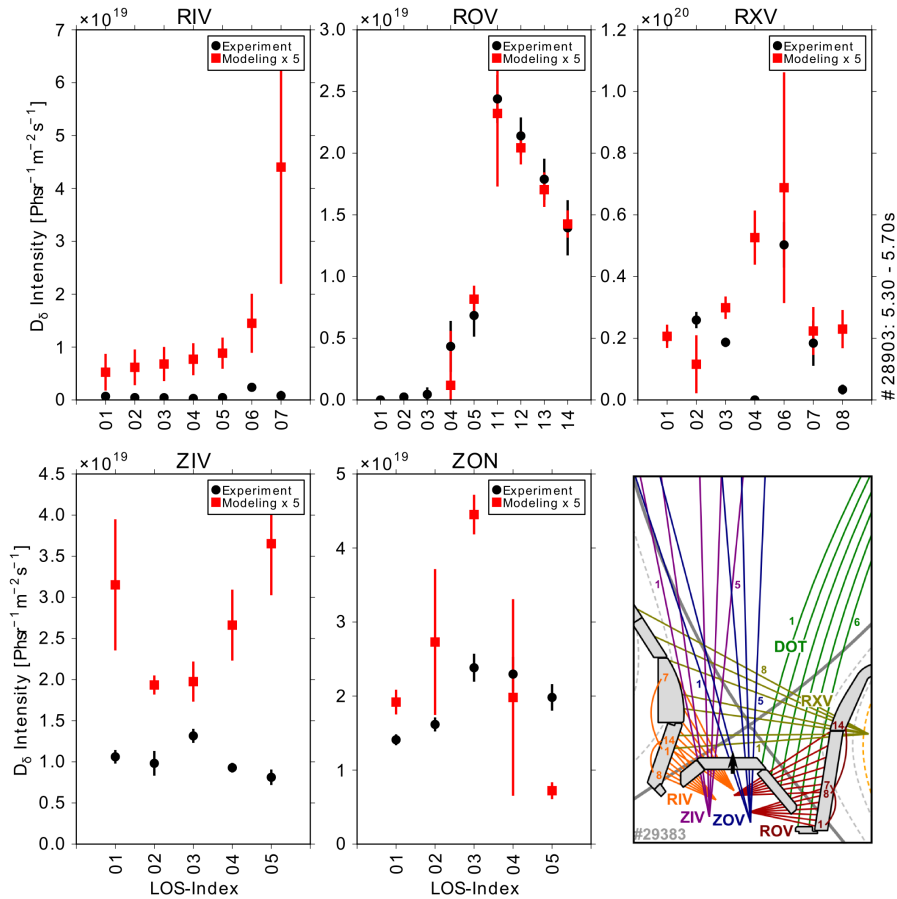In order to validate the divertor plasma in the divertor volume away from the targets, a

Figure 5.15: Experimental, line integrated Balmer D_{ffi} line intensities from divertor spectroscopy are compared to modeled ones from a virtual diagnostic for the completely detached case of #28903. The modeled intensities are rescaled by a factor 30. The experimental errorbars are the standard deviation of the signal during 400 ms. The modeled errorbars represent the variation of the signal if the poloidal position of the endpoints of the line of sight is shifted by 1 cm.

comparison of the modeled and the experimental line integrated NIII line intensities is shown in figure 5.14. The NIII line intensities are well reproduced in the inner and outer divertor volume within a factor of 2. Consistent with the experiment there is almost no NIII radiation close to the strikepoint at the target in both divertor legs (RIV & ROV) and the overall intensity is low. The simulation underestimates spatial extent of the radiating region for the NIII line radiation above the X-point (RXV). A comparison of modeled and experimental Balmer D_{δ} line radiation intensities is shown in figure 5.15. The shape of the Balmer D_{ffi} line radiation profiles are in excellent agreement and the absolute intensity is underestimated by a factor 5 in most of the divertor, except for the inner divertor where the modeled radiation intensity is matches quite well with the experiment (RIV & ZIV). The electron density distribution derived from the same Stark broadening evaluation of experimental and modeled data shows an agreement of the evaluated densities within 20–50 % with the exception of the vertical lines of sight at the X-point (ZON 3–5) and horizontal lines of sight above the X-point (RXV 6–8). The vertical lines of sight show a similar HFS-LFS asymmetry in the simulations as

seen in figure 5.14 for the NIII line emission. Deviations from experimental densities of up to a factor of 2 occur for both sets of lines of sight (ZON & RXV). Despite the absence of the HFSHD region in experiment for detached conditions, the modeled divertor neutral densities and the divertor compression are still a factor 4–6 lower than in the experiment.

In summary, the modeling has demonstrated that for completely detached, high power H-mode discharges a simultaneous match of the midplane and the divertor target profiles can be achieved. The radiation distribution, the radiated power fractions and a number of experimental observations, like localized X-point radiation inside the confined region, a pedestal top pressure loss, parallel temperature gradients on closed field lines and low temperatures at the X-point, are reproduced. Comparison of the simulations with diagnostics that are sensitive to the plasma parameters in the volume show a good agreement with small deviations above the X-point. The modeled divertor compression and the neutral densities in the divertor are still a factor 3–6 too low.

In order to achieve the presented level of agreement of the simulations with the experiment, a number of non-standard assumptions and transport models have been employed. Most important is a modification of the perpendicular transport coefficients in the divertor, which will be discussed in section 5.8. A second modification, discussed in section 5.2.6, is the inclusion of plasma drifts in detached simulations that help to stabilize the X-point radiation and redistribute particles and power in the divertor. The impact of different recycling assumptions and the implications of the mismatch in the neutral density are discussed in section 5.10. The detachment process as observed in the presented SOLPS simulations is analyzed and dicussed in section 5.7.

5.7 The Detachment Process in the Simulations

In the SOLPS simulations of complete detachment, the parallel pressure loss in the SOL and the target particle fluxes observed in the experiment can only be reproduced with intense, localized radiation at the X-point inside and outside of the confinement. Only when the X-point radiation moves inside the confined region, the experimentally observed pressure loss at the pedestal top and at the separatrix occurs and the experimental foil bolometer measurements of the radiated power at the X-point can be reconstructed in the simulations. The pedestal pressure loss with complete detachment of the divertor targets can be explained by a large parallel power losses along closed field lines and power dissipation by the X-point radiation inside the confined region. At the onset of the radiation inside the confined region parallel losses and temperature gradients are the largest close to the separatrix. This increases the radial temperature gradients locally. The radial power flux increases and flux surfaces radially further inward cool down to temperatures where impurity radiation becomes efficient in the proximity of the X-point. The volume of the radiating region is largest at the X-point due to the large flux expansion. The large parallel connection length at the X-point reduces the parallel gradients. The poloidal portion of the fluxtube that experiences increased radial gradients is small and strongly localized at the X-point. The radiation moves radially inward until the decrease in flux expansion and an increasing parallel gradient are such

that the dissipated power and the net power flux into the radiating region equilibrate. The plasma will suffer a radiative collapse if no such equilibrium exists or if the change in neutral penetration and the subsequent change in core fueling and the electron density dominates. If an equilibrium is attained increased temperature gradients inside the pedestal and a flat radial temperature profile as well as a pressure loss at the separatrix are established. The reduction in temperature around the separatrix region as well as local recombination at the X-point increase the ionization sources inside the confined plasma, effectively increasing the fueling efficiency and the plasma density.

The reduction of the power and particle fluxes at the divertor targets with complete detachment is mainly due to a reduction of the available power for ionization, especially in the divertor volume. The divertor is starved of power and the target particle and heat fluxes drop with the recycling level. In a nitrogen seeding rate scan the integrated ionization source has dropped by a factor of 5 when complete detachment is achieved. The recombination sink increases by a factor of 2, but is still only 50 % of the ionization source.

The increased transport in the divertor additionally increases the losses of particles and energy to the private flux region. The X-point radiation leads to large poloidal gradients, especially in the plasma temperature. As shown in figure 5.1, this leads to large drift-induced radial fluxes that cause high plasma densities in the proximity of the X-point and increase the power and particle losses from the outer divertor SOL into the private flux region. The density in the inner divertor volume stays high despite low densities and fluxes at the target as observed in the experiment. Drift fluxes provide a particle flux from the private flux region into the divertor X-point region and push the radiating ionization region away from the target to the divertor entrance, see figure 5.18. The increased divertor transport and drift fluxes along the separatrix in the inner divertor ensure that the particles are lost to the private flux region or recycled into the X-point region before reaching the vertical target component. This ensures the plasma depletion that is observed in the inner divertor leg while maintaining high densities at the X-point and in the far SOL above the divertor baffle.

The ability of the simulations to reproduce the experimental parallel pressure loss and the reduction of the particle fluxes at the target with a significantly reduced neutral pressure compared to the experiment could indicate that charge exchange momentum losses are not a dominant loss channel for plasma pressure. As stated above, the dominant contribution to the reduction of the plasma pressure and the particle flux to the target is the power dissipation inside the confined plasma that leads to a power starvation of the divertor. Shallow parallel temperature gradients in the divertor volume from the X-point to the target also increase the contribution of convective transport. Following the extended Two Point Model in (2.14) this further reduces the expected particle flux and pressure at the target.

Unfortunately, it is not possible to consequently rule out the possibility that charge exchange momentum losses could have a dominant impact on the detachment process, because the neutral density is significantly underestimated in the simulations. The requirement of increased perpendicular transport in the divertor could be a manifestation of missing charge exchange losses in the simulation due to the lower neutral density. An

artificial increase of the neutral density is not possible in the self-consistently calculated plasma solution, but a variation of the charge exchange reaction rates has been tested. In simulations without the dominant charge exchange reactions 7 and 12 in table 5.1 the modeled target pressure and particle flux profiles change only by about 30 % for similar midplane conditions. This is also true for simulations with a fourfold increase of their charge exchange reaction rates. In simulations with deactivated deuterium recombination, reaction 2 in table 5.1, a similar order of plasma parameter variation at the target is observed. The relatively minor corrections of the target profiles despite a strong variation in the rates again indicate that momentum loss due to charge exchange or recombination does not dominantly cause detachment in the presented plasma scenario. The reduction of the power into the divertor is the dominant mechanism in AUG H-mode detachment experiments that reduces the particle flux and the plasma pressure at the divertor target.

For a better constraint of the modeling, additional spectroscopic measurements can be used. However, new divertor diagnostics are required that measure a poloidal or parallel distribution of the plasma parameters in the divertor volume between target and X-point. Especially the position and spatial extent of the radiation, ionization and recombination regions are important to constrain with experimental data. The parallel plasma parameter profiles would also determine the relative importance of the convective parallel transport. From a divertor Thomson system the parallel profiles could be derived [134,135,171,203] and in combination with the evaluation of the ionization source distribution from spectral line emission analysis [269] the perpendicular transport in the divertor could be derived or at least constrained.

5.8 Effect of Increased Perpendicular Transport in the Divertor

SOLPS calculates the perpendicular fluxes from a radial profile of ad-hoc transport coefficients that is specified at the midplane. The transport coefficients are rescaled with the inverse of the flux tube width and a ballooning-like, poloidal variation is applied. The main transport coefficients are the electron heat conductivity, χ_e, the ion heat conductivity, χ_i, and the particle diffusivity, D. In drift cases an

Quantity	Core	Pedestal	SOL
χ_e [m^{2}s^{-1}]	0.30–0.90	0.01–0.50	0.30–2.00
χ_i [m^{2}s^{-1}]	0.30–0.90	0.05–0.50	0.30–1.00
D [m^{2}s^{-1}]	0.30–0.90	0.01–0.50	0.50–2.00
v [m s^{-1}]	0.00	0.00–2.00	0.00

Table 5.3: The range of transport coefficients for the modeling of #28903 is given.

inclusion of an inward drift velocity, v, in the pedestal can be necessary to achieve gradients that are steep enough to match experimental profiles. The magnitude of such an inward pinch is reduced to a minimum in the presented simulations. Identical transport coefficients are assumed for main and impurity ions. The profile shape in all simulations is similar. The coefficients profile is constant inside the pedestal, decreases in the pedestal in order to form the steep gradient region and increases radially in the SOL. The magnitude of transport coefficients applied can be found in table 5.3.

Simulations with the standard transport model of SOLPS failed to reproduce the mid-

plane and the target plasma parameters profiles simultaneously. If the experimental midplane profiles were matched with the radial transport coefficient profile, the target profile always showed a stronger peaking of the electron density and the plasma pressure compared with experimental target profiles. Experimental observations of locally increased transport in the inner divertor due to filaments [345] and indications of an increased perpendicular transport in the proximity of the X-point [132, 212] motivated the use of locally enhanced perpendicular transport in the divertor volume. A new transport model was introduced into the SOLPS code, that allows to separately rescale all transport coefficients for all the four divertor regions shown in figure 5.4. Additional rescaling of the transport coefficients or a specification of additional contributions to the local transport coefficients with a gaussian spatial profile centered around the X-point can be applied.

The simulations with a rescaling of the transport in the divertor regions show that to match the outer target profiles of the particle flux and pressure in H-mode experiments in high recycling and with detached targets it is necessary to increase the transport coefficients in the divertor region by factors 2–10. In order to similarly match the inner divertor target profiles, a further increase in the inner divertor by an additional factor 2–10 is necessary. A larger rescaling of the perpendicular transport in the inner compared to the outer divertor was also necessary to stabilize the numerical scheme with drifts. A local increase or rescaling of the transport coefficients in the proximity of the X-point can also reproduce the experimental target profiles in the simulations in the high recycling case.

A missing component of the transport model would be the influence of additional convective parallel transport in the private flux region from the outer divertor to the inner divertor due to blob filaments as observed in Ref. [345]. This has the potential to further the observed asymmetries in both divertors and enhance the density in the inner divertor that is still to low in the region of the high field side high density in the high recycling simulation. A similar effect is observed using the drifts, see section 5.2.6.

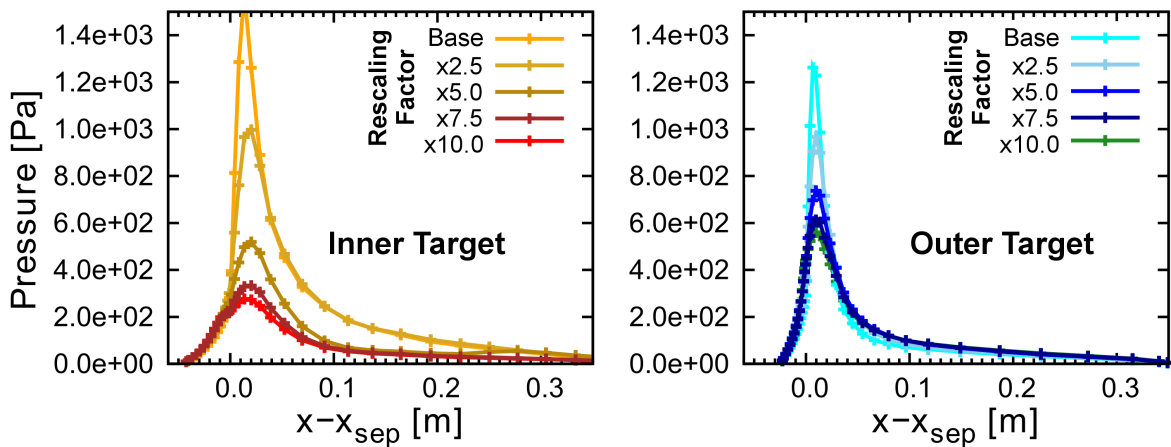In order to illustrate the impact of the increased perpendicular transport in the divertor

Figure 5.16: The effect of an increase of perpendicular transport coefficients in the divertor region by a constant factor [130].

a scan of the rescaling factor is discussed in more detail for non-drift simulations of the high recycling case. Figure 5.16 shows the evolution of the target plasma pressure profiles. The midplane pressure profile (not shown) does not change during this scan. The dominant effect of the increased transport is a broadening of the electron density profile around the separatrix and a reduction of the peak density. The way of reducing the peak particle flux to the target is different in the inner and outer divertor: In the inner divertor the temperature drops to low values around 1 eV across the whole target and the density profile broadens significantly. The peak density is reduced by about 30 %, but the far SOL density increases by factors of the order of 10. Both, peak pressure and pressure across the whole target, are reduced. In the outer divertor a large decrease in the peak density and increasing fall-off length into the SOL lead only to a reduction of the peak pressure close to the separatrix. The peak particle flux to the outer target is reduced by a factor of 2–5, whereas the integrated flux to the target reduces only by about 10–20 % due to an increase of the particle flux in the far SOL.

With the inclusion of drifts into the simulations, the inner vertical target tends to detach completely and the particle flux up to the divertor baffle ($x - x_{\text{sep}} \approx 0.10$ cm) drops to very low values below 0.5×10^{22} m^{-2}s^{-1}.

In simulations with detached conditions that include the drift effects, the increased perpendicular transport leads to increased fluxes to grid boundary of the outer private flux region and of the main chamber SOL. A transport increase by a factor of 2 varies the distribution of the radiated power. It decreases in the divertor and increases in the confined plasma by 10–30 %, but the overall radiation varies by only about 1–5 %. The increased transport also leads to a broadening of the density and radiation profile in the divertor volume. Due to lower plasma density in the divertor recombination and momentum losses are reduced with respect to the reference case without increased transport. This again implies that the pressure in our simulations is not lost due to increased plasma-neutral interaction or recombination, but that the enhanced cross-field transport leads additional pressure reduction along a field line. For the inner divertor the losses into the private flux region in combination with drifts are particularly important for the detachment of the vertical target below the divertor baffle. It has to be noted that with the transition to the X-point radiation inside the confined plasma the necessary transport rescaling in the divertor can be reduced by a factor of about 5 in the outer and 10 in the inner divertor compared to values used for the high recycling case.

In summary, the simulations have shown that an increased perpendicular transport in the whole divertor volume or in the proximity of the X-point is necessary to reconcile the modeled target profiles with experimental measurements. Such an increase of perpendicular transport also increases the numerical stability of simulations with drifts for completely detached divertor targets. The dominant effect of the increased transport is a broadening of the electron density profiles and a reduction of the peak pressure and particle flux in both divertors, due to increased losses of power and particles to the private flux region and the far SOL. With the transition to completely detached targets and radiation inside the confined region, the divertor transport increase can be reduced significantly.

5.9 Effect of Drifts

The effects of drifts on the plasma solution is discussed in this section. The inclusion of drifts is not necessary to reproduce most of the experimental profiles of the high recycling plasma. In the high recycling plasma, large radial gradients in the divertor result in strongly varying drift fluxes that are a challenge for proper convergence of the simulations. A stabilization and convergence of drift simulations in high recycling conditions is still on-going and the preliminary, detailed match of those drift simulations with the experimental data is still not of comparable quality to non-drift simulations. In detached conditions drifts are required to match the experimental data.

The effect of drifts in detached H-mode simulations can be studied in a scan of a drift factor, that rescales all perpendicular fluxes caused by drifts. Such a scan with fixed perpendicular transport coefficient profiles and gas puff rates is shown in figure 5.17. It shows the evolution of the plasma pressure profiles at the outer midplane and at the targets successively taking into account larger fractions of the perpendicular fluxes caused by drifts. The reduction of the pressure in the confined plasma is due to the diamagnetic drift that causes a net outflux of particles and energy across the separatrix. Compared to the upstream separatrix pressure loss of about 60 %, the pressure drop at the outer strikepoint is substantially larger and reaches almost 85 %. Thus, the drifts
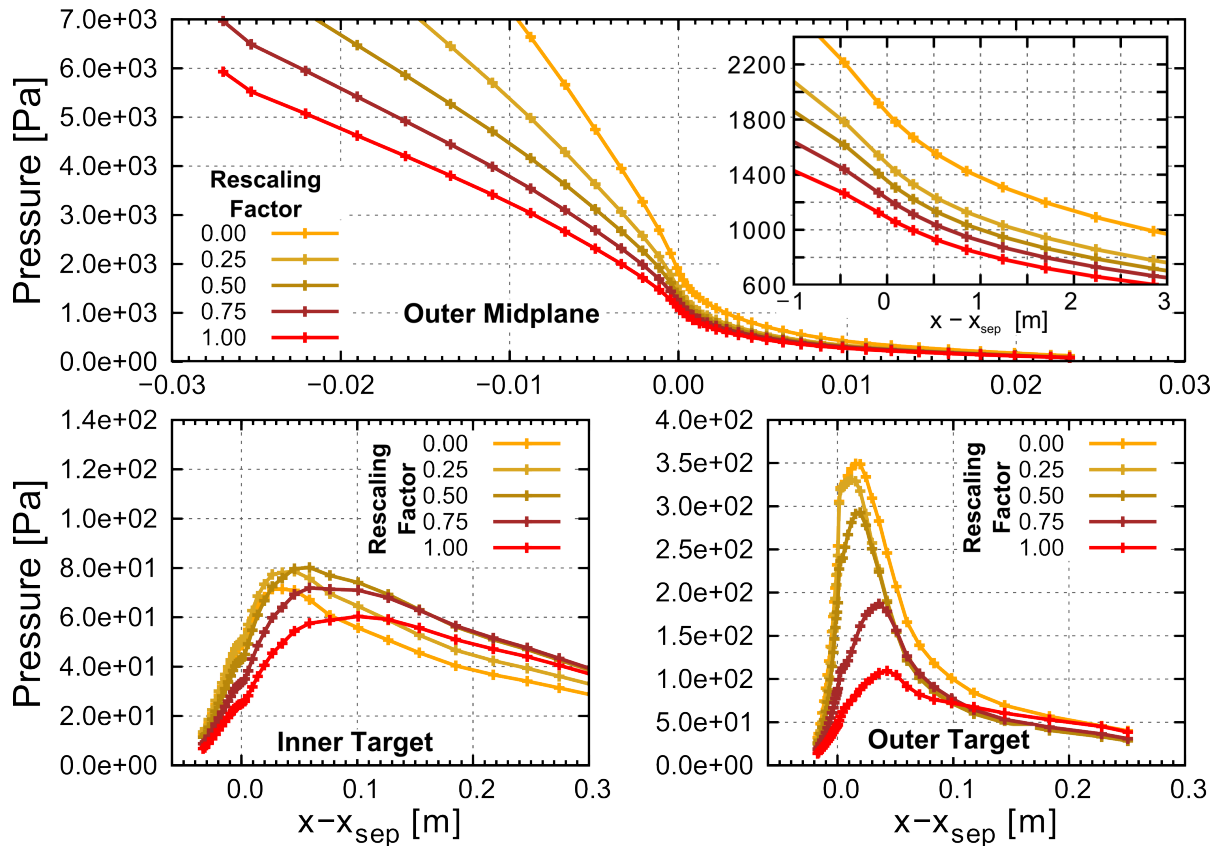

Figure 5.17: The effect of the increasing transport due to drifts. The fluxes caused by drifts are rescaled successively until the full drift transport is included.

change the upstream conditions and have an additional effect on the divertor plasma, that leads to a pressure loss and a redistribution of the plasma parameters within the divertor volume. With increasing transport coefficients the target electron density and temperature profiles show a roll-over like behavior. First, the temperature at outer target increases across the whole target. Above a rescaling factor of about 50 % the temperature decreases from the separatrix outwards into the far SOL. A similar trend is observed at the cold inner target. Inversely, the outer target electron density first decreases and then increases along the whole outer target. At the same time the profile broadens into the SOL. At the inner target the electron density increases first and then decreases along the whole target while it broadens during the whole evolution.

As shown in figure 5.18, the evolution of the density and temperature as well as the change in impurity fluxes with increasing drift effects gradually change the radiation distribution in the inner divertor from a V-shaped front in the divertor legs close to the target to a more straight front at the divertor entrance well above the divertor target. In the outer divertor the extent
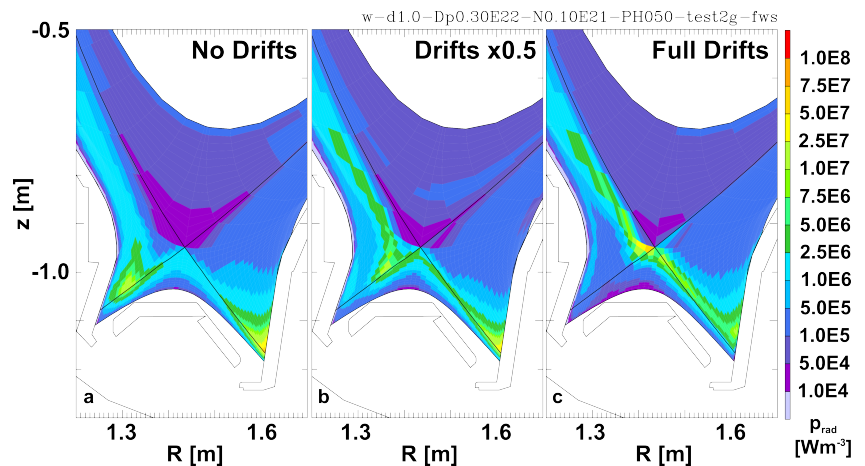
Figure 5.18: Changes of the location and the spatial extent of the radiating region in a scan of the drift-flux rescaling factor are shown.

of the radiating region grows along the separatrix up to the X-point and the radiated power increases. The movement of the radiating region from the inner target to the inner divertor entrance results in a cold, dense divertor plasma ($T_{e,i} = 1.5$–2 eV) in the whole inner divertor volume. However, the divertor volume with plasma conditions necessary for recombination to dominate ($T_{e,i} < 1$–1.5 eV) stays close to the target and expands only very little in size.

Increasing the nitrogen seeding rate further, the radiation moves inside the confined plasma (not shown). The contribution of core radiation within the simulation domain to the total radiated power increases from about 10 to 50 %. In a seeding rate scan in simulations, with drifts the transition of the dominant radiation region from the inner to the outer divertor to the confined plasma is more abrupt compared to non-drift simulations. Drifts stabilize the localized radiation inside the confined plasma at the X-point with respect to the occurrence of a radiative collapse of the plasma. Also the radiation within the confined region shows a hysteresis effect with respect to the nitrogen seeding rate. Once the core radiation at the X-point is established the nitrogen seeding rate can be dropped significantly below the seeding rate at which the core radiation was established before the radiation is pushed out of the confined region again. In the experiment such a strong hysteresis is not observed.

The effect of the different drift terms on the electron density and temperature are shown
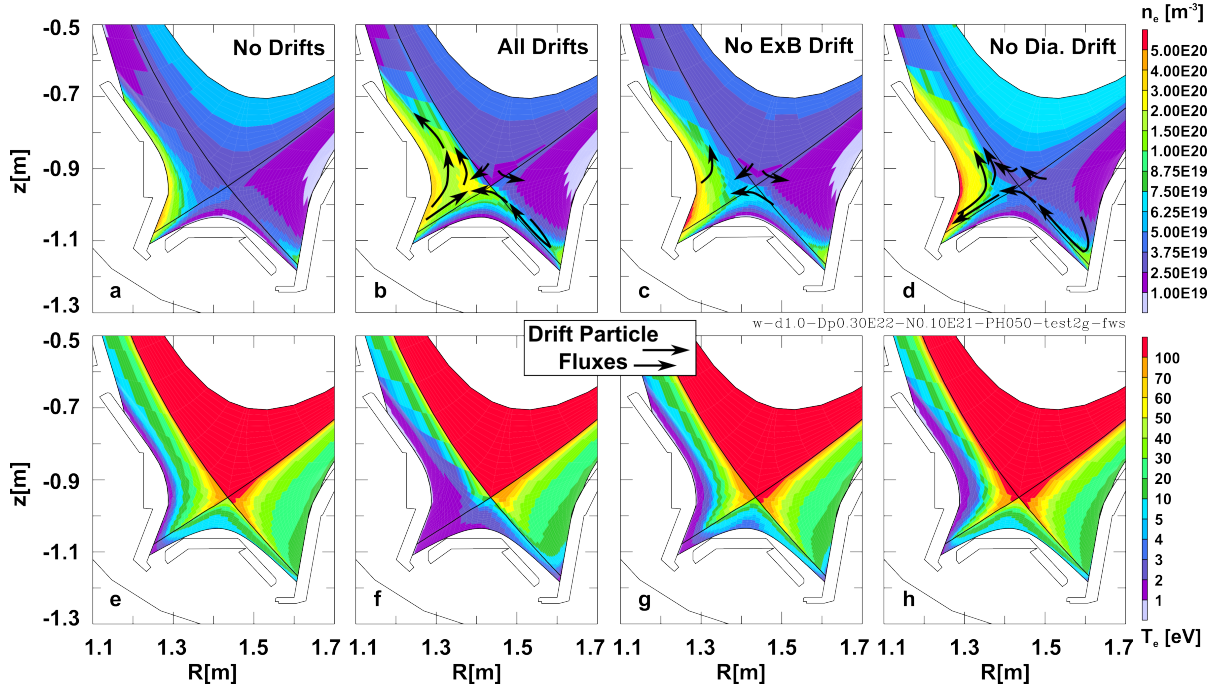
Figure 5.19: Electron density (top) and temperature (bottom) are shown for simulations close to complete detachment and dominant X-point radiation. The activation of different drift terms changes the plasma solution and the general dynamics of the drift-induced particle fluxes that are indicated with black arrows.

along with the pattern of drift induced particle fluxes in figure 5.19. Both the diamagnetic drift and the $\vec{E} \times \vec{B}$ drift lead to an increase of electron density in both divertors that is particularly strong in the inner divertor volume. The diamagnetic drifts alone lead to an increase along the whole inner target with the strongest effect in the inner divertor leg below the divertor baffle and to an inverse decrease of the temperature. The $\vec{E} \times \vec{B}$ drifts alone result in a more evenly distributed increase of the density in the inner divertor and the affected volume extends farther from the divertor baffle to the X-point and into the far SOL.

The combined effect of both drifts leads to the formation of a high density region close to the X-point in the inner divertor at the expense of density in the divertor leg below the baffle. The large density in the inner divertor far SOL is maintained in the inner divertor. With high density above 1×10^{20} m^{-3} in the whole inner divertor up to the X-point, the temperature decreases to low values below 2 eV. In the outer divertor the far SOL density is decreased with respect to the $\vec{E} \times \vec{B}$ drift simulation, but drifts lead to deuterium particle fluxes along the outer strikeline from the target to the X-point and into the private flux region. The particle flux to the target is reduced, especially close to the outer strikepoint. The reduction of the flux to the vertical target component seems to be driven by drift fluxes in the proximity of the X-point and above the divertor entrance that push the plasma out into the far SOL and even away from the target.

The effect of drifts on impurities is two-fold. The increase of the density in the divertor leads to an increase of the friction force [48, p.55] due to collisions with the deuterium ions. Reduced parallel temperature gradients reduce the thermo-force [48, p.55] that

results from an electron temperature gradient and that pushes the impurities out of the
divertor in the direction of the paralllel gradient. It has to be noted that the impurity
divertor retention without drifts is too low to match the experimental plasmas. For the
experimental separatrix densities the core plasma nitrogen concentration in the simula-
tions needs to attain values of 5–10 % in order to reach the experimental radiated power
fractions. Even with unphysical assumptions for input parameters, e.g. wall pumping of
40 %, the quality of the match is far from the drift simulation results.

As stated above, the inner vertical target component detaches more easily with drifts and
the peak electron density and particle flux moves up along the target towards the divertor
baffle as observed in experiment. Figure 5.20 shows poloidal profiles of the plasma
parameters and the perpendicular fluxes in the SOL fluxtube adjacent to the separatrix
for the drift simulation shown in figure 5.19.b+f. As expected from the theoretical model
in section 5.2.6, the drift-induced perpendicular fluxes are the largest at the X-point,
where the alignment of the region of steep parallel gradients in the electron temperature
and pressure with the region of high electron and ion densities are collocated. The
perpendicular particle fluxes lead to the described particle transport from the outer to
the inner divertor transport via the private flux region and from the X-point region close
to the separatrix in the inner divertor into the far SOL above the divertor baffle.

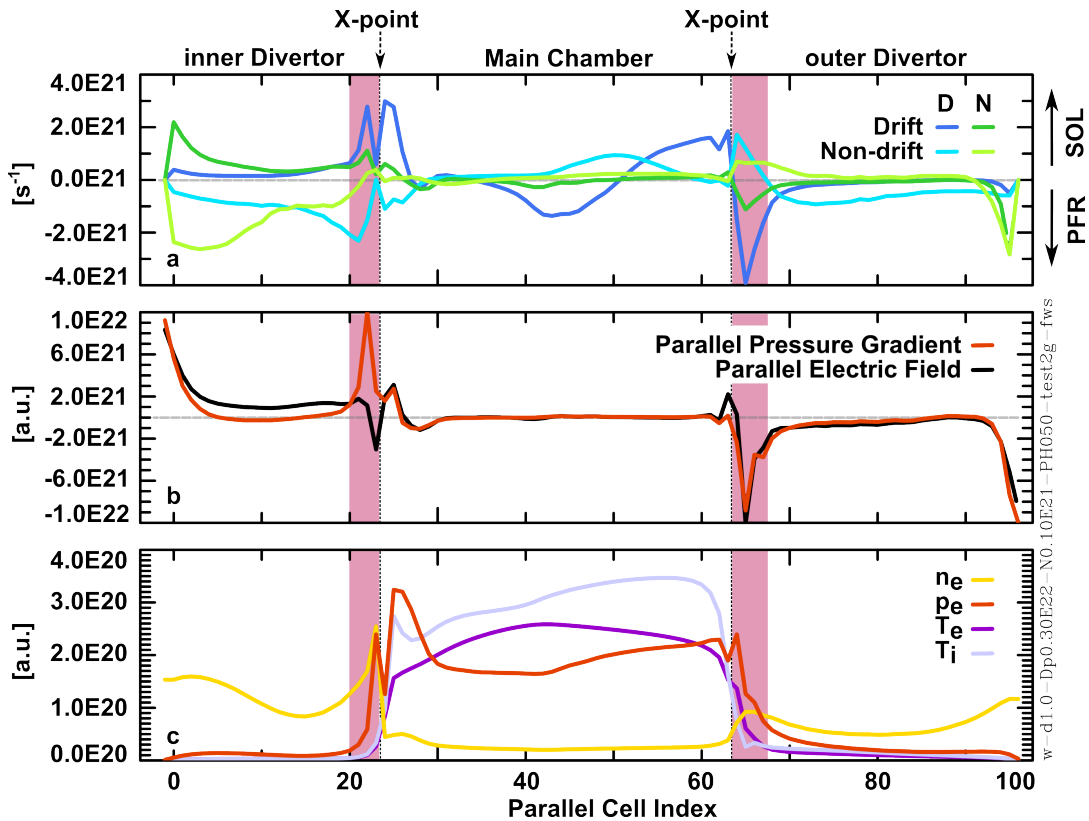In high density simulations the vertical target component can reach deep detachment and

Figure 5.20: Poloidal profiles of the plasma parameters and the perpendicular fluxes
in the SOL fluxtube adjacent to the separatrix for the drift simulation shown in figure
5.19.b+f. The drift-induced fluxes are largest in the steep gradient region close to the X-
point.

virtually no particle flux onto the target is left. Unfortunately, the low particle fluxes at the vertical inner target component in such simulations lead to numerical instabilities in the code that tend to terminate the simulations. A first analysis seems to connect this to a reversal of the total particle flux at the inner target boundary. The plasma flow is locally reversed and the Bohm boundary condition is violated. Most likely an adaptation of the Bohm boundary condition is required for this plasma regime.

In initial drift simulations of the high recycling case, a high density region in front of and above the inner divertor baffle with a maximum close to the divertor baffle and at the X-point can form. Concomitantly, a local enhancement of the neutral density in the inner far SOL is observed. Similar to experimental observations that have been presented in section 4.4.6, the increase in the far SOL neutral density is also reflected in the virtual diagnostics for the neutral pressure gauges at the HFS limiter and the divertor spectroscopy of Balmer line radiation.

Effectively, in detached simulations with strong nitrogen seeding, drifts redistribute particles from around the strikepoint into the far SOL and from the outer into the inner divertor. The spatial extent of the region of high electron density in the inner divertor volume increases towards the X-point and the drifts ensure a reduction of the particle flux to the vertical target. The density in the divertor volume increases while the temperature in the divertor volume decreases. With drifts the radiating regions broaden and move away from the target plate. In the inner divertor the radiation front moves to the divertor entrance with a maximum at the X-point. In the outer divertor the radiation increases along the outer separatrix up to the X-point. Additionally, with drifts impurities are better confined inside the outer divertor, which is the main leakage of impurities from the divertor in non-drift simulations. The impurity fluxes from the outer to the inner divertor along the SOL are reduced whereas the impurity transport from the outer to the inner divertor through the private flux region is increased. Initial drift simulations of the high recycling case indicate that a high field side high density region can be reproduced in the simulations.

5.10 Recycling

As presented in section 5.4, the recycling of the main ion species and impurities at the plasma-wall interface is the dominant source of neutrals within the plasma. Depending on the local plasma conditions and their kinetic energy, their penetration depth into the plasma varies substantially. High densities with temperatures above the ionization threshold effectively shield neutrals from penetrating deep into the plasma.

For neutral transport in remote areas behind the plasma facing components, a neutral conductance model can allow or inhibit neutrals to escape from the divertor or travel from the inner to the outer divertor. Thereby, the conductance model influences the ionization source, the divertor impurity retention and the divertor neutral compression.

The impact of the assumptions on the recycling and the neutral conductance is assessed in this section.

5.10.1 Impurity Recycling & Main Chamber Pumping

A challenge in non-drift simulations at the experimental midplane separatrix density of $n_{e,sep} = 2.5 \times 10^{19}$ m^{-3} is to limit the core impurity content to experimental levels at the high impurity seeding rates that are necessary to achieve the experimentally observed radiated power fractions. In non-drift simulations the divertor retention of nitrogen in the presented H-modes is low and the core concentration of nitrogen is about 5–10 %. Main chamber pumping of nitrogen is necessary to limit the core content of nitrogen to experimental levels that is around 2 %. In line with Ref. [387], wall pumping of 0–5 % of the impinging nitrogen flux to the main chamber wall and full recycling of nitrogen at the divertor targets have been assumed in the simulations. Main chamber wall pumping of nitrogen reduces the core content of nitrogen and the local impurity concentration in the main chamber SOL. In drift simulations of the detached plasma case the main chamber wall pumping leads to an enhanced code stability, especially with strong radiation at the X-point.

In a parameter scan of heating power, deuterium fueling and nitrogen seeding rates, the divertor impurity retention in the simulations decreases significantly for increasing heating power and decreasing density. The divertor retention is decreased due to a suppression of friction forces acting on the impurities while increasing the thermal force pulling the impurities out of the divertor. For higher charge states of the impurities the friction force at the entrance of the divertor close to the X-point can even reverse sign, which is consistent with the evolution of the flow pattern. Stronger reversal of the plasma flow along the outer divertor separatrix leg is observed with increasing heating power. With larger deuterium fueling and at higher divertor densities the divertor retains impurities better even at high heating power due to increased friction forces in the divertor volume.

The effect of ELMs on the impurity content has been assessed via a series of ELM simulations similar to Ref. [347]. It has been found that the mock-up ELMs neither lead to flushing of nitrogen nor to a reduction in the overall core content of nitrogen.

In the presented simulations the nitrogen was puffed and recycled in the form of atoms. In reality, nitrogen molecules (N_2) are puffed and in the recycling process molecules could be formed. In order to assess the effect of N_2 molecules as seeding and recycling species a simple breakup chain for N_2, similar to the one employed in Ref. [371], was introduced into Eirene. The simulations revealed that the inclusion of molecular nitrogen changes the global plasma parameters such as the radiated power, the integral ion fluxes to the targets and the core nitrogen content by less then 20 %. The target and midplane profiles change by 5–10 %.

The modeling showed that the recycling model can influence the plasma solution, especially the impurity content. In particular the experimentally little constrained effect of impurity wall pumping is important. The divertor impurity retention is dominantly set by the outer divertor in the simulations. The interplay of parallel friction and thermal forces acting on the impurity ions as well as the direction of the plasma flow and the location of the ionization region for the impurities determine the ability to retain impurities in the divertor. The recycling of nitrogen as molecules does not significantly

influence the simulated plasmas. The impact of ELMs on the impurity content and impurity transport is small in our simulations.

5.10.2 Neutral conductance & Neutral pressure

The most striking discrepancy to the experiment in the simulated plasmas is the low neutral density in the divertor, which is a factor 3–10 lower than in the experiment for both simulated plasma scenarios. Consistent with the lower neutral density, a similar underestimation of Balmer line emission in the divertor is seen in the simulations. Dedicated efforts to match the neutral influx and pressure in the divertor have not been successful, yet. So far, the increase of the divertor neutral density to experimental levels is coupled to an increase of the separatrix density by at least a factor of 2. The magnitude of this increase is not within experimental errorbars and cannot be explained by radial shifts of the midplane profiles within the allowed range.

Experimental line ratio measurements of Balmer $D_{\delta,\varepsilon}$ in the inner divertor indicate a much wider spatial extent of the recombination region than present in the simulations. In simulations with higher separatrix densities than and similar divertor neutral densities as in the experiment, the extent of the recombination region and the Balmer line emission match the experiment within a factor of 2. The results again indicate that the code does not reproduce the experimental divertor neutral compression and overestimates the core plasma fueling.

The ratio of the poloidally distributed neutral fluxes in the divertor are in general similar in experiment and modeling. An exception is the absence of higher neutral fluxes at the HFS limiter gauge (F11) in the high recycling case. The experimental neutral fluxes at this location are close to values measured below the roof baffle (F07) as discussed in section 4.4.6. Taking into account the neutral fluxes inside the SOLPS grid at far SOL edge of the inner divertor, the neutral flux at the HFS limiter shows 5–10 times lower neutral fluxes in non-drift simulations compared to the experiment. As already stated before, simulations of the high recycling case with drifts seem to reproduce this local increase.

Variations of the neutral conductance model of the subdivertor structures and of the pumping of neutrals did not significantly reduce the observed discrepancies in the divertor neutral compression or the mismatch of the HFS gauge in the high recycling cases. The modeling indicates a deficiency of the code in predicting the correct divertor neutral compression and core plasma fueling.

5.11 Discussion & Summary

This chapter showed that agreement of the SOLPS simulations of high power H-mode discharges in ASDEX Upgrade with experimental measurements of most divertor and main chamber diagnostics can be achieved in both simulated plasma scenarios. The fluctuating detachment state with a high recycling outer divertor and a detached inner

divertor as well as the completely detached state have been modeled. The modeling of such plasma scenarios is a novelty. The extent of the validation with experimental measurements and its level of agreement for the presented H-mode simulations has been substantially improved compared to previous modeling of other H-mode plasmas. The applied boundary conditions in the simulations are within the experimental limits and most modeling parameters are fairly standard choices.

Special features of the experimental H-mode detachment experiments at ASDEX Upgrade are a strongly localized, pronounced X-point radiation in the confined plasma and a related pedestal top pressure loss. Both are reproduced in the SOLPS simulations. The simulations show that the pedestal top pressure loss is induced by the reduction of the temperature due to the large parallel energy losses into the X-point radiation region on closed fieldlines. Despite the large parallel conductivity, significant parallel temperature gradients with temperatures as low as 1 eV in the proximity of the X-point are established on closed field lines.

Modeling shows that an unconventional assumption of an increased perpendicular transport in the divertor of ASDEX Upgrade is required to reproduce experimental measurements at the midplane and at the target simultaneously in both modeled H-mode plasma scenarios. A larger transport increase in the inner than in the outer divertor is necessary to simultaneously match both targets. The transport increase necessary to match the divertor target profiles in high recycling conditions is a factor 5–10 for the outer divertor and a factor 50–100 for the inner divertor in non-drift simulations. In completely detached plasma simulations the inclusion of drift effects is required to match and stabilize the experimentally observed X-point radiation. The appearance of the X-point radiation inside the confined plasma and the use of drifts in the completely detached plasma simulations reduce the necessary divertor transport increase to a factor 2 for the outer and 10 for the inner divertor.

The dominant effect of the increased transport is a broadening of the electron density profiles and a reduction of the peak pressure and particle flux to the target in both divertors. The impact of charge exchange and recombination on divertor detachment was shown to be of minor importance for the simulated pressure loss. The particle flux reduction at the target dominantly stems from the reduction of the power flux into the divertor and the increased perpendicular transport of power and particles into the private flux region and the far SOL.

In detached simulations with strong nitrogen seeding, drifts are necessary to reproduce experimental observations such as a detached vertical inner target, improved X-point radiation stability and improved impurity retention of the divertor. Drifts redistribute particles from around the strikepoint into the far SOL and from the outer into the inner divertor via the private flux region. The good alignment of the high density in the ionization and radiation region and the strong temperature gradient region at the X-point causes large perpendicular drift fluxes that are of the same order as the perpendicular fluxes due to the gradient-driven transport. The drift fluxes cause an increase of the spatial extent of the region of high electron density in the inner divertor towards the X-point, broaden the radiating regions in both divertors and move them away from the target plates.

In drift simulations of completely detached plasmas the target sheath boundary conditions potentially need to be revised. The Bohm boundary condition seems to be a limitation for the numerical stability of the code and a challenge for further improvement of the match to experimental data.

A remaining discrepancy between the simulations and the experiment in both plasma scenarios is that the code predicts neutral densities in the divertor that are a factor 3 to 10 lower than in the experiment. The discrepancy consistently can be observed in the underestimation of spectroscopic Balmer line intensity, neutral flux and neutral pressure measurements in the divertor. Efforts to achieve experimentally observed neutral densities in the divertor at experimental separatrix densities were not successful and point to a deficiency of the code to describe the divertor neutral compression and the core plasma fueling correctly.

A series of sensitivity scans included the recycling of nitrogen as N_2 and impurity transport due to ELMs. No significant effect on the plasma solution was found. In contrast, changes to the model for recycling changed the plasma solution. In particular, wall pumping of nitrogen and the particle reflection model have a significant impact on the core impurity content and the simulated target profiles. Both properties of the recycling model are not well constrained by direct experimental measurement and it is necessary to gather more accurate data from simulations and experiments.

5.12 Open issues

During the work on this thesis a number of issues came up that could not be analyzed in sufficient depth due to time constraints and the limited of the scope of this work. Nevertheless, the following issues should be subject to further research:

- Study impact of photon opacity for the stability and formation of the X-point radiation in the confined plasma.

- More detailed neutral density investigations with simulations that include the neutral conductance of inter-tile gaps in the toroidal and poloidal direction, neutral-neutral collisions, extended grids to the first wall as well as drift effects in the high recycling case.

- Improvement of experimental and virtual diagnostics, e.g. divertor Thomsom, especially to further constrain the parallel plasma parameter profiles and the spatial location of the radiation, ionization and recombination in the divertor volume. With such data the relative importance of perpendicular transport, convective power transport and momentum losses due to charge exchange and recombination should be assessed in detail.

- Validation of drift effects in the simulated plasma regimes with field reversal experiments.

- Code convergence tests, especially concerning the grid resolution due to the large gradients at the X-point.

- Development of a physical parameterization of the transport coefficient increase. An inclusion of a convective transport from the outer to the inner divertor inside the private flux region should be implemented [345].

- Investigations on the recycling and wall pumping model with respect to carbon or boron layer formation and nitrogen chemistry (ammonia formation). The particle and energy reflection model potentially including molecular dynamics simulations should be a part of such work.

- High performance discharge simulations at highest heating powers at ASDEX Upgrade have been started in the framework of this thesis, but did not advanced to a level where a detailed comparison to the experimental data is useful. Validated simulations at higher heating power and density would allow an assessment of the scaling of the modeling results to different operational parameter regimes beyond unvalidated parameter scans in the simulations.

- Time-dependent simulations including ELMs and tungsten as an intrinsic impurity should validate the dynamics of the physics included in the code.

CHAPTER 6

Summary & Conclusions

In future fusion devices like ITER and DEMO power exhaust is a challenge. In a fusion reactor like DEMO power fluxes along a field line connected to material divertor elements of several $10\,\mathrm{GWm}^{-2}$ are to be expected. Accounting for geometrical effects the remaining power flux to the divertor target is of the order of several $100\,\mathrm{MWm}^{-2}$, which is still well above the specified steady-state material limits of $5 - 15\,\mathrm{MWm}^{-2}$. For target protection, radiation cooling in the confined region, in the SOL and in the divertor with a radiated power fraction of $f_{\mathrm{rad}} \approx 95\,\%$ is necessary. In addition, the particle fluxes carrying the atomic ionization energy to the wall have to be limited by a reduction of the plasma pressure, i.e. detachment. A good characterization and understanding of divertor detachment in H-mode plasmas with high radiated power fractions and significant power fluxes to the divertor is crucial to validate the theoretical models and to extrapolate the experimental results to devices like DEMO.

The present work has shown that in ASDEX Upgrade complete detachment of both divertor targets can be achieved when nitrogen is puffed as a radiating impurity into the divertor plasma. The obtained discharges are stable and well controlled H-modes at high heating powers of up to 12.5 MW with acceptable low core impurity levels. An undesired back transition to the L-mode regime as suggested in Refs. [105, 133] was not observed.

The experiments showed that the classification of the detachment process is similar to that found in L-Mode discharges [1] with the addition of a new phase during complete detachment. In this phase radiation at the X-point inside the confined plasma emerges. The intense, localized X-point radiation reduces the power flux into the divertor, thereby reducing the level of recycling and the target particle flux. The X-point radiation leads to a reduction of the plasma pressure at the pedestal top ($\varrho_{\mathrm{pol}} = 0.95$) and at the separatrix with only small changes of the core plasma pressure ($\varrho_{\mathrm{pol}} < 0.7$). The reduced pressure at the separatrix and increased radial gradients of the plasma parameters in the edge plasma ($0.7 < \varrho_{\mathrm{pol}} < 0.90$) facilitate divertor detachment while maintaining good core plasma performance and confinement at confinement factors of $H_{98} = 0.8 - 1.0$. High radiation losses at and above the X-point are beneficial for power dispersal across the entire first wall as long as the impact on confinement is not detrimental. In our experiments the energy confinement time of the plasma was reduced by about 5–10 % during complete

detachment with nitrogen seeding.

Analysis of the X-point radiation with visible spectroscopy revealed low plasma temperatures ($T_e < 5 - 10$ eV) and high plasma and neutral densities above the X-point inside the confined plasma. The measurements imply large poloidal temperature variations on closed field lines despite the high thermal conductivity parallel to magnetic field lines.

Another beneficial effect related to the nitrogen seeding is a reduced size of the edge localized modes, ELMs, which lead to transiently increased power loads at the targets. The ELMs change from large type-I to high frequency, broadband type-III ELMs that are more benign. During complete detachment the ELM size can be even reduced to a level where no ELM signatures in the divertor and at the midplane can be observed (ELM suppression) and transient reattachment during ELMs is absent.

A transient increase of the line integrated plasma density with progressing detachment indicates an increase of the plasma fueling efficiency. The change in core plasma fueling is most likely due to a reduced shielding of neutrals from the inner divertor by a high plasma density region, which dissolves with nitrogen seeding.

This thesis uses an integrated approach to study detachment with dedicated experiments in ASDEX Upgrade and accompanying detailed modeling for the analysis and the interpretation of the data. The approach furthers the understanding of divertor detachment in H-mode conditions beyond what is possible with experiment or modeling alone. The experimental data is used to validate the modeled plasmas and in turn the simulations supplement the experimental information thereby overcoming the limited resolution and the challenge of the difficult interpretation of line integrated measurements. The complexity and the non-linear interaction of the plasma processes in the divertor are an obstacle for uncovering the involved physical processes. Therefore, the numerical modeling provides a tool to identify the elementary physical effects.

Qualitative understanding of the detachment process has been established for some time [48, 124, 131, 365, 392], but a quantitative match of numerical models has not been shown before. Major improvement in comparing and matching the numerical simulations to the experiment has been achieved for ASDEX Upgrade L-mode discharges [166, 167, 184, 228, 241, 350]. The modeling of the high recycling and the completely detached H-mode discharges with high heating power and large radiated power fractions in this thesis is a novelty. The modeling was able to recover the main observed phenomena, i.e. the X-point radiation that induces low temperatures at the X-point as well as large temperature variations on closed field lines, a pedestal pressure drop and the occurrence of complete detachment. A detailed comparison of the simulations with the experimental data using virtual diagnostics shows good agreement in the radiated power fraction, in line integrated spectroscopic measurements as well as for the plasma profiles at the midplane and at the divertor targets. The level of agreement is substantially improved compared to previous modeling of H-mode plasmas. A discrepancy remains in the divertor neutral pressure in both modeled plasma scenarios. Efforts to achieve experimentally observed neutral densities in the divertor at experimental separatrix densities were not successful and point to a deficiency of the code to describe the divertor neutral compression and the core plasma fueling correctly. At the same time it must be concluded that the pressure removal by charge exchange is not dominant in the

description of the detachment process in our simulations.

The modeling shows that an unconventional assumption of an increased perpendicular transport in the divertor of ASDEX Upgrade is required to reproduce experimental measurements at the midplane and at the target simultaneously in both modeled H-mode plasma scenarios. A larger transport increase in the inner than in the outer divertor is necessary to simultaneously match both targets. The transport increase needed is a factor 5–10 for the outer divertor and a factor 50–100 for the inner divertor in non-drift simulations. In completely detached plasma simulations the inclusion of drift effects is required to match and stabilize the experimentally observed X-point radiation. The appearance of the X-point radiation inside the confined plasma and the use of drifts in such completely detached plasma simulations reduce the necessary divertor transport increase to a factor 2 for the outer and 10 for the inner divertor.

The transport increase broadens the target profiles and increases the fluxes from the inner and outer SOL close to the separatrix into the private flux region. This leads to a reduction of the profile peaking of the electron density and of the particle flux close to the separatrix in the outer divertor. A further consequence is the reduction of the pressure in the inner divertor, especially in the divertor leg below the divertor baffle. The additional perpendicular losses of particles and energy into the private flux region and into the far SOL also facilitate detachment. In the completely detached plasma scenario the impact of charge exchange and recombination on divertor detachment was shown to be of minor importance for the simulated pressure loss. The particle flux and the pressure reduction at the target dominantly stems from the reduction of the power flux into the divertor and the increased perpendicular transport into the private flux region and the far SOL.

The inclusion of drifts is crucial for modeling of the ASDEX Upgrade SOL and divertor in detached H-mode conditions with strong nitrogen seeding. Drifts are responsible for some of the experimental observations such as the detached vertical inner target, improved stability of the radiation at the X-point and improved impurity retention of the divertor. As expected, the diamagnetic drift affects the midplane profiles the strongest and reduces the plasma pressure. In the detached divertor the drifts lead to a broadening of the profiles and to additional particle transport from the outer to the inner divertor via the private flux region. In the inner divertor the drifts increase the density in the divertor volume, especially at the X-point, and redistribute particles from close to the separatrix into the far SOL. The radiation losses increase and the radiation moves to the X-point. In drift simulations of completely detached plasmas the target sheath boundary conditions seems to be a limitation for the numerical stability of the code. An adaptation of the Bohm condition to conditions of low plasma flow towards the targets seems to be required.

This thesis demonstrated that a better characterization of the plasma parameters in the divertor volume is necessary in order to further discern a number of physical processes and to asses their relative importance for the occurrence of detachment. Additional spectroscopic measurements can be made available in the future, but new divertor diagnostics are required to validate the poloidal or parallel profile of the plasma parameters in the divertor volume between the target and the X-point. A divertor Thomson scatter-

ing system in combination with an evaluation of the ionization source distribution from spectral line emission analysis [269] would be a powerful tool that could provide parallel profiles of the plasma parameters and sources. Such information could be used to constrain the perpendicular transport in the divertor and validate the poloidal distribution of the plasma parameters in the divertor volume.

Future predictive modeling of the presented plasma scenarios is hampered by the fact that the perpendicular transport coefficient profiles are specified to match the experimental data. For reliable predictive modeling a validation of these transport coefficients is necessary and a first principle model for the derivation of such transport coefficients in future devices and scenarios is required. Both remain a task for future investigations.

In summary, this work has made substantial progress in demonstrating the ability of the SOLPS code to describe the experimental observations and match most of the absolute numbers of integrated and local plasma properties within the experimental errorbars for ASDEX Upgrade H-mode plasmas in high recycling and completely detached conditions with high heating powers. The physical model of SOLPS has been validated to a large extent for the presented plasma scenarios. Additional effort is required to understand and eliminate the deficiency of the code to model the neutral density in the divertor correctly.

High radiative fractions inside the confined plasma, small ELMs and detached divertor targets will be necessary in future fusion devices in order to handle the power exhaust in the SOL and in the divertor, while operating in an H-mode regime with good confinement. Experimentally, this thesis demonstrated the accessibility to such a plasma regime that might be an interesting candidate for a plasma scenario of future fusion devices.

APPENDIX A

Acknowledgements

Detlev Reiter and Marco Wischmeier.

I would like to thank the whole IPP staff and in particular the (PhD) students that made the time at IPP worthwhile not only on a professional but also on a personal basis. In particular, I am grateful to my office mates Gerd Meisl and Matthias Bernert. They were always ready to supply help, motivation and sweets when needed and I would not have been able to finish this thesis without their friendship. As my mentors for the last years Marco Wischmeier and Bruce Lipschultz have proven to be a steady help in challenging professional situations.

I want to thank my family, in particular my parents, who supported my early steps into the academic realm. They and my friends helped me to get through this thesis (relatively) unharmed, endured long working hours, weekend absences and in particular the last couple of weeks of weariness. I am very grateful in particular to Nadja who has supported me unwaveringly, helped me to focus on the important things and has been ready to compromise for this work to be completed as it is.

Bibliography

[1] S. Potzel, et al. *Plasma Phys. Control. Fusion*, 56(2):025010, February 2014.

[2] F. Reimold. *Numerical simulations of tungsten impurity transport in ASDEX Upgrade.* Thesis, Technical University Munich, Munich, December 2010.

[3] IEA. *Redrawing the energy-climate map.* IEA, Paris, France, 2013.

[4] IEA and Organisation for Economic Co-operation and Development. *World energy outlook, 2012.* OECD/IEA, Paris, 2012.

[5] IEA. *Key World Energy Statistics.* IEA, 2013.

[6] IEA and Organisation for Economic Co-operation and Development. *World Energy Outlook 2013.* IEA, Paris, France, 2013.

[7] L. Bernstein and Intergovernmental Panel on Climate Change (IPCC). *Climate change 2007: synthesis report.* IPCC, Geneva, 2008.

[8] N. Armaroli and V. Balzani. *Angewandte Chemie International Edition*, 46(1-2):52–66, January 2007.

[9] W. F. Pickard. *Energy Policy*, 49:346–354, October 2012.

[10] H. Lund. *Energy*, 32(6):912–919, June 2007.

[11] S. Jacobsson, et al. *Energy Policy*, 37(6):2143–2146, June 2009.

[12] A. Ipakchi and F. Albuyeh. *IEEE Power and Energy Magazine*, 7(2):52–62, March 2009.

[13] T. J. Hammons. *International Journal of Electrical Power & Energy Systems*, 30(8):462–475, October 2008.

[14] R. M. Margolis and D. M. Kammen. *Science*, 285(5428):690–692, July 1999.

[15] F. Marechal, et al. *Resources, Conservation and Recycling*, 44(3):245–262, June 2005.

[16] S. E. Jones. *Nature*, 321(6066):127–133, May 1986.

[17] H. Daniel. *Hyperfine Interact*, 82(1-4):409–421, March 1993.

[18] G. H. Miley, et al. *Final Report, 1986 - 1987 National Academy of Sciences -*

National Research Council, Washington, DC., -1, October 1987.

[19] N. Rostoker, et al. *Science*, 278(5342):1419–1422, November 1997.

[20] M. Lampe and W. Manheimer. Technical report, Defense Technical Information Center, October 1998.

[21] W. M. Nevins. *Science*, 281(5375):307–307, July 1998.

[22] T. Pütterich. Technical Report IPP 10/29, Max-Planck Institut for Plasma Physics, Garching. Germany, April 2006.

[23] H.-S. Bosch and G. M. Hale. *Nucl. Fusion*, 32(4):611, April 1992.

[24] A. A. F. Tavassoli, et al. *Journal of Nuclear Materials*, 329–333, Part A:257–262, August 2004.

[25] A. A. F. Tavassoli, et al. *Fusion Engineering and Design*, 61–62:617–628, November 2002.

[26] A. Möslang, et al. *Nucl. Fusion*, 45(7):649, July 2005.

[27] N. Baluc, et al. *Journal of Nuclear Materials*, 367–370, Part A:33–41, August 2007.

[28] Y. Horibe and M. Kobayakawa. *Geochimica et Cosmochimica Acta*, 20(3–4):273–283, November 1960.

[29] J. Wesson. *Tokamaks*, volume 1. Clarendon Press, Oxford, England, 3rd edition, 2004.

[30] B. M. Oliver, et al. *International Journal of Radiation Applications and Instrumentation. Part A. Applied Radiation and Isotopes*, 38(11):959–965, 1987.

[31] M. Sawan. Technical report, University of California, California, 1999.

[32] H. Kawamura, et al. *Fusion Engineering and Design*, 61–62:391–397, November 2002.

[33] S. E. Kesler, et al. *Ore Geology Reviews*, 48:55–69, October 2012.

[34] R. Dux. Technical Report IPP 10/27, Max-Planck Institut for Plasma Physics, Munich, December 2004.

[35] E. I. Moses. *Nucl. Fusion*, 49(10):104022, October 2009.

[36] B. Bigot. *Journal de Physique IV (Proceedings)*, 133:3–8, June 2006.

[37] J. Lindl. *Physics of Plasmas (1994-present)*, 2(11):3933–4024, November 1995.

[38] S. H. Glenzer, et al. *Science*, 327(5970):1228–1231, March 2010.

[39] J. Biener, et al. *Fusion science and technology*, 49(4):737, 2006.

[40] J. Nuckolls, et al. *Nature*, 239(5368):139–142, September 1972.

[41] S. Atzeni, et al. *Nucl. Fusion*, 49(5):055008, May 2009.

[42] J. P. Freidberg. *Plasma physics and fusion energy.* Cambridge University Press,

Cambridge, 2007.

[43] U. Stroth. *Plasmaphysik - Phänomene, Grundlagen, Anwendungen.* Vieweg + Teubner Verlag, Wiesbaden, Germany, 1st edition, 2011.

[44] R. Balescu. *Transport processes in plasmas - Classical Transport Theory*, volume 1. Elsevier Science & Technology, Amsterdam, 1st edition, 1988.

[45] J. F. Lyon. *Plasma Phys. Control. Fusion*, 32(11):1041, November 1990.

[46] A. Sagara, et al. *Fusion Engineering and Design*, 83(10):1690–1695, 2008.

[47] G. Grieger, et al. *Physics of Fluids B: Plasma Physics (1989-1993)*, 4(7):2081–2091, July 1992.

[48] P. C. Stangeby. *The Plasma Boundary of Magnetic Fusion Devices.* Institute of Physics Pub., Bristol; Philadelphia, 2000.

[49] G. Birkenmeier, et al. *Physical Review Letters*, 107(2), July 2011.

[50] C. Silva, et al. *Plasma Physics and Controlled Fusion*, 53(8):085021, August 2011.

[51] D. Carralero, et al. *Nucl. Fusion*, 54(12):123005, December 2014.

[52] H.-S. Bosch, et al. *Plasma Phys. Control. Fusion*, 39(11):1771, November 1997.

[53] H.-S. Bosch, et al. *Journal of Nuclear Materials*, 241–243:82–91, February 1997.

[54] A. Kallenbach, et al. *Nuclear Fusion*, 51(9):094012, September 2011.

[55] A. Loarte, et al. *Nuclear Fusion*, 47(6):S203–S263, June 2007.

[56] F. Wagner. *Plasma Physics and Controlled Fusion*, 49(12B):B1–B33, December 2007.

[57] F. Ryter, et al. *Nucl. Fusion*, 53(11):113003, November 2013.

[58] E. J. Doyle, et al. *Nuclear Fusion*, 47(6):S18–S127, June 2007.

[59] K. H. Burrell. *Physics of Plasmas (1994-present)*, 4(5):1499–1518, May 1997.

[60] P. Mantica, et al. *Phys. Rev. Lett.*, 102(17):175002, April 2009.

[61] O. Sauter, et al. *Physics of Plasmas (1994-present)*, 21(5):055906, May 2014.

[62] M. Shimada, et al. *Nuclear Fusion*, 47(6):S1–S17, June 2007.

[63] H. Zohm. *Plasma Physics and Controlled Fusion*, 38(2):105–128, February 1996.

[64] J. W. Connor. *Plasma physics and controlled fusion*, 40(2):191, 1998.

[65] M. G. Dunne. *Inter-ELM evolution of the edge current density profile on the ASDEX upgrade tokamak.* Thesis, University College Cork, Cork, Ireland, 2013.

[66] J. Rapp, et al. *Nuclear Fusion*, 49(9):095012, September 2009.

[67] T. Pütterich, et al. *Journal of Nuclear Materials*, 415(1, Supplement):S334–S339, August 2011.

[68] A. R. Raffray, et al. *Fusion Engineering and Design*, 85(1):93–108, January 2010.

[69] V. Barabash, et al. *Journal of Nuclear Materials*, 258–263, Part 1:149–159, October 1998.

[70] J. Roth. *Journal of Nuclear Materials*, 266–269:51–57, March 1999.

[71] R. Behrisch and W. Eckstein. *Sputtering by Particle Bombardment.* Topics in Applied Physics. Springer, Berlin, Heidelberg, 1st edition, 2007.

[72] G. Federici, et al. *Journal of Nuclear Materials*, 266–269:14–29, March 1999.

[73] J. Roth, et al. *Plasma Phys. Control. Fusion*, 50(10):103001, October 2008.

[74] R. Neu. Technical Report IPP 10/25, Max-Planck Institut for Plasma Physics, Garching. Germany, December 2003.

[75] R. Dux, et al. *Nuclear Fusion*, 51(5):053002, May 2011.

[76] K. Krieger, et al. *Journal of Nuclear Materials*, 266–269:207–216, March 1999.

[77] J. Roth and K. Schmid. *Phys. Scr.*, 2011(T145):014031, December 2011.

[78] S. Brezinsek, et al. *Nuclear Fusion*, 53(8):083023, 2013.

[79] Y. Ueda. *Plasma and Fusion Research*, 5:S1009–S1009, 2010.

[80] B. Lipschultz, et al. *Nuclear Fusion*, 52(12):123002, 2012.

[81] M. Mayer, et al. *Journal of Nuclear Materials*, 390–391:538–543, June 2009.

[82] G. F. Matthews. *Journal of Nuclear Materials*, 438, Supplement:S2–S10, July 2013.

[83] R. L. Neu, et al. *Plasma Science, IEEE Transactions on*, 42(3):552–562, 2014.

[84] P. Batistoni. Technical Report CCE-FU 49/6., March 2010.

[85] V. Mukhovatov, et al. *Nuclear Fusion*, 47(6):S404–S413, June 2007.

[86] T. Eich, et al. *Journal of Nuclear Materials*, 438:S72–S77, July 2013.

[87] C. S. Pitcher, et al. *Journal of nuclear materials*, 241:696–700, 1997.

[88] A. Herrmann, et al. *Plasma Phys. Control. Fusion*, 37(1):17, January 1995.

[89] R. Schneider, et al. *Contributions to Plasma Physics*, 46(1-2):3–191, February 2006.

[90] H. P. Summers, et al. *Plasma Phys. Control. Fusion*, 48(2):263, February 2006.

[91] D. E. Post and R. V. Jensen. *Atomic Data and Nuclear Data Tables*, 20:397–439, 1977.

[92] A. Kallenbach, et al. *Plasma Physics and Controlled Fusion*, 55(12):124041, December 2013.

[93] C. S. Pitcher and P. C. Stangeby. *Plasma Phys. Control. Fusion*, 39(6):779, June 1997.

[94] R. Dux, et al. *Plasma Phys. Control. Fusion*, 38(7):989, July 1996.

[95] A. Kallenbach, et al. *Plasma Phys. Control. Fusion*, 38(12):2097, December 1996.

[96] A. Kallenbach. In *IAEA 2014*, pages EX/7–1, St. Petersburg, Russia, March 2014.

[97] A. Kallenbach, et al. In *Proc. 24rd IAEA Fusion Energy Conference (San Diego, CA,)*, 2012.

[98] H.-S. Bosch, et al. *Phys. Rev. Lett.*, 76(14):2499–2502, April 1996.

[99] D. E. Post. *Journal of Nuclear Materials*, 220–222:143–157, April 1995.

[100] A. Scarabosio, et al. *Journal of Nuclear Materials*, 2015.

[101] M. Wischmeier, et al. *Contributions to Plasma Physics*, 44(1-3):268–273, 2004.

[102] S. Potzel. *Experimental classification of divertor detachment.* Thesis, Ludwig-Maximillian University Munich, Munich, 2012.

[103] M. Bernert. *Analysis of the H-mode density limit in the ASDEX Upgrade tokamak using bolometry.* Thesis, Ludwig-Maximillian University Munich, 2013.

[104] F. Reimold, et al. *Nucl. Fusion*, 55(3):033004, March 2015.

[105] K. Borrass, et al. *Nucl. Fusion*, 44(7):752, July 2004.

[106] W. Suttrop, et al. *Journal of Nuclear Materials*, 266-269:118–123, March 1999.

[107] J. R. Harrison. *Characterisation of Detached Plasmas on the MAST Tokamak.* Thesis, University of York, York, September 2010.

[108] S. Potzel, et al. *Journal of Nuclear Materials*, 438, Supplement:S285–S290, July 2013.

[109] D. Bohm. *The characteristics of electrical discharges in magnetic fields.* McGraw-Hill, New York, USA, 1949.

[110] K.-U. Riemann. *Contrib. Plasma Phys.*, 32(3-4):231–236, January 1992.

[111] J. E. Allen. *Plasma Sources Science and Technology*, 18(1):014004, February 2009.

[112] A. Guthrie and R. K. Wakerling. *The Characteristics of Electrical Discharge in Magnetic Fields.* McGraw-Hill, 1949.

[113] A. V. Chankin. *Plasma Phys. Control. Fusion*, 39(7):1059, July 1997.

[114] R. H. Cohen and D. D. Ryutov. *Contrib. Plasma Phys.*, 44(1-3):111–125, April 2004.

[115] P. C. Stangeby. *Physics of Fluids*, 27(3):682, 1984.

[116] S. Marsen, et al. *Journal of Nuclear Materials*, 438:S393–S396, July 2013.

[117] R. A. Jong, et al. *Journal of Nuclear Materials*, 196–198:800–803, December 1992.

[118] P. C. Stangeby, et al. *Journal of Nuclear Materials*, 241-243:358–362, February 1997.

[119] I. H. Hutchinson. *Nucl. Fusion*, 34(10):1337, October 1994.

[120] B. Lipschultz, et al. *Journal of Nuclear Materials*, 266–269:370–375, March 1999.

[121] T. W. Petrie, et al. *Journal of Nuclear Materials*, 241–243:639–644, February 1997.

[122] A. Kallenbach, et al. *Journal of Nuclear Materials*, 290–293:639–643, March 2001.

[123] J. Neuhauser, et al. *Plasma Phys. Control. Fusion*, 37(11A):A37, November 1995.

[124] A. Loarte, et al. *Nucl. Fusion*, 38(3):331, March 1998.

[125] B. LaBombard, et al. *Physics of Plasmas (1994-present)*, 2(6):2242–2248, June 1995.

[126] B. Lipschultz, et al. *Fusion science and technology*, 51(3):369–389, April 2007.

[127] S. Potzel, et al. *Nucl. Fusion*, 54(1):013001, January 2014.

[128] M. Greenwald, et al. Technical Report PFC/JA-86-22, PSFC Massachusetts Institute of Technology, Boston, USA, January 1988. 00626.

[129] A. Huber, et al. *Journal of Nuclear Materials*, 438, Supplement:S139–S147, July 2013.

[130] F. Reimold, et al. *Journal of Nuclear Materials*, 2015. accepted.

[131] C. S. Pitcher, et al. *Journal of Nuclear Materials*, 220–222(0):213–217, April 1995.

[132] D. D. Ryutov, et al. *Contributions to Plasma Physics*, 52(5-6):539–543, 2012.

[133] K. Borrass. *Nucl. Fusion*, 31(6):1035, June 1991.

[134] A. W. Leonard, et al. *Phys. Rev. Lett.*, 78(25):4769–4772, June 1997.

[135] A. W. Leonard, et al. *Physics of Plasmas*, 5(5):1736, 1998.

[136] S. A. Self and H. N. Ewald. *Physics of Fluids (1958-1988)*, 9(12):2486–2492, December 1966.

[137] H. P. Summers. *ttp://www.adas.ac.uk./manual.php*, 2004.

[138] A. Kukushkin. In *IAEA 2014*, St. Petersburg, Russia, October 2014.

[139] S. I. Krasheninnikov, et al. *Physics of Plasmas (1994-present)*, 4(5):1638–1646, May 1997.

[140] S. I. Krasheninnikov, et al. *Journal of Nuclear Materials*, 241–243:283–287, February 1997.

[141] G. M. McCracken, et al. *Nucl. Fusion*, 38(4):619, April 1998.

[142] A. Loarte, et al. *Contributions to Plasma Physics*, 40(3-4):508–513, 2000.

[143] S. I. Krasheninnikov, et al. *Journal of Nuclear Materials*, 266–269:251–257, March 1999.

[144] R. D. Monk, et al. *Journal of Nuclear Materials*, 266–269:37–43, March 1999.

[145] A. E. Järvinen, et al. *Journal of Nuclear Materials*, 2015.

[146] D. Lumma, et al. *Physics of Plasmas (1994-present)*, 4(7):2555–2566, July 1997.

[147] R. Schneider, et al. *Journal of Nuclear Materials*, 266–269(0):175–181, March 1999.

[148] R. Schneider, et al. *Journal of Nuclear Materials*, 241–243:701–706, February 1997.

[149] J. Schweinzer, et al. *Journal of Nuclear Materials*, 266–269:934–939, March 1999.

[150] H.-S. Bosch, et al. *Journal of Nuclear Materials*, 266–269:462–466, March 1999.

[151] L. D. Horton, et al. *Journal of Nuclear Materials*, 266–269:160–167, March 1999.

[152] N. Asakura, et al. *Nucl. Fusion*, 39(11Y):1983, November 1999.

[153] N. S. Wolf, et al. *Journal of nuclear materials*, 266:739–741, 1999.

[154] M. Groth. In *PSI 2014*, Kanazawa, Japan, May 2014.

[155] A. Kallenbach, et al. *Nucl. Fusion*, 39(7):901, July 1999.

[156] A. Kukushkin, et al. *Nuclear Fusion*, 49(7):075008, July 2009. 00088.

[157] R. A. Pitts, et al. *Journal of Nuclear Materials*, 290–293:940–946, March 2001.

[158] D. D. Ryutov, et al. *Physics of Plasmas (1994-present)*, 15(9):092501, September 2008.

[159] M. V. Umansky, et al. *Nucl. Fusion*, 49(7):075005, July 2009.

[160] G. Fishpool, et al. *Journal of Nuclear Materials*, 438, Supplement:S356–S359, July 2013.

[161] P. M. Valanju, et al. *Physics of Plasmas (1994-present)*, 16(5):056110, April 2009.

[162] E. Havlíčková, et al. *Plasma Phys. Control. Fusion*, 55(6):065004, June 2013.

[163] S. I. Krasheninnikov. *Physics of Plasmas (1994-present)*, 4(11):3741–3743, November 1997.

[164] S. I. Krasheninnikov, et al. *Physics of Plasmas (1994-present)*, 2(7):2717–2728, July 1995.

[165] T. Eich, et al. *Journal of Nuclear Materials*, 390-391:760–763, June 2009.

[166] L. Aho-Mantila, June 2014.

[167] L. Aho-Mantila, September 2014.

[168] N. Asakura, et al. *Nucl. Fusion*, 36(6):795, June 1996.

[169] S. Potzel, et al. *Journal of Nuclear Materials*, 2015.

[170] M. Nakamura, et al. *Journal of Nuclear Materials*, 415(1, Supplement):S553–S556, August 2011.

[171] S. Lisgo, et al. *Journal of Nuclear Materials*, 337–339:139–145, March 2005.

[172] A. Taroni, et al. *Contrib. Plasma Phys.*, 32(3-4):438–443, January 1992.

[173] S. Wiesen. JET-ITC project report, JET, Jülich, Germany, June 2006.

[174] J. P. Verboncoeur, et al. *J. Comput. Phys.*, 104(2):321–328, February 1993.

[175] A. Chankin, et al. *Contrib. Plasma Phys.*, 52(5-6):500–504, June 2012.

[176] P. C. Stangeby and J. D. Elder. *Journal of Nuclear Materials*, 196–198:258–263, December 1992.

[177] I. Hyodo, et al. *Journal of Nuclear Materials*, 313–316:1183–1187, March 2003.

[178] T. Lunt, et al. *Plasma Physics and Controlled Fusion*, 53(12):125010, December 2011.

[179] Y. Feng, et al. In *Proc. 38th EPS Conf. on Plasma Physics (Strasbourg, France, 27 June–1 July)*, 2011.

[180] F. Schwander, et al. In *PET 2014*, 2014.

[181] A. Kallenbach, et al. *Plasma Phys. Control. Fusion*, 52(5):055002, May 2010.

[182] J. A. Goetz, et al. *Physics of Plasmas (1994-present)*, 3(5):1908–1915, May 1996.

[183] J. Rapp, et al. *Nuclear Fusion*, 52(12):122002, December 2012.

[184] L. Aho-Mantila, et al. *Nucl. Fusion*, 52(10):103007, October 2012.

[185] N. Asakura, et al. *Journal of Nuclear Materials*, 241–243:559–563, February 1997.

[186] S. Brezinsek, et al. *Journal of Nuclear Materials*, 390-391:267–273, June 2009.

[187] R. D. Monk, et al. *Journal of Nuclear Materials*, 241–243:396–401, February 1997.

[188] G. Matthews, et al. *Journal of Nuclear Materials*, 241–243:450–455, February 1997.

[189] A. Huber, et al. Berlin, Germany, June 2014.

[190] T. W. Petrie, et al. *Journal of nuclear materials*, 363:416–420, 2007.

[191] M. E. Fenstermacher, et al. *Journal of Nuclear Materials*, 241–243:666–671, February 1997.

[192] O. Gruber, et al. *Physical review letters*, 74(21):4217, 1995.

[193] C. Giroud, et al. *Nucl. Fusion*, 52(6):063022, June 2012.

[194] R. Neu, et al. *Physics of Plasmas*, 20(5):056111, 2013.

[195] M. Groth, et al. *Nucl. Fusion*, 53(9):093016, September 2013.

[196] B. Lipschultz, et al. *Plasma physics and controlled fusion*, 44(6):733, 2002.

[197] C. S. Pitcher, et al. *Physics of Plasmas (1994-present)*, 7(5):1894–1903, 2000.

[198] B. Lipschultz. In *IAEA 1998*, Yokohama, Japan, 1998.

[199] B. Lipschultz, et al. *Nuclear Fusion*, 24(8):977–988, August 1984.

[200] W. M. Stacey. *Physics of Plasmas (1994-present)*, 8(2):525–532, February 2001.

[201] T. W. Petrie, et al. *Nucl. Fusion*, 48(4):045010, April 2008.

[202] S. L. Allen, et al. *Journal of Nuclear Materials*, 241–243:595–601, February 1997.

[203] A. G. McLean. In *PSI 2014*, Kanazawa, Japan, May 2014.

[204] J. M. Canik, et al. *Bulletin of the American Physical Society*, 59, 2014.

[205] N. Asakura, et al. *Nuclear Fusion*, 49(11):115010, November 2009.

[206] A. Hatayama, et al. *Journal of Nuclear Materials*, 290–293:407–412, March 2001.

[207] T. Nakano, et al. *Journal of Nuclear Materials*, 390-391:255–258, June 2009.

[208] K. Fujimoto, et al. *Plasma and Fusion Research*, 4:025–025, 2009.

[209] F. Piras, et al. *Plasma Phys. Control. Fusion*, 51(5):055009, May 2009.

[210] D. D. Ryutov. *Physics of Plasmas (1994-present)*, 14(6):064502, June 2007.

[211] D. D. Ryutov, et al. *Plasma Phys. Control. Fusion*, 52(10):105001, October 2010.

[212] D. D. Ryutov, et al. *Plasma Phys. Control. Fusion*, 54(12):124050, December 2012.

[213] V. A. Soukhanovskii, et al. *Journal of Nuclear Materials*, 438, Supplement:S96–S101, July 2013.

[214] V. A. Soukhanovskii, et al. *Physics of Plasmas (1994-present)*, 19(8):082504, August 2012.

[215] M. Kotschenreuther, et al. *Physics of Plasmas (1994-present)*, 14(7):072502, July 2007.

[216] P. M. Valanju, et al. *Fusion Engineering and Design*, 85(1):46–52, January 2010.

[217] M. Nakamura, et al. *Plasma and Fusion Research*, 6:2403098–2403098, 2011.

[218] W. M. Stacey, et al. *Physics of Plasmas (1994-present)*, 9(3):888–897, March 2002.

[219] W. M. Stacey. *Physics of Plasmas (1994-present)*, 3(7):2673–2678, July 1996.

[220] M. Z. Tokar. *Physics of Plasmas (1994-present)*, 9(5):1646–1653, April 2002.

[221] V. Kotov, et al. *Journal of Nuclear Materials*, 438, Supplement:S449–S452, July 2013.

[222] F. A. Kelly, et al. *Physics of Plasmas*, 8(7):3382, July 2001.

[223] R. Schneider, et al. *Journal of Nuclear Materials*, 196–198:810–815, December 1992.

[224] D. Coster, et al. *Journal of Nuclear Materials*, 241-243:690–695, February 1997.

[225] M. Wischmeier, et al. *Contributions to Plasma Physics*, 48(1-3):249–254, 2008.

[226] M. Wischmeier, et al. *Journal of Nuclear Materials*, 313–316:980–985, March 2003.

[227] C. Guillemaut, et al. *Journal of Nuclear Materials*, 438, Supplement:S638–S642, July 2013.

[228] L. Aho-Mantila, et al. *Journal of Nuclear Materials*, 438, Supplement:S321–S325, July 2013.

[229] V. Kotov, et al. *Plasma Phys. Control. Fusion*, 50(10):105012, October 2008.

[230] S. Wiesen, et al. *Journal of Nuclear Materials*, 415(1, Supplement):S535–S539, August 2011.

[231] M. Groth, et al. *Plasma Physics and Controlled Fusion*, 53(12):124017, December 2011.

[232] V. Kotov, et al. *Contributions to Plasma Physics*, 46(7-9):635–642, 2006.

[233] T. Lunt, et al. *Plasma Physics and Controlled Fusion*, 56(3):035009, 2014.

[234] A. S. Kukushkin, et al. *Nucl. Fusion*, 45(7):608, July 2005.

[235] A. Kukushkin, et al. *Journal of Nuclear Materials*, 241–243:268–272, February 1997.

[236] M. Wischmeier, et al. *Journal of Nuclear Materials*, 390–391:250–254, June 2009.

[237] A. Kallenbach, et al. *Journal of Nuclear Materials*, 390–391:278–281, June 2009.

[238] K. McCormick, et al. *Journal of Nuclear Materials*, 390–391:465–469, June 2009.

[239] L. Aho-Mantila. In *IAEA 2014*, St. Petersburg, Russia, 2014.

[240] L. Aho-Mantila. In *TTF 2014*, 2014.

[241] L. Aho-Mantila. In *EPS 2014*, Berlin, June 2014.

[242] A. Herrmann, et al. *Journal of Nuclear Materials*, 313–316:759–767, March 2003.

[243] I. H. Hutchinson. *Principles of Plasma diagnosics*. Cambridge Univ. Press, New York, USA, 2. edition, 2005.

[244] D. V. Orlinskij and G. Magyar. *Nucl. Fusion*, 28(4):611, April 1988.

[245] B. Streibl, et al. *FST*, 44(3):578–592, November 2003.

[246] R. Dux, et al. *Journal of Nuclear Materials*, 363–365:112–116, June 2007.

[247] B. Streibl, et al. *Fusion Engineering and Design*, 56–57:867–872, October 2001.

[248] B. Streibl, et al. In C. VARANDAS and F. SERRA, editors, *Fusion Technology 1996*, pages 427–430. Elsevier, Oxford, 1997.

[249] P. J. Mc Carthy. *Physics of Plasmas (1994-present)*, 6(9):3554–3560, September 1999.

[250] P. J. Mc Carthy and A. U. Team. *Plasma Phys. Control. Fusion*, 54(1):015010, January 2012.

[251] J. Neuhauser, et al. *FST*, 44(3):659–681, November 2003.

[252] T. Eich, et al. *Nucl. Fusion*, 53(9):093031, September 2013.

[253] H. Murmann, et al. *Review of Scientific Instruments*, 63(10):4941–4943, October 1992.

[254] B. Kurzan, et al. *Review of Scientific Instruments*, 72(1):1111, 2001.

[255] B. Kurzan, et al. *Plasma Phys. Control. Fusion*, 46(1):299, January 2004.

[256] B. Kurzan, et al. *Plasma Phys. Control. Fusion*, 49(6):825, June 2007.

[257] R. Fischer, et al. *Plasma Phys. Control. Fusion*, 50(8):085009, August 2008.

[258] M. Willensdorfer, et al. *Review of Scientific Instruments*, 83(2):023501, 2012.

[259] M. Willensdorfer, et al. *Plasma Phys. Control. Fusion*, 56(2):025008, February 2014.

[260] S. K. Rathgeber, et al. In *EPS 2013*, Helsinki, Sweden, 2013.

[261] E. Viezzer, et al. *Review of Scientific Instruments*, 83(10):103501, October 2012.

[262] E. Viezzer. *Radial electric field studies in the plasma edge of ASDEX*. PhDThesis, Ludwig-Maximilians-Universität München, February 2013.

[263] B. Geiger, et al. *Plasma Phys. Control. Fusion*, 53(6):065010, June 2011.

[264] M. Bernert, et al. *Review of Scientific Instruments*, 85(3):033503, March 2014.

[265] H. Meister, et al. *Rev Sci Instrum*, 81(10):10E132, October 2010.

[266] L. Giannone, et al. *Review of Scientific Instruments*, 73(9):3205–3214, September 2002.

[267] L. Giannone, et al. *Plasma Phys. Control. Fusion*, 47(12):2123, December 2005.

[268] L. C. Ingesson, et al. *FST*, 53(2):528–576, February 2008.

[269] J. Harhausen, et al. *Plasma Physics and Controlled Fusion*, 53(2):025002, February 2011.

[270] S. Potzel. *Bestimmung der Elektronendichte im Divertorplasma mittels Starkverbreiterung der Balmerlinien*. Thesis, University Bayreuth, Bayreuth, Germany, January 2009.

[271] R. J. Goldston and P. H. Rutherford. *Introduction to Plasma Physics*. CRC Press, New York, USA, 1995.

[272] S. Lisgo, et al. *Journal of Nuclear Materials*, 390-391:1078–1080, June 2009.

[273] T. Fujimoto, et al. *Nucl. Fusion*, 28(7):1255, July 1988.

[274] B. Sieglin. *Te measurment in SOL at AUG by He-Line ratios*. Thesis, Technical University Munich, Munich, Germany, 2010.

[275] U. Fantz, et al. *Nucl. Fusion*, 46(6):S297, June 2006.

[276] H. R. Griem. *Principles of Plasma Spectroscopy*. Cambridge University Press,

Cambridge, 1997.

[277] K. Schmidtmann. Technical Report IPP 10/15, Max-Planck Institut for Plasma Physics, Garching. Germany, September 2000.

[278] A. Huber, et al. *Journal of nuclear materials*, 313:925–930, 2003.

[279] S. Brezinsek, et al. *Fusion Science and Technology*, 47(2):209–219, 2005.

[280] A. Thoma, et al. *Plasma Phys. Control. Fusion*, 39(9):1487, September 1997.

[281] K. Behringer, et al. *Plasma Phys. Control. Fusion*, 31(14):2059, December 1989.

[282] T. Kato, et al. *Journal of Nuclear Materials*, 220–222:493–496, April 1995.

[283] R. Prakash, et al. Technical Report IPP 10/31, Max-Planck Institut for Plasma Physics, Garching. Germany, September 2006.

[284] G. J. van Rooij, et al. *Journal of Nuclear Materials*, 438, Supplement:S42–S47, July 2013.

[285] A. Scarabosio, et al. *Journal of Nuclear Materials*, 390–391:494–497, June 2009.

[286] A. Scarabosio, et al. *Nuclear Instruments and Methods in Physics Research Section A: Accelerators, Spectrometers, Detectors and Associated Equipment*, 623(2):667–671, November 2010.

[287] H.-S. Bosch, et al. *Journal of Nuclear Materials*, 196–198(0):1074–1077, December 1992.

[288] G. Haas and H.-S. Bosch. *Vacuum*, 51(1):39–46, September 1998.

[289] R. L. Summers. *NASA TN D-5285*, volume 5285. National Aeronautics and Space Administration, 1969.

[290] M. Weinlich. Technical Report IPP 5/64, Max-Planck Institut for Plasma Physics, Munich, 1995.

[291] M. Weinlich and A. Carlson. *Physics of Plasmas (1994-present)*, 4(6):2151–2160, June 1997.

[292] P. C. Stangeby. *J. Phys. D: Appl. Phys.*, 20(11):1472, November 1987.

[293] B. Sieglin. *Experimental Investigation of Heat Transport and Divertor Loads of Fusion Plasma in All Metal ASDEX Upgrade and JET*. Thesis, Technical University Munich, Munich, May 2014.

[294] L. Aho-Mantila. *Divertor plasma conditions and their effect on carbon migration in the ASDEX upgrade tokamak*. PhD thesis, VTT, Espoo, 2011.

[295] M. Lehnen. In *IAEA 2010*, 2010.

[296] G. Pautasso, et al. *Plasma Phys. Control. Fusion*, 51(12):124056, December 2009.

[297] A. Kallenbach, November 2014.

[298] S. Nakazawa, et al. *Contributions to Plasma Physics*, 40(3-4):491–497, 2000.

[299] S. Potzel, et al. In *EPS 2013*, Helsinki, 2013.

[300] M. E. Fenstermacher, et al. *Plasma Phys. Control. Fusion*, 41(3A):A345, March 1999.

[301] T. Ishijima, et al. *Plasma Phys. Control. Fusion*, 41(9):1155, September 1999.

[302] L. Casali, et al. In *EPS 2014*, Berlin, Germany, 2014.

[303] D. Carralero. In *APS Division of Plasma Physics Meeting Abstracts*, New Orleans, USA, November 2014.

[304] G. Birkenmeier, et al. *Plasma Phys. Control. Fusion*, 56(7):075019, July 2014.

[305] J. Schweinzer, et al. *Nuclear Fusion*, 51(11):113003, November 2011.

[306] G. Tardini, et al. *Plasma Physics and Controlled Fusion*, 55(1):015010, January 2013.

[307] D. Post, et al. *Physics of Plasmas*, 2(6):2328, 1995.

[308] D. Post, et al. *Journal of Nuclear Materials*, 220–222:1014–1018, April 1995.

[309] N. Asakura, et al. *Journal of Nuclear Materials*, 415(1):S318–S321, August 2011.

[310] V. Mertens, et al. *Nucl. Fusion*, 40(11):1839, November 2000.

[311] X. Bonnin and D. P. Coster. Technical report, Max-Planck Institut for Plasma Physics, Garching. Germany, 2014.

[312] D. Reiter, et al. *Fusion Science and Technology*, 47(2):172–186, 2005.

[313] V. Kotov, et al. Technical Report Juel-4257, Forschungszentrum Jülich GmbH, Jülich, Germany, November 2007.

[314] D. Reiser. *Zur Anwendung der driftkinetischen Theorie in Monte-Carlo-Studien zum Verunreinigungstransport in Tokamak-Plasmen.* Thesis, Heinrich-Heine University, Düsseldorf, Germany, 1997.

[315] S. I. Braginskii. *Reviews of Plasma Physics*, 1:205, 1965.

[316] R. Balescu. *Transport processes in plasmas - Neoclassical Transport Theory*, volume 2. Elsevier Science & Technology, Amsterdam, 1st edition, 1988.

[317] E. Zawaideh, et al. *Physics of Fluids (1958-1988)*, 29(2):463–474, February 1986.

[318] L. Spitzer and R. Härm. *Phys. Rev.*, 89(5):977–981, March 1953.

[319] W. Fundamenski. *Plasma Physics and Controlled Fusion*, 47(11):R163–R208, November 2005.

[320] A. V. Chankin. In *PSI2014*, Kanazawa, Japan, May 2014.

[321] A. V. Chankin, et al. In *IAEA 2006*, 2006.

[322] O. V. Batishchev, et al. *Journal of Nuclear Materials*, 241–243:374–378, February 1997.

[323] A. V. Chankin, et al. *Plasma Physics and Controlled Fusion*, 56(2):25003–25013, February 2014.

[324] P. Helander and D. J. Sigmar. *Collisional Transport in Magnetized Plasmas*. Cambridge University Press, October 2005.

[325] A. G. Peeters. *Physics of Plasmas (1994-present)*, 7(1):268–275, January 2000.

[326] R. Dux and A. G. Peeters. *Nucl. Fusion*, 40(10):1721, October 2000.

[327] B. LaBombard, et al. *Nuclear Fusion*, 40(12):2041, 2000.

[328] H. W. Müller. Kanazawa, Japan, 2014.

[329] D. L. Rudakov, et al. *Plasma Physics and Controlled Fusion*, 44(6):717–731, June 2002.

[330] D. L. Rudakov, et al. *Nucl. Fusion*, 45(12):1589, December 2005.

[331] D. A. D'Ippolito, et al. *Physics of Plasmas (1994-present)*, 9(1):222–233, January 2002.

[332] O. Garcia, et al. *Nuclear Fusion*, 47(7):667–676, July 2007.

[333] V. Naulin. *Journal of Nuclear Materials*, 363-365:24–31, June 2007.

[334] S. I. Krasheninnikov. *Physics Letters A*, 283(5):368–370, 2001.

[335] D. A. D'Ippolito, et al. *Contrib. Plasma Phys.*, 44(1-3):205–216, April 2004.

[336] G. S. Xu, et al. *Nucl. Fusion*, 49(9):092002, September 2009.

[337] J. A. Boedo, et al. *Physics of Plasmas (1994-present)*, 10(5):1670–1677, April 2003.

[338] D. Carralero. In *PSI 2014*, Kanazawa, Japan, May 2014.

[339] B. LaBombard, et al. *Physics of Plasmas (1994-present)*, 8(5):2107–2117, May 2001.

[340] M. Kočan, et al. *Plasma Physics and Controlled Fusion*, 54(8):085009, August 2012.

[341] M. Kočan, et al. In *IAEA 2012*, 2012.

[342] M. Kočan, et al. *Contributions to Plasma Physics*, 53(1):22–26, 2013.

[343] M. Kočan, et al. *Nucl. Fusion*, 53(7):073047, July 2013.

[344] S. I. Krasheninnikov, et al. *Physics of Plasmas (1994-present)*, 16(1):014501, January 2009.

[345] J. R. Harrison. In *PSI 2014*, Kanazawa, Japan, May 2014.

[346] F. Militello. In *PSI 2014*, Kanazawa, Japan, May 2014.

[347] D. P. Coster. In *PSI 2014*, Kanazawa, Japan, May 2014.

[348] B. I. Cohen, et al. *Physics of Plasmas*, 20(5):055906, 2013.

[349] S. Niedner, et al. *Plasma Phys. Control. Fusion*, 44(4):397, April 2002.

[350] L. Aho-Mantila. In *PSI 2014*, Kanazawa, Japan, May 2014.

[351] V. Rozhansky, et al. *Journal of Nuclear Materials*, 438, Supplement:S297–S302, July 2013.

[352] V. Rozhansky, et al. *Journal of Nuclear Materials*, 313–316:1141–1149, March 2003.

[353] P. C. Stangeby and A. V. Chankin. *Nucl. Fusion*, 36(7):839, July 1996. 00051.

[354] A. V. Chankin, et al. *Journal of Nuclear Materials*, 290–293:518–524, March 2001. 00037.

[355] J. L. Terry, et al. *Fusion science and technology*, 51(3):342–356, 2007.

[356] A. V. Chankin, et al. *Nucl. Fusion*, 47(5):479, May 2007. 00028.

[357] A. Hatayama, et al. *Nucl. Fusion*, 40(12):2009, December 2000.

[358] S. I. Krasheninnikov, et al. *Physics of Plasmas (1994-present)*, 2(6):1972–1975, June 1995.

[359] A. V. Chankin and P. C. Stangeby. *Plasma Phys. Control. Fusion*, 36(9):1485, September 1994.

[360] P. Helander and D. J. Sigmar. *Collisional Transport in Magnetized Plasmas, by Per Helander , Dieter J. Sigmar, Cambridge, UK: Cambridge University Press, 2005*, -1, October 2005. 00408.

[361] D. Reiter. Technical Report The EIRENE Code User Manual, Forschungszentrum Jülich, Jülich, Germany, November 2009.

[362] D. R. Bates, et al. *Proc. R. Soc. Lond. A*, 270(1341):155–167, November 1962.

[363] D. Reiter. *Electronic file, FZ Jülich*, 2000.

[364] A. Y. Pigarov and S. I. Krasheninnikov. *Physics Letters A*, 222(4):251–257, November 1996.

[365] S. I. Krasheninnikov, et al. *Physics Letters A*, 214(5–6):285–291, May 1996.

[366] S. Brezinsek, et al. Technical Report EFDA–JET–PR(03)38, European Fusion Development Agreement, 2003.

[367] U. Fantz, et al. *Journal of Nuclear Materials*, 290–293:367–373, March 2001.

[368] P. Mertens, et al. *Plasma Phys. Control. Fusion*, 43(12A):A349, December 2001.

[369] M. Wischmeier. *Simulating divertor detachment in the TCV and JET tokamaks.* Thesis, Ecole Polytechnique Federale de Lausanne, Lausanne, 2004.

[370] U. Wenzel, et al. *Nucl. Fusion*, 39(7):873, July 1999.

[371] A. Hakola, et al. *Plasma Phys. Control. Fusion*, 55(12):124029, December 2013.

[372] J. Rosato, et al. *Contributions to Plasma Physics*, 50(3-5):398–403, 2010.

[373] V. Kotov and D. Reiter. *Plasma Phys. Control. Fusion*, 54(8):082003, August 2012.

[374] R. K. Janev, et al. Technical Report Juel-4105, Forschungszentrum Jülich GmbH, 2004.

[375] R. K. Janev, et al. In *Research supported by DOE,. Berlin and New York, Springer-Verlag (Springer Series on Atoms and Plasmas. Volume 4), 1987, 335 p.*, volume 4, 1987.

[376] R. K. Janev, et al. *Journal of Nuclear Materials*, 121:10–16, May 1984.

[377] H. P. Summers, et al. *Plasma physics and controlled fusion*, 44(12B):B323, 2002.

[378] J. Miettunen, et al. *Plasma Phys. Control. Fusion*, 56(9):095029, September 2014.

[379] D. Naujoks. *Plasma-material interaction in controlled fusion.* Springer, Berlin, 2006.

[380] D. Reiter. Technical Report Jül-2605, Forschungszentrum Jülich GmbH, Jülich, Germany, April 1992.

[381] G. Meisl. *Nitrogen implantation in tungsten and migration in the fusion experiment ASDEX Upgrade.* Thesis, Technical University Munich, Munich, Germany, December 2014.

[382] W. Eckstein. *Journal of Nuclear Materials*, 248:1–8, September 1997.

[383] D. Reiter. Technical report, January 2010.

[384] W. Eckstein. *Computer Simulation of Ion-Solid Interactions.* Springer Series in Materials Science. Springer Berlin Heidelberg, Berlin, Heidelberg, 1991.

[385] M. Mayer, et al. *Journal of Nuclear Materials*, 337–339:119–123, March 2005.

[386] M. F. Stamp, et al. *Journal of Nuclear Materials*, 266–269:685–690, March 1999.

[387] G. Meisl, et al. *New J. Phys.*, 16(9):093018, September 2014.

[388] V. Kotov and D. Reiter. *Plasma Physics and Controlled Fusion*, 51(11):115002, November 2009.

[389] A. Järvinen. In *PSI 2014*, Kanazawa, Japan, May 2014.

[390] D. Moulton, et al. *Journal of Nuclear Materials*, 415(1, Supplement):S509–S512, August 2011.

[391] C. Guillemaut, et al. *Nucl. Fusion*, 54(9):093012, September 2014.

[392] S. I. Krasheninnikov. *Czech J Phys*, 48(2):97–112, February 1998.